# DEVELOPMENT OF A HIGH-EFFICIENCY POWER AMPLIFIER

# FOR ENVELOPE TRACKING APPLICATIONS

A thesis submitted to Cardiff University

In candidature for the degree of

Doctor of Philosophy

By

**Zulhazmi A. Mokhti, M.Sc.**

Centre for High Frequency Engineering

School of Engineering

Cardiff University

United Kingdom

September 2016

# ABSTRACT

Complex and spectrally efficient modulation schemes present a power-efficiency challenge to base station power amplifiers due to the time-varying envelope and high peak-to-average power ratios involved. The envelope tracking architecture is one way to address this issue, where an envelope amplifier provides a dynamic, modulated supply to the power amplifier to reduce power consumption.

While most research into envelope tracking focuses on the envelope amplifier, this work focuses on optimising the power amplifier design for envelope tracking using the waveform engineering approach. It studies the behaviour of a highly-efficient power amplifier mode of operation (class-F) using a relatively low-cost high voltage laterally diffused metal oxide semiconductor (HVLDMOS) technology in an envelope tracking environment. A systematic design process is formulated based on identifying the optimum amplifier load and the envelope shaping function, and then applied in the development of an actual class-F power amplifier.

The fabricated power amplifier is integrated into an envelope tracking system and is able to produce one of the highest recorded efficiencies compared to current state-of-the-art envelope tracking amplifiers, which are mostly based on Gallium Nitride technology. The limitation of this design is its linearity performance, and the efficiency-linearity trade-off is analysed in detail in this work.

The use of continuous mode power amplifiers in envelope tracking is also explored for high-bandwidth operation. The limitation of such a technique is posed by the device nonlinear output capacitance, and this is analysed through the use of a novel characterisation approach called *voltage-pull*, which is derived from an active load-pull system but uses voltage waveforms as the target instead of loads.

This method is also used to investigate the possibility of exploiting the device nonlinear output capacitance as a $2^{nd}$ harmonic injection source to improve power amplifier efficiency, as predicted in a novel mathematical analysis presented in this work.

# KEY CONTRIBUTIONS

**Contribution 1:** Waveform-based characterisation of class-F and continuous class-F power amplifier modes in an envelope tracking environment.

**Contribution 2:** A waveform-based trade-off analysis between efficiency and linearity for different power amplifier modes in an envelope tracking architecture.

**Contribution 3:** Formulation of a design flow using waveform engineering to optimise the design of an RF power amplifier for envelope tracking applications.

**Contribution 4:** Design and fabrication of a high voltage LDMOS class-F power amplifier using the formulated design flow, and its integration into a real envelope tracking system.

**Contribution 5:** A novel mathematical analysis of the effect of the nonlinear device output capacitance, or the varactor effect, on continuous mode power amplifiers.

**Contribution 6:** A novel characterisation method for continuous mode power amplifiers called the *voltage-pull* method, which exposes the varactor effect that is hidden with conventional load-pull methods.

**Contribution 7:** Mathematical, simulation, and experimental work to investigate the use of device nonlinear output capacitance or varactor as a $2^{nd}$ harmonic injection source to improve amplifier efficiency.

# ACKNOWLEDGEMENTS

# LIST OF PUBLICATIONS

**First author:**

1. Z. Mokhti, P. Tasker, and J. Lees, "Correlation analysis between a VNA-based passive load pull system and an oscilloscope-based active load pull system: A case study," in *Microwave Measurement Conference (ARFTG), 2014 83rd ARFTG*, 2014, pp. 1-4.

2. Z. A. Mokhti, J. Lees, P. J. Tasker, and C. Cassan, "Investigating the linearity versus efficiency trade-off of different power amplifier modes in an envelope tracking architecture," in *Microwave Conference (EuMC), 2015 European*, 2015, pp. 1208-1211.

3. Z. A. Mokhti, P. J. Tasker, and J. Lees, "Using waveform engineering to optimize class-F power amplifier performance in an envelope tracking architecture," in *Microwave Conference (EuMC), 2014 44th European*, 2014, pp. 1301-1304.

4. Z. A. Mokhti, P. J. Tasker, and J. Lees, "Analyzing the improvement in efficiency through the integration of class-F power amplifiers compared to class-AB in an envelope tracking architecture," in *Teletraffic Congress (ITC), 2014 26th International*, 2014, pp. 1-4.

5. Z. A. Mokhti, P. J. Tasker, and J. Lees, "Analyzing device behaviour at the current generator plane of an envelope tracking power amplifier in a high efficiency mode," in *Automated RF & Microwave Measurement Society (ARMMS) Conference 2014.*

**Co-authored:**

6. A. Imtiaz, Z. A. Mokhti, J. Cuenca, and J. Lees, "An integrated inverse-F power amplifier design approach for heating applications in a microwave resonant cavity," in *2014 Asia-Pacific Microwave Conference*, 2014, pp. 756-758.

7. M. Lasanen, M. Aubree, C. Cassan, A. Conte, J. David, S. E. Elayoubi*, et al.*, "Environmental friendly mobile radio networks: Approaches of the European OPERA-Net 2 project," in *Telecommunications (ICT), 2013 20th International Conference on*, 2013, pp. 1-5.

8. F. L. Ogboi, P. Tasker, Z. Mokhti, J. Lees, J. Benedikt, S. Bensmida*, et al.*, "Sensitivity of AM/AM linearizer to AM/PM distortion in devices," in *Microwave Measurement Conference (ARFTG), 2014 83rd ARFTG*, 2014, pp. 1-4.

# LIST OF ACRONYMS

| | |
|---|---|
| **2D-EM** | Two dimension electromagnetic simulation |
| **2G** | Second generation mobile communication system |
| **3G** | Third generation mobile communication systems |
| **4G** | Fourth generation mobile communication systems |
| **AC** | Alternating current |
| **ACPR** | Adjacent channel power ratio |
| **ADS** | Advanced Design System |
| **AM** | Amplitude modulation |
| **APT** | Average power tracking |
| **BB** | Baseband |
| **$C_{DS}$** | Drain-to-source capacitance |
| **$C_{GD}$** | Gate-to-drain capacitance |
| **$CO_2$** | Carbon dioxide |
| **CW** | Continuous wave |
| **DA** | Doherty amplifier |
| **DAC** | Digital-to-analogue converter |
| **DC** | Direct current |
| **DC-IV** | Direct-current current-to-voltage ratio |
| **DE** | Drain efficiency |
| **DPD** | Digital pre-distortion |
| **DUT** | Device under test |
| **EA** | Envelope amplifier |
| **EER** | Envelope Elimination and Restoration |
| **ET** | Envelope Tracking |
| **FET** | Field effect transistor |
| **FFT** | Fast Fourier Transform |
| **FPGA** | Field-programmable gate array |
| **GaN** | Gallium Nitride |
| **$G_{OPT}$** | Optimum gain |
| **HBT** | Heterojunction bipolar transistor |
| **HEMT** | High electron mobility transistor |
| **HFET** | Heterostructure field effect transistor |

| | |
|---|---|
| **I** | In-phase |
| **IF** | Intermediate frequency |
| **I$_{GEN}$** | Current generator |
| **IM3** | Third order intermodulation |
| **IM5** | Fifth order intermodulation |
| **I$_{MAX}$** | Maximum current |
| **LDMOS** | Laterally diffused metal oxide semiconductor |
| **LTE** | Long Term Evolution |
| **MLIN** | Microstrip element |
| **MMIC** | Monolithic microwave integrated circuit |
| **NVNA** | Nonlinear vector network analyser |
| **OBO** | Output back-off |
| **OPEX** | Operating expense |
| **PA** | Power amplifier |
| **PAE** | Power added efficiency |
| **PAPR** | Peak-to-average power ratio |
| **pHEMT** | Pseudomorphic high electron mobility transistor |
| **P$_{IN}$** | Input power |
| **PM** | Phase modulation |
| **PRBS** | Pseudo-random bit sequence |
| **Q** | Quadrature |
| **RF** | Radio frequency |
| **RFPA** | Radio frequency power amplifier |
| **R$_{ON}$** | On-resistance |
| **R$_{OPT}$** | Optimum resistance |
| **TLIN** | Transmission line element |
| **TRL** | Thru Reflect Line |
| **VDS** | Drain-to-source voltage |
| **VIN** | Input voltage |
| **V$_{MAX}$** | Maximum voltage |
| **VNA** | Vector network analyser |
| **W-CDMA** | Wideband Code Division Multiple Access |

TABLE OF CONTENT

# Chapter 1

# Introduction

## 1.1      Research Motivation

The mobile communication industry has seen a tremendous growth over the past decade, where mobile data traffic has grown 4000-fold [1]. In the first quarter of 2016, there were 7.4 billion mobile subscriptions worldwide with half of these broadband subscriptions. Video streaming was the biggest contributor of smartphone mobile traffic at 43% followed by social networking at 20% [2]. The usage trend of mobile phones has moved towards *heavy-data* cases while the number of users keeps increasing at the same time. It is expected that the number of mobile subscriptions will exceed 26 billion by 2020 [3].

The rapid growth and the demand for wider bandwidth to cater for the heavy-data traffic shown in Fig. 1.1 have driven the development of more complex modulation schemes to allow for more users within the limited available spectrum. However, these spectrally-efficient modulation schemes present a power-efficiency challenge to the base-station power amplifier (PA) due to its time-varying envelope and high peak-to-average power ratio (PAPR). With the introduction of 4$^{th}$ generation mobile communication systems (4G), rise in energy cost, and the increasing demand in coverage, network operators are faced with high operating cost (OPEX) where approximately 30% is spent on base-station energy utilization with the RF power amplifier being the biggest

contributor accounting for 50-80% of the total power consumed [4, 5]. Improving PA efficiency will therefore contribute significantly towards reducing the operating cost.
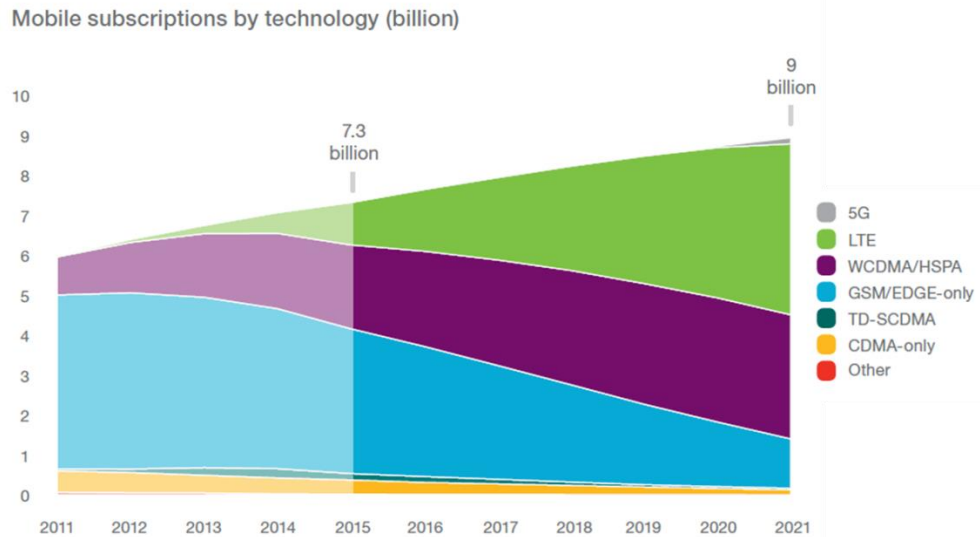


**Figure 1.1 – Worldwide mobile subscription trend [2].**

The motivation to improve base station power amplifier efficiency is not only financial but also environmental. A macro base station deployed in 2G/3G/4G infrastructure typically consumes between 2kW to 5kW of power [6]. In Europe alone it is estimated that a 20% efficiency improvement in 3G base station PA's would result in an annual 17 kiloton reduction in $CO_2$ emission [7].

This research focuses on the development of high-efficiency power amplifiers to address base station power efficiency utilising the envelope tracking architecture. The target application is for small cells to be used in a heterogeneous network with a peak transmit power of 50W. This work has been carried out as part of the *Opera-Net 2* project, which is an industry-driven European ICT research initiative funded through the Eureka's Celtic-Plus program. The *Opera-Net 2* consortium comprised 11 partners with different

specialization areas from within the industry and academia in Europe: Orange (France), Alcatel Lucent Bell Labs (France), Freescale (France, now NXP), Nokia (Finland), Thomson Broadcast (France, now Arelis), VTT (Finland), Efore (Belgium), Cardiff University (UK), Telecom Bretagne (France), University of Caen (France), and Alpha Technologies (Belgium).

The objective of the Opera Net 2 project is to reduce the environmental impact of mobile radio networks by analysing and providing an end-to-end solution from the standpoint of material lifecycle, hybrid energy sites, access network optimisation, architecture optimisation and hardware design, and standardization [8]. In terms of the current industry practice in base station architecture and hardware design, the Doherty PA with digital pre-distortion (DPD) is the preferred implementation due to its relatively high-efficiency performance over wide dynamic range whilst delivering high power, coupled with an absence of a high-power solution from the envelope tracking architecture [9]. However with the emergence of heterogeneous networks to address growth in data traffic, smaller cells with lower transmit-power are used to extend network capacity in dense areas [10, 11]. It is in this type of application that the envelope tracking PA architecture presents an attractive high-efficiency solution with its relatively high bandwidth capability, and is the focus of the Opera-Net 2 project for architecture and hardware design.

Cardiff University's role in Opera-Net 2 was in the development of a highly efficient RF PA using Freescale's next generation high voltage LDMOS transistors that would be used in an envelope tracking system developed by Arelis. As such, the Opera-Net 2 project acts as a platform for this PhD

research work and provides an industry validation for the designed PA prototype.

## 1.2    Research Objectives

There are several objectives outlined in this research towards developing a high-efficiency mode PA for ET applications using HV-LDMOS technology.   The first objective is to utilize Cardiff University's waveform engineering capabilities to understand the effect of variable drain bias on a high-efficiency mode PA.  The output capacitance ($C_{DS}$) varies nonlinearly with output voltage and an analysis at the device's current generator plane is needed to fully understand the load trajectory  in terms of boundary interaction relative to the IV plane, as a function of ET drain voltage.

The second objective is to use waveform engineering to formulate a systematic design methodology for a high-efficiency RF PA to be used in an ET application.   This design method will utilize the target load and the envelope shaping function as design parameters to optimise overall ET efficiency as well as linearity based on signal PAPR and other design specifications.

The third objective is to apply the method to design, build, and test a class-F PA in an industry standard ET system.   The ET-integration work is carried out in collaboration with Arelis, an Opera-Net 2 consortium member whom with their recent work in ET modulators, provide the capability to adopt a new, high-efficiency PA into their existing ET system.

The fourth objective is to investigate the use of envelope tracking as a baseband linearising method.   Baseband injection for linearisation is a

technique developed at Cardiff University utilising the waveform engineering system under multi-tone excitations [12]. This method has been proven to linearise a PA regardless of envelope shape and bandwidth but its effect on PA efficiency has not been tested.

Finally the fifth objective is to investigate the feasibility of applying continuous mode PA design in an envelope tracking application, which is an extension of the first objective. The continuous mode power amplifiers offer a high efficiency operation over a wider bandwidth but only at its peak power. The aim is to analyse the effect of nonlinear output capacitance on a continuous mode PA and how that affects the operation of a continuous mode amplifier in ET.

| Research Objectives | | | | |
|---|---|---|---|---|
| Investigate variable drain bias effect on high-efficiency mode PA | Formulate a systematic design method for high-efficiency RF PA in ET | Design & build LDMOS class-F PA and integrate into ET system | Investigate the use of ET as a baseband linearizing method | Investigate the feasibility of applying continuous mode PA in ET |
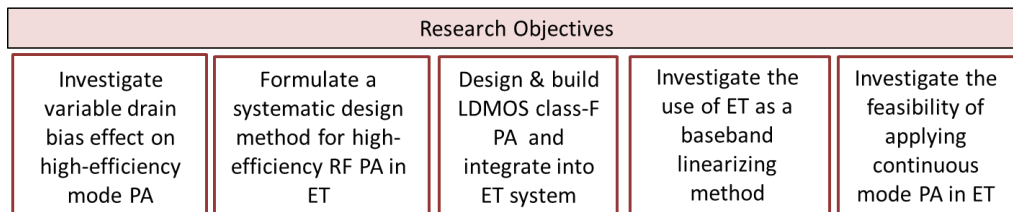
**Figure 1.2 - Research objectives.**

## 1.3      Thesis Organization

This thesis is organized into eight chapters, summarized as follows:

**Chapter 2** provides an overview of high-efficiency power amplifier modes and architectures. It discusses the challenges faced by the PA design community in dealing with signals with high PAPR. State-of-the-art power amplifiers of different architecture are also summarized.

**Chapter 3** presents the behaviour of a high-efficiency PA mode in a variable drain bias setting, which is an environment that can emulate the envelope

tracking condition. It investigates the impact of the nonlinear output capacitance on efficiency when class-F and class-AB Pas are optimised at different drain bias points. The efficiency and linearity trade-off when using different envelope shaping functions is also analysed. Through modulated signal simulations, this chapter also investigates the effectiveness of using ET as a baseband linearisation method for class-F compared to the previous work of class-AB.

**Chapter 4** describes the process of using waveform engineering to optimise a class-F PA design for envelope tracking applications based on the experimental results from Chapter 3. A systematic design method is proposed and applied in designing an actual class-F PA using an LDMOS device operating at 900MHz. The design goals, matching network design, and simulated results are described.

**Chapter 5** presents the initial standalone test results of the fabricated class-F PA followed by the integration of the PA into a full ET system used in the Opera-Net 2 project. System level test results are then presented, highlighting the benefits and limitations of using a class-F PA mode in an ET system.

**Chapter 6** investigates the integration of a continuous mode PA, which is an extension of the high-efficiency PA mode to achieve a higher bandwidth, in an envelope tracking architecture. Starting with a discussion on conventional continuous mode PA theory, simulated and measured results are then compared. A novel investigation of the device nonlinear output capacitance (varactor) effect on continuous mode PAs is presented through mathematical

analysis, where one of the theoretical findings points to the possibility of using the varactor effect for efficiency enhancement under certain load conditions.

**Chapter 7** presents an experimental validation to the theory of the varactor effect on continuous mode PA's, specifically on class-BJ power amplifiers. A novel measurement strategy to expose the varactor effect, termed the *voltage-pull*, is described. It also experiments with the possibility of exploiting the varactor as a $2^{nd}$ harmonic injection source to improve PA efficiency. In doing so this chapter presents a new design space for continuous mode PA, which is modified from the conventional design space as a result of the varactor effect.

**Chapter 8** summarizes and concludes the overall findings from this research work and derives future work that can be taken forward.

## 1.4      References

[1]    *Cisco Visual Networking Index: Global Mobile Data Traffic Forecast Update                              2015-2020*.                         Available: http://www.cisco.com/c/en/us/solutions/collateral/service-provider/visual-networking-index-vni/mobile-white-paper-c11-520862.pdf

[2]    *Ericsson        Mobility        Report        June        2016*.        Available: https://www.ericsson.com/res/docs/2016/ericsson-mobility-report-2016.pdf

[3]    *Ericsson        Mobility        Report        June        2015*.        Available: https://www.ericsson.com/res/docs/2015/ericsson-mobility-report-june-2015.pdf

[4]    L. M. Correia, D. Zeller, O. Blume, D. Ferling, Y. Jading, G. I*, et al.*, "Challenges and enabling technologies for energy aware mobile radio networks," *IEEE Communications Magazine,* vol. 48, pp. 66-72, 2010.

[5]    Z. Wang, *Envelope Tracking Power Amplifiers for Wireless Communications*: Artech House, 2014.

[6]　　M. Liu, L. Liu, X. Wu, L. Teng, J. Cao, and S. Qin, "A Research on the Telecommunication Base Station Power Consumption Investment Analysis and Optimized Configuration Method for Hybrid Energy Power," in *Telecommunications Energy Conference 'Smart Power and Efficiency' (INTELEC), Proceedings of 2013 35th International*, 2013, pp. 1-6.

[7]　　*OPERA-Net 2: Optimising Power Efficiency in Mobile Radio Networks 2*. Available: http://projects.celticplus.eu/opera-net2/index.html

[8]　　M. Aubree, D. Marquet, S. Le Masson, H. Louahlia, A. Chehade, J. David*, et al.*, "OPERA-Net 2 Project - An environmental global approach for radio access networks-achievements for off-grid systems," in *Telecommunications Energy Conference (INTELEC), 2014 IEEE 36th International*, 2014, pp. 1-7.

[9]　　R. Pengelly, C. Fager, and M. Ozen, "Doherty's Legacy: A History of the Doherty Power Amplifier from 1936 to the Present Day," *IEEE Microwave Magazine,* vol. 17, pp. 41-58, 2016.

[10]　A. Damnjanovic, J. Montojo, Y. Wei, T. Ji, T. Luo, M. Vajapeyam*, et al.*, "A survey on 3GPP heterogeneous networks," *IEEE Wireless Communications,* vol. 18, pp. 10-21, 2011.

[11]　S. Landstrom, A. Furuskar, K. Johansson, L. Falconetti, and F. Kronestedt, "Heterogeneous networks - increasing cellular capacity," *Ericsson Review,* vol. 1, 2011.

[12]　F. L. Ogboi, P. J. Tasker, M. Akmal, J. Lees, J. Benedikt, S. Bensmida*, et al.*, "A LSNA configured to perform baseband engineering for device linearity investigations under modulated excitations," in *Microwave Conference (EuMC), 2013 European*, 2013, pp. 684-687.

# Chapter 2

# Overview of Envelope Tracking and Other High-Efficiency Power Amplifiers

## 2.1    Introduction

Research into power amplifier (PA) efficiency improvement has been ongoing since the 1930s driven by increasing operating costs associated with high power (Megawatt) AM broadcast applications due to inefficient power transmitters and associated cooling requirements [1]. The advent of wireless mobile communication especially the introduction of the $3^{rd}$ generation mobile communication systems (3G) has further increased the need to improve power amplifier efficiency in order to have longer handsets battery life, lower electricity cost for network operators, and importantly lower $CO_2$ emission from mobile networks.

PA's in typical in typical mobile communications system base stations are responsible for 50-80% of the total power consumption [2]. From that total DC power consumed, typically only approximately 30% is converted into useful transmitted RF signals [3]. The main challenge in producing a high efficiency power amplifier in such applications is the high peak to average power ratio (PAPR) of the RF signal, which in some cases is in excess of 10dB [2]. This is because the PA needs to be efficient not only at peak power but also at

average power levels several dB's below where the PA would spend most of its time operating. As the demand for higher bandwidth increases, more complicated and dynamic modulation schemes are used, driving the signal PAPR increasingly higher. This puts a lot of pressure on the PA design community to provide solutions that continually improve PA efficiency and to react to the advancements in spectrally-efficient schemes, as well as accommodating the stringent linearity requirements implicit in new wireless standards.

This chapter provides a brief overview of the envelope tracking power amplifiers and the current research from literature. It begins by introducing different high efficiency PA *modes* that offer high efficiency close to saturation and at peak envelope power, as well as high-efficiency PA *architectures* that offer high efficiency over dynamic range or output back-off. A review of the state-of-the-art of one of these architectures; envelope tracking (ET) is presented, covering different aspects of the ET research such as the drain modulator, use of high-efficiency modes in ET, and linearisation techniques. Finally this chapter concludes with a discussion of the new research opportunities based on the latest literature and state-of-the-art review.

## 2.2 High Efficiency Power Amplifiers: *Modes* and *Architectures*

### 2.2.1 Addressing Efficiency at Peak Power: PA Modes

The efficiency of a PA, or *drain efficiency* (DE), is defined as the ratio of the fundamental output power to the DC supplied power. Another metric that is often used is *power added efficiency* (PAE) which takes into account the gain of the PA, and is defined as the ratio of the difference between output and

input fundamental power over the DC supplied power. For a PA with high gain, DE and PAE will be similar, but if the PA gain goes below for example 10dB, the DE and PAE difference would be more than 10% [4].

Several techniques have been developed in improving PA efficiency from the theoretical 50% limit of class-A, as summarized in Table 2.1, assuming an infinite harmonic content. The basis of these techniques is the reduction of the overlapping region between the current and the voltage at the device current generator plane by reducing the conduction angle, as well as increasing the drive level to an optimum point [5].

| | PA Mode | Conduction angle | Theoretical drain efficiency (%) |
|---|---|---|---|
| Linear amplifiers [6] | Class A | $2\pi$ | 50 |
| | Class AB | $\pi<\theta<2\pi$ | 50 – 78.5 |
| | Class B | $\pi$ | 78.5 |
| | Class C | $0<\theta<\pi$ | 78.5 – 100 |
| | Class J | $\pi$ | 78.5 |
| Switching amplifiers | Class D | $\pi$ | 100 |
| | Class E | $\pi$ | 100 |
| | Class F | $\pi$ | 100 |
| | Class F$^{-1}$ | $\pi$ | 100 |

**Table 2.1 - Summary of different PA modes.**

Classes A, AB, B, and C amplifiers in Table 2.1 have identical sinusoid voltage outputs and the difference in their efficiency is due to the current conduction angles. Different applications require different types of PA class and there is no one type that is best for all solutions [6]. For this research, class-F is chosen to be used in an envelope tracking architecture for a number of reasons. Firstly, it is able to provide higher baseline efficiency than that of

class-AB, which is typically used in ET power amplifiers. As will be seen in the next section, there is an opportunity to address this gap in literature for ET applications.

Secondly class-F is chosen instead of $F^{-1}$ because of the limitation presented by the large output capacitance $C_{DS}$ of the LDMOS device used for this work preventing a proper 2$^{nd}$ harmonic open circuit termination at the current generator plane with the available active load-pull system. Also as shown in a load-pull comparison between these 2 modes using LDMOS in [7], the class-F mode produced 4%-point higher peak drain efficiency compared to $F^{-1}$ for the same bias point. This was considered due to the increase in drain current during the off-state for the class- $F^{-1}$ mode at high input drive as the output voltage approaches breakdown. This peak drain efficiency is important for this work as it determines the highest achievable efficiency for a particular bias, and the strategy is then to use ET to maintain it over dynamic range through the use of an ET shaping function. This design strategy is discussed in more detail in Chapter 4.

Thirdly, even though class-F mode is narrowband in its operation, it can be built upon to produce a wideband design space through the use of the continuous class-F mode [8]. In [9] a continuous class-F mode PA has been realized using a 10W GaN HEMT and a 74% average drain efficiency was achieved over an octave bandwidth. The topic of extending the bandwidth for this LDMOS class-F is described in Chapter 6.

Fig. 2.1 shows the normalized voltage and current waveforms for class-F compared to other linear amplifiers for 3-harmonic voltage components.

With 3-harmonic voltage components, the theoretical efficiency of class-F drops to 90.7% [10].
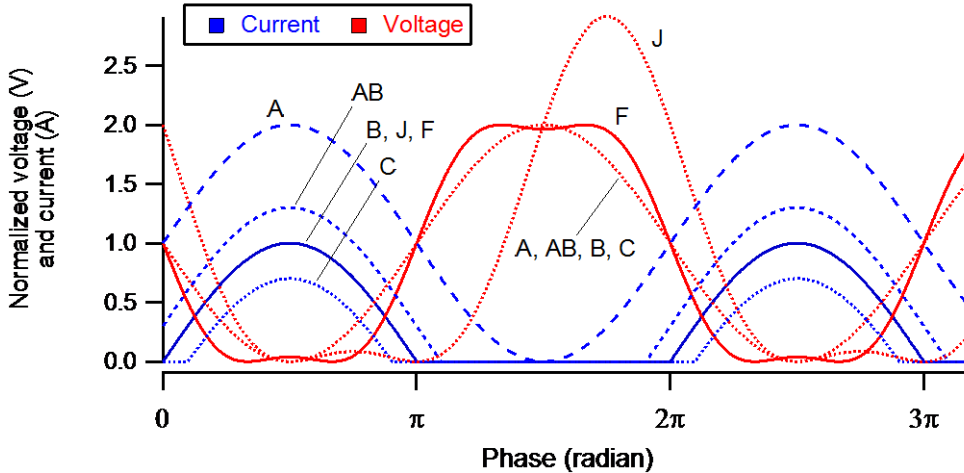


**Figure 2.1 - Normalized current and voltage waveforms for class-AB, B, C, F, J.**

### 2.2.2     Addressing Efficiency at Output Back-Off: PA Architectures

While the high-efficiency PA modes described in the previous section produce promising efficiencies, they are only efficient near peak power when the device starts to go into compression. However, when the PA operates below peak power under output back-off (OBO) conditions, the efficiency drops significantly. Fig. 2.2 shows a simulation example of a class-F PA used with a 7.5dB PAPR LTE signal. Even though it has a 75% PAE at peak power, the PA spends most of its time at average power where it is approximately 35% efficient. Therefore signals with high PAPR such as LTE and WCDMA present a challenge to a PA in maintaining efficient operation over dynamic range, as the PA spends most of its time in output back-off.

Therefore, in this backed-off region of operation, a different solution is needed to maintain the same efficiency performance achieved at peak power. Typical architectures used are Doherty, envelope tracking (ET), envelope

elimination and restoration (EER), and outphasing.  These architectural level
solutions require more than one device [11].  In this chapter the Doherty and
ET architectures are reviewed.
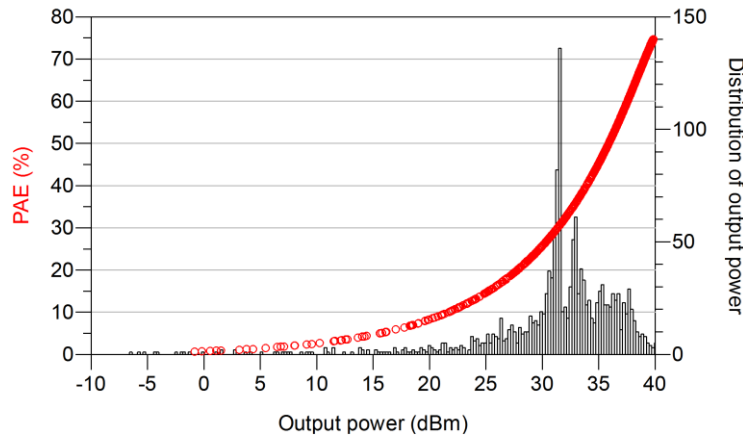


**Figure 2.2 – Simulated class-F PAE and LTE signal power distribution**

### *2.2.2.1    Doherty Power Amplifier*

The Doherty architecture was first introduced by William H. Doherty in
1936 to improve the PA efficiency in amplitude modulation (AM) broadcasting
applications [12].   The basic form of a Doherty PA consists of a carrier
amplifier, typically biased in class-AB, and a peaking amplifier biased in class-
C as shown in Fig. 2.3.  This classical structure can maintain high-efficiency
operation over 6dB OBO using the concept of load modulation [13, 14].
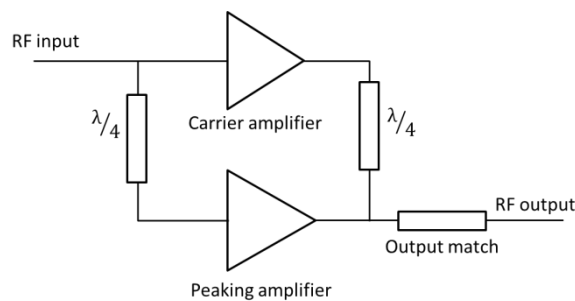


**Figure 2.3 - Basic Doherty amplifier**

At low drive levels, the peaking amplifier is turned off and the output power is contributed only by the carrier amplifier which is presented with a load of twice the devices optimum fundamental impedance ($2R_{opt}$). As the input drive level increases to power 6dB below peak power (a point often referred to as the transition point $P_T$), the carrier amplifier achieves maximum voltage swing, while the peak amplifier turns on and begins to contribute output current into the load. Increasing the drive further begins to reduce the load seen by the carrier amplifier due to the action of the impedance transformer, while, at the same time, increasing the load seen by the peaking amplifier. At peak power, both amplifiers see the same load ($R_{opt}$), and each contribute half the total output power and see a load R, if they are identical.
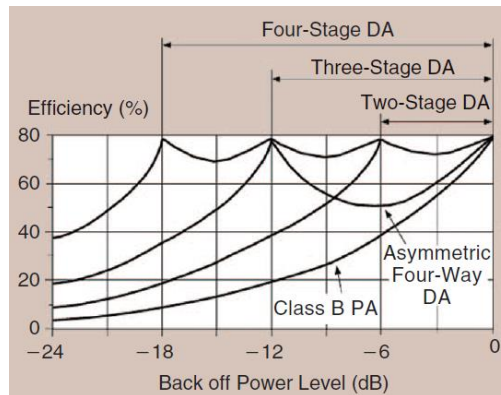


**Figure 2.4 - Efficiency plots of different Doherty amplifier configurations [13].**

The high-efficiency output range can theoretically be extended further up to 12dB OBO using a 3-way [15] or even 18dB for a 4-way Doherty as shown in Fig. 2.4 [13, 16]. An asymmetric Doherty amplifier, where the peaking device is larger than the carrier device is also used to extend the high-efficiency region as for example up to 12dB OBO as demonstrated in [17], with only a 7%-point drop over the dynamic range. The application of an 'envelope tracking' technique on the gate bias of the peaking device was presented in

15

[18] to address load modulation issues that are causing the dip in the high-efficiency region. The work in [19] addresses this dipping phenomenon by applying ET on the drain bias of the peaking device, and a relatively flat high efficiency performance was achieved over 18dB of dynamic range in a simulation environment. However the analysis did not include a fabricated hardware and the efficiency of the drain supply modulator was not considered.

The main limitation of Doherty PA is the narrow bandwidth introduced by the use of the quarter wavelength combining transformer. This presents a challenge in 4G LTE where not only the bandwidth is wider, but with carrier aggregation, PA's ideally need to accommodate multiple-bands. Research focusing on extending the bandwidth of a Doherty PA are ongoing and recent examples include [20] which is capable of handling a 100MHz instantaneous bandwidth, and [21] where a 1.5 - 2.14 GHz design was developed corresponding to a 35% fractional bandwidth.

In [22] a multiband Doherty was designed and fabricated for 1.9, 2.14, and 2.16GHz obtaining a 60% PAE at 6dB OBO. In a more recent study by Nghiem *et al.* a quad-band Doherty PA was developed at 0.96, 1.5, 2.14, and 2.16GHz, although with a relatively lower PAE at 6dB OBO, ranging from 20 to 43% [23]. There are also patented wideband and multiband Doherty PA's as shown in [24].

Doherty is currently the architecture of choice for base station power amplifiers [13], mainly because of its relative simplicity in comparison with other highly efficient solutions such as ET.

### 2.2.2.2    *Envelope Tracking Power Amplifier*

The envelope tracking (ET) architecture is inherently broadband in comparison with the Doherty, and modulates a device's DC supply according to the input envelope magnitude to improve the efficiency during output back-off.  The approach evolved from the envelope elimination and restoration (EER) amplifier technique by Kahn [25].  In ET, an envelope amplifier is used to bias the drain of the RF PA based on the input envelope signal as shown in Fig. 2.4.  The envelope information is obtained either through an envelope detector on the input path or digitally from baseband processing.   Its relationship with the drain bias voltage is defined by an *envelope shaping function* to generate the desired ET system-level efficiency shown in Fig. 2.4. The overall efficiency of an ET PA is calculated as the product of the efficiency of the RF PA and the envelope amplifier.  Therefore to improve the ET PA efficiency, careful design considerations must be given to both amplifiers.

Currently, the main constraint to implement ET in macro base stations is the lack of efficient, linear and sufficiently wideband high-power supply modulators [26].  This limitation is mainly due to the trade-off between the transistor breakdown voltage and its switching speed, hence ET implementations tend to be limited to low power applications such as mobile phones [11].  A simplified version of ET called the average power tracking (APT) is widely used for mobile phones PA's where the supply voltage is changed slowly.  However with the advancement of low-power modulators, a complete ET system is emerging as the future trend, especially with ET's ability to work over extended bandwidths and accommodate multi-band operation [11, 27].  The other issue with the ET supply modulator is that it can potentially

be a source of distortion for the RF PA. It therefore makes sense that much of the ET research focus is around the ET supply modulator, for example in [28-37].
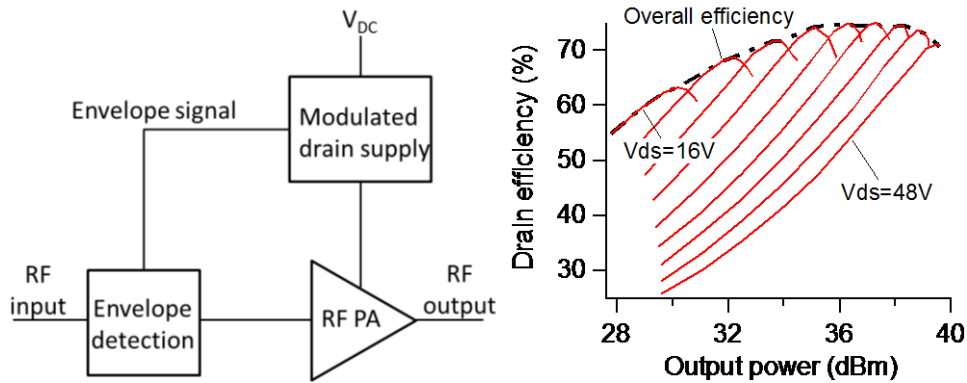


**Figure 2.5 - ET PA block diagram (left) and an example of measured efficiency plot of a class-F PA at different drain bias, or static-ET (right).**

For this research, the ET architecture is chosen instead of Doherty as the system level solution for a few reasons. Firstly ET provides more flexibility for operation in a multi-band environment compared to Doherty since the main constraint is on the envelope bandwidth as opposed to the centre frequency [11]. Secondly, to take advantage of access to a high-efficiency, medium power ET modulator supplied by Arelis through the Opera Net 2 project. The ET modulator is able to supply between 16V and 50V, which is well suited to the 50V LDMOS device used in this work. Thirdly, the waveform engineering system at Cardiff University is well suited to exploring and optimising device operation under static ET conditions, while having the ability to set up the desired harmonic mode of operation.

It is noted in literature that there are two different descriptions of how the RF PA operates to qualify as an ET PA. Earlier literatures described the RF PA in ET as operating in a linear or nearly linear state at all times,

differentiating it from polar amplifiers [5, 38-41]. In such linear operation, the modulated drain supply has minimal impact on the output envelope shape. In later literatures, the terms *envelope tracking amplifier* and *polar amplifier* are used interchangeably where the nonlinear operation of the RF PA is utilised by operating it in compression at all time for efficiency enhancement, as described in [26, 42-46].

For this research, the class-AB PA that is typically used in ET architectures is replaced with a class-F PA to boost the maximum available efficiency. In order to generate the necessary harmonic current components, class-F mode requires that the device operates in a specific degree of compression at all bias setting within the ET range. Therefore the term 'ET' used in this research includes the compressed condition in which the device operates in a nonlinear state.

## 2.3    Research Areas in Envelope Tracking Power Amplifiers

### 2.3.1    Modulated Drain Supply Generation

As this is the current limitation that is holding back ET from wide deployments in macro base stations, much of the research in ET has focused and continues to focus on the modulated bias signal path rather than on the optimisation of the RF PA within the ET architecture [47]. The DC modulation path consists of 2 main components - envelope generation and the supply modulator itself. This DC modulation topic alone is a large research area as seen in [34, 35, 48-50] and is not within the scope of this work. However, it is worth highlighting 2 recent developments in this area which are relevant to this PhD work.

The first of these is [36] where a new technique was developed for the modulated drain supply utilising a sinking current. Using this method on a class-AB PA at 889MHz, a 60% drain efficiency was achieved for a 6.5dB PAPR 10MHz LTE signal at 40.2dBm output power. The results obtained here are under similar conditions used for this PhD work, namely the frequency, output power, and the signal PAPR. Furthermore, one of the objectives of this PhD work is to compare the performance of the traditional class-AB implementation in ET with class-F, as described in Chapters 3 and 4. Therefore the work in [36] provides a good baseline, even though it uses a GaN device instead of LDMOS.

The second relevant piece of work in this modulator topic is the work presented by Yusoff in [51, 52] where a simple and low-cost technique to generate the modulated drain supply called auxiliary envelope tracking (AET) was presented. In this technique the DC and AC components of the modulated drain supply are generated separately and a broadband RF transformer is used to combine them and dynamically bias the device. The magnitude and phase of the envelope amplifier output which amplifies the AC path can be varied to reduce IM3 distortion products. The limitation in this technique, as published, is the limited flexibility in controlling the envelope shaping function and the limited dynamic range of the detector diode. One of the objectives of this PhD work is to use ET as a linearising method using the envelope shaping function which would address the limitations described above, and shall be discussed in Chapters 4 and 5.

**2.3.2      Use of High-Efficiency Modes in Envelope Tracking PA**

The RF PA in an ET system typically operates in class-AB mode due to its linearity advantage [28].  However other high-efficiency modes of operation have been used in an ET architecture that are discussed in literature.  In [53] a class-F$^{-1}$ mode is used on a GaN HEMT device optimised for an ET architecture achieving more than 70% efficiency over a bandwidth of 920-960MHz.  However the measured efficiency was of the RF PA alone without the drain modulator, obtained from CW measurements at individual drain bias points.

Alavi et al. used a class-B and class-J* "hybrid" in an ET setting in [44], utilising the drain-to-source capacitance ($C_{DS}$) variation with drain voltage to tune the fundamental and 2$^{nd}$ harmonic impedances between the 2 PA modes. A static ET experiment where CW measurements were made at individual drain bias points using load-pull on a 2W LDMOS device at 2.14GHz achieved an average PAE of 64% at 7.8dB output back-off.  However once again this is only the efficiency of the RF PA alone under CW excitation.  The actual ET dynamic bias effect was not observed and the efficiency of the drain supply modulator was not included.

The class-J mode PA was also used by Kimball et al. in an ET system in [45], this time in combination with a class-E type of operation using a GaN HFET for a W-CDMA base station.  Using a signal with 7.67dB PAPR, the average combined efficiency for both the RF PA and the drain modulator was 50.7% at 37.2W average output power.  This is another good baseline reference for comparison with this PhD work.

In [46] Kim et al. presented the use of a class-$F^{-1}$ mode, fully integrated with an ET modulator for a 3G LTE base station design using a 60W peak power GaN device, achieving 44% drain efficiency at 3.54GHz. However, it is observed that the class-$F^{-1}$ GaN RF PA efficiency before ET was already below 60%. This PhD work aims to use the waveform engineering system [54] to systematically optimise the RF PA design for ET applications to achieve a higher baseline efficiency as demonstrated in [55] for a class-$F^{-1}$, and this is described in Chapter 4.

In [56] a class-$F^{-1}$ PA in ET was developed using GaN MMIC at 10GHz. With the RF PA optimised for efficiency at average power and trading-off the efficiency at peak power, the average efficiency achieved with an ET modulator was 54.4% for a 6.6dB PAPR LTE signal. The RF PA optimisation was done through fundamental load-pull while the harmonic terminations were determined from simulations.

### 2.3.3    Use of LDMOS in ET

In high-power ET applications outlined in the previous section, GaN devices are typically used in preference to LDMOS. The large output capacitance ($C_{DS}$) and on-resistance ($R_{ON}$) associated with LDMOS causes reduced efficiency in comparison to GaN. However, the low cost of LDMOS makes it an attractive solution for <3GHz applications and as of 2014 it accounted for 95% of the base station market [26]. Previous ET PA realisations that utilised LDMOS devices as the RF PA obtained lower efficiency numbers compared to their GaN counterpart. For example in [29] the achieved average PAE was 40% for a 7.6dB-PAPR 3.84MHz-bandwidth W-CDMA signal at 27W output power. However, this was obtained with a

64%-efficient RF PA that was optimised at peak power. The use of a highly-efficient PA mode with harmonic termination optimised at average power could have increased this efficiency further.

In [57] a static ET evaluation from CW measurements was performed on a 10W LDMOS device, this time with 2nd harmonic tuning for efficiency optimisation of a class-AB operation at 2.14GHz. The drain efficiency obtained from this technique was 50% for approximately 5dB of input power back-off. However, this number is for the RF PA alone and a full ET system test was not performed.

### 2.3.4    PA Linearisation using Baseband Injection for ET Applications

The linearity aspect of a PA in some applications takes precedence over efficiency, such as those used for base stations due to stringent regulations in spectral interference [5]. Almost all of the ET PAs described above rely heavily on digital pre-distortion (DPD) to achieve the necessary linearity. It should be remembered however that DPD should be considered as 'the last resort' in linearising a PA [58] and designing PAs with maximum 'raw' linearity while still remaining highly efficient remains the ultimate objective.

The linearity performance of a transistor device technology, such as LDMOS, is heavily affected by the impedance presented at baseband frequencies [59]. The usual solution to this is careful design of bias networks that present very low, ideally short-circuit impedances to baseband components. It has been shown however in [60] that it is possible to improve the linearity of a transistor by injecting a baseband signal into the output of the device operating in a compressed state. The injected baseband signal will

produce mixing products and depending on the magnitude and phase of the baseband signal, the mixing products have the potential to cancel out odd-order intermodulation products of the PA.  It makes sense therefore to explore the idea of achieving such linearity improvement and efficiency enhancement simultaneously through the application of specific ET signals.

The use of waveform engineering in investigating AM-AM linearisation methods for PAs was first shown in [61] using an active IF load-pull system where the linearising baseband signal was presented in the form of a negative impedance that lies outside the Smith chart.  This impedance, when presented to a drain of a 10W GaN device, was able to suppress the $3^{rd}$ and $5^{th}$ order intermodulation products under modulated excitations [62].  Further work in [63] developed a systematic formulation of the even-order baseband coefficients to suppress the intermodulation products of a class-AB mode PA operating in compression, which was shown to be independent of envelope complexity [64], envelope bandwidth [65], and FET device technology [66]. The engineered injected baseband signal linearises the device transconductance, which is derived from the relationship between the output drain current versus the input voltage [67].

In terms of implementation, the previous work of baseband injection in [61-66] used arbitrary waveform generators (AWG) to independently generate the baseband signal and combine it with the DC bias through a diplexer at the drain for PA linearisation.  This is possible as long as the input envelope signal shape is repetitive, known and well-defined, as would be the case for example if the RF input excitation is constructed using discrete tones.  However when complex, continuous modulation schemes such as LTE and W-CDMA signals

are used, while the linearising baseband transfer function and formulated coefficients still hold, the time-domain baseband signal itself cannot be easily generated independently with an AWG and be made coherent with the random input envelope, but rather it must be sampled off the input. In an ET system, that linearising baseband transfer function takes the form of an envelope shaping function of the drain supply modulator.

While the intended purpose of the aforementioned research work was ET implementation, the effect of the baseband injection on efficiency was not previously investigated due to the unavailability of an ET modulator. Therefore, this PhD work aims to 'close the loop' of that study by investigating the possibility of using ET as a baseband injection signal simultaneously for PA linearisation and analyse its trade-off with efficiency.

## 2.4      State-of-the-Art Envelope Tracking Power Amplifiers

Recent works in this field have produced further improved efficiency numbers or higher frequency of operation. In [68] a GaN device operating in class-AB was used in ET at 780MHz by Yan et al. The measured drain efficiencies were 69% and 60% for a 6.6dB-PAPR 5MHz-bandwidth 29W-power WCDMA and a 7.5dB-PAPR 10MHz-bandwidth 23W-power LTE signal, respectively.

A GaN HEMT operating in class-E is used in [69] in an ET system at 2.6GHz. With the RF PA having a drain efficiency of 74% and the ET modulator at 92% efficiency, the overall ET efficiency was 60% when a 6.5dB PAPR 10MHz LTE signal was applied producing a 40W average output power.

In [70] an ET PA utilising a GaN device operating in inverse class-F at 880MHz was able to produce a PAE of 53% at 7.4W output power for a 6.6dB PAPR 20MHz LTE signal.

A higher bandwidth was achieved in [71] where an X-band GaN MMIC PA was used in ET for a 60MHz LTE signal with 6.6dB PAPR. With the RF PA operating in class-E at 9.23GHz, the overall PAE achieved was 35% at 1.1W average output power.

These state-of-the-art ET PA's shall be used as a benchmark for the ET PA developed in this PhD work.

## 2.5      Conclusions & New Research Opportunities

Envelope tracking is a well-covered topic in research with the introduction of 4G LTE and heterogeneous networks. Wideband and multiband operations present a challenge for the current practice in base stations where the current standard Doherty amplifiers are widely used. Although the research in ET is well-covered, there are still opportunities for new research areas within the ET field, and for this PhD work to address some gaps in the literature.

The first research opportunity is the use of a high-voltage LDMOS device technology in ET. Most ET implementations use GaN devices, except for a small few, and the ones that used LDMOS did not achieve high efficiency numbers with conventional class-AB mode.

The second opportunity is the use of class-F mode in ET. As described in Section 2.3.2, ET typically uses class-AB PA's and most of the work

involving high-efficiency modes in ET used class-F$^{-1}$ mode.  The only work that the author is aware of using class-F in ET at the time of writing is [72] where a continuous-mode class-F approach is proposed.   However, that work only presented simulation results and no actual measurements were performed.

Thirdly, there is an opportunity to fully research the use of continuous mode PA's in ET as this has not been analysed in detail and tested with a hardware before.  This is a new topic and presents an attractive solution for wideband ET implementation, if successful.  It is also interesting to understand how such structures would respond to baseband linearisation, within an ET environment.

The fourth opportunity is to use waveform engineering to optimise the RF PA in an ET system.  This approach has been successfully used in high-efficiency and high-bandwidth PA design as well as device characterisation and modelling previously, but has not been used in designing an RF PA for ET applications.

## 2.6      References

[1]     R. Caverly, F. Raab, and J. Staudinger, "High-Efficiency Power Amplifiers," *Microwave Magazine, IEEE,* vol. 13, pp. S22-S32, 2012.

[2]     L. M. Correia, D. Zeller, O. Blume, D. Ferling, Y. Jading, G. I*, et al.*, "Challenges and enabling technologies for energy aware mobile radio networks," *IEEE Communications Magazine,* vol. 48, pp. 66-72, 2010.

[3]     G. Koutitas and P. Demestichas, "A Review of Energy Efficiency in Telecommunication Networks," *Telfor Journal,* vol. 2, 2010.

[4]     M. Eron, B. Kim, F. Raab, R. Caverly, and J. Staudinger, "The Head of the Class," *Microwave Magazine, IEEE,* vol. 12, pp. S16-S33, 2011.

[5]     S. C. Cripps, *RF Power Amplifiers for Wireless Communications*: Artech House, 2006.

[6]     N. O. Sokal, "RF power amplifiers-classes A through S," in *Electro/95 International. Professional Program Proceedings.*, 1995, pp. 335-400.

[7]     A. Sheikh, C. Roff, J. Benedikt, P. J. Tasker, B. Noori, J. Wood*, et al.*, "Peak Class F and Inverse Class F Drain Efficiencies Using Si LDMOS in a Limited Bandwidth Design," *IEEE Microwave and Wireless Components Letters,* vol. 19, pp. 473-475, 2009.

[8]     V. Carrubba, A. L. Clarke, M. Akmal, J. Lees, J. Benedikt, P. J. Tasker*, et al.*, "The Continuous Class-F Mode Power Amplifier," in *Microwave Conference (EuMC), 2010 European*, 2010, pp. 1674-1677.

[9]     V. Carrubba, J. Lees, J. Benedikt, P. J. Tasker, and S. C. Cripps, "A novel highly efficient broadband continuous class-F RFPA delivering 74% average efficiency for an octave bandwidth," in *Microwave Symposium Digest (MTT), 2011 IEEE MTT-S International*, 2011, pp. 1-4.

[10]    F. H. Raab, "Maximum efficiency and output of class-F power amplifiers," *IEEE Transactions on Microwave Theory and Techniques,* vol. 49, pp. 1162-1166, 2001.

[11]    P. Asbeck and Z. Popovic, "ET Comes of Age: Envelope Tracking for Higher-Efficiency Power Amplifiers," *Microwave Magazine, IEEE,* vol. 17, pp. 16-25, 2016.

[12]    W. H. Doherty, "A New High Efficiency Power Amplifier for Modulated Waves," *Proceedings of the Institute of Radio Engineers,* vol. 24, pp. 1163-1182, 1936.

[13]    R. Pengelly, C. Fager, and M. Ozen, "Doherty's Legacy: A History of the Doherty Power Amplifier from 1936 to the Present Day," *IEEE Microwave Magazine,* vol. 17, pp. 41-58, 2016.

[14]    B. Kim, K. Ildu, and M. Junghwan, "Advanced Doherty Architecture," *Microwave Magazine, IEEE,* vol. 11, pp. 72-86, 2010.

[15]    F. H. Raab, "Efficiency of Doherty RF Power-Amplifier Systems," *IEEE Transactions on Broadcasting,* vol. BC-33, pp. 77-83, 1987.

[16]    K. J. Cho, W. J. Kim, J. Y. Kim, J. H. Kim, and S. P. Stapleton, "N-Way Distributed Doherty Amplifier with an Extended Efficiency Range," in *2007 IEEE/MTT-S International Microwave Symposium*, 2007, pp. 1581-1584.

[17]    M. Iwamoto, A. Williams, C. Pin-Fan, A. G. Metzger, L. E. Larson, and P. M. Asbeck, "An extended Doherty amplifier with high efficiency over a wide power range," *IEEE Transactions on Microwave Theory and Techniques,* vol. 49, pp. 2472-2479, 2001.

[18]     K. Ildu and B. Kim, "A 2.655 GHz 3-stage Doherty power amplifier using envelope tracking technique," in *Microwave Symposium Digest (MTT), 2010 IEEE MTT-S International*, 2010, pp. 1496-1499.

[19]     M. Thian, P. Gardner, M. Thian, and P. Gardner, "Envelope-tracking-based Doherty power amplifier," *International Journal of Electronics,* vol. 97, pp. 525-530, 5 2010.

[20]     C. Ma, W. Pan, S. Shao, C. Qing, and Y. Tang, "A Wideband Doherty Power Amplifier With 100 MHz Instantaneous Bandwidth for LTE-Advanced Applications," *IEEE Microwave and Wireless Components Letters,* vol. 23, pp. 614-616, 2013.

[21]     K. Bathich, A. Z. Markos, and G. Boeck, "A wideband GaN Doherty amplifier with 35 % fractional bandwidth," in *Microwave Conference (EuMC), 2010 European*, 2010, pp. 1006-1009.

[22]     A. M. M. Mohamed, S. Boumaiza, and R. R. Mansour, "Reconfigurable Doherty Power Amplifier for Multifrequency Wireless Radio Systems," *IEEE Transactions on Microwave Theory and Techniques,* vol. 61, pp. 1588-1598, 2013.

[23]     X. A. Nghiem, J. Guan, T. Hone, and R. Negra, "Design of Concurrent Multiband Doherty Power Amplifiers for Wireless Applications," *IEEE Transactions on Microwave Theory and Techniques,* vol. 61, pp. 4559-4568, 2013.

[24]     A. Grebennikov and S. Bulja, "High-Efficiency Doherty Power Amplifiers: Historical Aspect and Modern Trends," *Proceedings of the IEEE,* vol. 100, pp. 3190-3219, 2012.

[25]     L. R. Kahn, "Single-Sideband Transmission by Envelope Elimination and Restoration," *Proceedings of the IRE,* vol. 40, pp. 803-806, 1952.

[26]     Z. Wang, *Envelope Tracking Power Amplifiers for Wireless Communications*: Artech House, 2014.

[27]     B. Kim, "Advanced linear PA architectures for handset applications," in *Wireless Symposium (IWS), 2013 IEEE International*, 2013, pp. 1-1.

[28]     K. Bumman, M. Junghwan, and K. Ildu, "Efficiently Amplified," *Microwave Magazine, IEEE,* vol. 11, pp. 87-100, 2010.

[29]     P. Draxler, S. Lanfranco, D. Kimball, C. Hsia, J. Jeong, J. van de Sluis*, et al.*, "High Efficiency Envelope Tracking LDMOS Power Amplifier for W-CDMA," in *Microwave Symposium Digest, 2006. IEEE MTT-S International*, 2006, pp. 1534-1537.

[30]     J. Jeong, D. F. Kimball, M. Kwak, P. Draxler, C. Hsia, C. Steinbeiser*, et al.*, "High-Efficiency WCDMA Envelope Tracking Base-Station Amplifier

Implemented with GaAs HVHBTs," *IEEE Journal of Solid-State Circuits,* vol. 44, pp. 2629-2639, 2009.

[31]    I. Kim, J. Kim, J. Moon, and B. Kim, "Optimized Envelope Shaping for Hybrid EER Transmitter of Mobile WiMAX - Optimized ET Operation," *IEEE Microwave and Wireless Components Letters,* vol. 19, pp. 335-337, 2009.

[32]    D. Kimball, P. Draxler, J. Jeong, C. Hsia, S. Lanfranco, W. Nagy*, et al.*, "50% PAE WCDMA basestation amplifier implemented with GaN HFETs," in *IEEE Compound Semiconductor Integrated Circuit Symposium, 2005. CSIC '05.*, 2005, p. 4 pp.

[33]    D. Kimball, J. J. Yan, P. Theilmanrr, M. Hassan, P. Asbeck, and L. Larson, "Efficient and wideband envelope amplifiers for envelope tracking and polar transmitters," in *Power Amplifiers for Wireless and Radio Applications (PAWR), 2013 IEEE Topical Conference on*, 2013, pp. 13-15.

[34]    V. Yousefzadeh, E. Alarcon, and D. Maksimovic, "Three-level buck converter for envelope tracking applications," *IEEE Transactions on Power Electronics,* vol. 21, pp. 549-552, 2006.

[35]    M. Vasic, P. Cheng, O. Garcia, J. A. Oliver, P. Alou, J. A. Cobos*, et al.*, "The Design of a Multilevel Envelope Tracking Amplifier Based on a Multiphase Buck Converter," *IEEE Transactions on Power Electronics,* vol. 31, pp. 4611-4627, 2016.

[36]    J. Kim, J. Moon, J. Son, S. Jee, J. Lee, J. Cha*, et al.*, "Highly efficient envelope tracking transmitter by utilizing sinking current," in *Microwave Conference (EuMC), 2011 41st European*, 2011, pp. 1197-1200.

[37]    W. Zhancang, "Demystifying Envelope Tracking: Use for High-Efficiency Power Amplifiers for 4G and Beyond," *Microwave Magazine, IEEE,* vol. 16, pp. 106-129, 2015.

[38]    C. Buoli, A. Abbiati, and D. Riccardi, "Microwave power amplifier with "envelope controlled" drain power supply," in *Microwave Conference, 1995. 25th European*, 1995, pp. 31-35.

[39]    G. Hanington, C. Pin-Fan, P. M. Asbeck, and L. E. Larson, "High-efficiency power amplifier using dynamic power-supply voltage for CDMA applications," *IEEE Transactions on Microwave Theory and Techniques,* vol. 47, pp. 1471-1476, 1999.

[40]    E. McCune, "Envelope Tracking or Polar - Which Is It? [Microwave Bytes]," *IEEE Microwave Magazine,* vol. 13, pp. 34-56, 2012.

[41]    E. McCune, *Dynamic Power Supply Transmitters*: Cambridge University Press, 2015.

[42]    G. F. Collins, J. Wood, and B. Woods, "Challenges of power amplifier design for envelope tracking applications," in *Power Amplifiers for Wireless and Radio Applications (PAWR), 2015 IEEE Topical Conference on*, 2015, pp. 1-3.

[43]    K. Bumman, K. Jungjoon, K. Dongsu, S. Junghwan, C. Yunsung, K. Jooseung*, et al.*, "Push the Envelope: Design Concepts for Envelope-Tracking Power Amplifiers," *Microwave Magazine, IEEE,* vol. 14, pp. 68-81, 2013.

[44]    M. S. Alavi, F. van Rijs, M. Marchetti, M. Squillante, T. Zhang, S. J. Theeuwen*, et al.*, "Efficient LDMOS device operation for envelope tracking amplifiers through second harmonic manipulation," in *Microwave Symposium Digest (MTT), 2011 IEEE MTT-S International*, 2011, pp. 1-1.

[45]    D. F. Kimball, J. Jeong, H. Chin, P. Draxler, S. Lanfranco, W. Nagy*, et al.*, "High-Efficiency Envelope-Tracking W-CDMA Base-Station Amplifier Using GaN HFETs," *Microwave Theory and Techniques, IEEE Transactions on,* vol. 54, pp. 3848-3856, 2006.

[46]    J. H. Kim, G. D. Jo, J. H. Oh, Y. H. Kim, K. C. Lee, J. H. Jung*, et al.*, "High-Efficiency Envelope-Tracking Transmitter With Optimized Class-F-1 Amplifier and 2-bit Envelope Amplifier for 3G LTE Base Station," *IEEE Transactions on Microwave Theory and Techniques,* vol. 59, pp. 1610-1621, 2011.

[47]    G. F. Collins, J. Fisher, F. Radulescu, J. Barner, S. Sheppard, R. Worley*, et al.*, "Power Amplifier Design Optimized for Envelope Tracking," in *Compound Semiconductor Integrated Circuit Symposium (CSICs), 2014 IEEE*, 2014, pp. 1-4.

[48]    Q. Jin, X. Ruan, X. Ren, Y. Wang, Y. Leng, and C. Tse, "Series-Parallel Form Switch-Linear Hybrid Envelope-Tracking Power Supply to Achieve High Efficiency," *IEEE Transactions on Industrial Electronics,* vol. PP, pp. 1-1, 2016.

[49]    V. I. Kumar and S. Kapat, "Mixed-signal hysteretic internal model control of buck converters for ultra-fast envelope tracking," in *2016 IEEE Applied Power Electronics Conference and Exposition (APEC)*, 2016, pp. 3224-3230.

[50]    J. S. Paek, Y. S. Youn, J. H. Choi, D. S. Kim, J. H. Jung, Y. H. Choo*, et al.*, "An RF-PA supply modulator achieving 83% efficiency and -136dBm/Hz noise for LTE-40MHz and GSM 35dBm applications," in *2016 IEEE International Solid-State Circuits Conference (ISSCC)*, 2016, pp. 354-355.

[51]    Z. Yusoff, J. Lees, J. Benedikt, P. J. Tasker, and S. C. Cripps, "Linearity improvement in RF power amplifier system using integrated

Auxiliary Envelope Tracking system," in *Microwave Symposium Digest (MTT), 2011 IEEE MTT-S International*, 2011, pp. 1-4.

[52]    Z. Yusoff, J. Lees, M. A. Chaudhary, V. Carrubba, C. Heungjae, P. Tasker*, et al.*, "Simple and low-cost tracking generator design in envelope tracking radio frequency power amplifier system for WCDMA applications," *Microwaves, Antennas & Propagation, IET,* vol. 7, pp. 802-808, 2013.

[53]    W. Zhancang, "A class-F-1 GaN HEMT power amplifier optimized for envelope tracking with gain-efficiency trajectory analysis and comparison," in *Microwaves, Communications, Antennas and Electronics Systems (COMCAS), 2013 IEEE International Conference on*, 2013, pp. 1-4.

[54]    P. J. Tasker, "Practical waveform engineering," *Microwave Magazine, IEEE,* vol. 10, pp. 65-76, 2009.

[55]    P. Wright, A. Sheikh, C. Roff, P. J. Tasker, and J. Benedikt, "Highly efficient operation modes in GaN power transistors delivering upwards of 81% efficiency and 12W output power," in *Microwave Symposium Digest, 2008 IEEE MTT-S International*, 2008, pp. 1147-1150.

[56]    G. Collins, J. Fisher, F. Radulescu, J. Barner, S. Sheppard, R. Worley*, et al.*, "C-band and X-band class F, F-1 GaN MMIC PA design for envelope tracking systems," in *Microwave Conference (EuMC), 2015 European*, 2015, pp. 1172-1175.

[57]    E. Cipriani, P. Colantonio, F. Giannini, R. Giofre, and L. Piazzon, "Envelope Tracking Technique Applied on a 10W 2(nd) Harmonic Tuned Power Amplifier at 2.14 GHz," *2009 European Microwave Conference, Vols 1-3,* pp. 1429-1432, 2009.

[58]    R. S. Pengelly, W. Pribble, and T. Smith, "Inverse Class-F Design Using Dynamic Loadline GaN HEMT Models to Help Designers Optimize PA Efficiency [Application Notes]," *Microwave Magazine, IEEE,* vol. 15, pp. 134-147, 2014.

[59]    J. Brinkhoff and A. E. Parker, "Effect of baseband impedance on FET intermodulation," *Microwave Theory and Techniques, IEEE Transactions on,* vol. 51, pp. 1045-1051, 2003.

[60]    J. Brinkhoff, A. E. Parker, and M. Leung, "Baseband impedance and linearization of FET circuits," *Microwave Theory and Techniques, IEEE Transactions on,* vol. 51, pp. 2523-2530, 2003.

[61]    J. Lees, M. Akmal, S. Bensmida, S. Woodington, S. Cripps, J. Benedikt*, et al.*, "Waveform engineering applied to linear-efficient PA design," in *Wireless and Microwave Technology Conference (WAMICON), 2010 IEEE 11th Annual*, 2010, pp. 1-5.

[62]     M. Akmal, V. Carrubba, J. Lees, S. Bensmida, J. Benedikt, K. Morris*, et al.*, "Linearity enhancement of GaN HEMTs under complex modulated excitation by optimizing the baseband impedance environment," in *Microwave Symposium Digest (MTT), 2011 IEEE MTT-S International*, 2011, pp. 1-4.

[63]     F. L. Ogboi, P. J. Tasker, M. Akmal, J. Lees, J. Benedikt, S. Bensmida*, et al.*, "A LSNA configured to perform baseband engineering for device linearity investigations under modulated excitations," in *Microwave Conference (EuMC), 2013 European*, 2013, pp. 684-687.

[64]     F. L. Ogboi, P. J. Tasker, M. Akmal, J. Lees, J. Benedikt, S. Bensmida*, et al.*, "Investigation of Various Envelope Complexity Linearity under Modulated Stimulus Using a New Envelope Formulation Approach," in *Compound Semiconductor Integrated Circuit Symposium (CSICs), 2014 IEEE*, 2014, pp. 1-4.

[65]     F. L. Ogboi, P. J. Tasker, M. Akmal, J. Lees, J. Benedikt, S. Bensmida*, et al.*, "High bandwidth investigations of a baseband linearization approach formulated in the envelope domain under modulated stimulus," in *Microwave Conference (EuMC), 2014 44th European*, 2014, pp. 1305-1308.

[66]     F. L. Ogboi, P. Tasker, Z. Mohkti, J. Lees, J. Benedikt, S. Bensmida*, et al.*, "Sensitivity of AM/AM linearizer to AM/PM distortion in devices," in *Microwave Measurement Conference (ARFTG), 2014 83rd ARFTG*, 2014, pp. 1-4.

[67]     F. Chun-Wah and K. K. M. Cheng, "Theoretical and experimental study of amplifier linearization based on harmonic and baseband signal injection technique," *Microwave Theory and Techniques, IEEE Transactions on,* vol. 50, pp. 1801-1806, 2002.

[68]     J. J. Yan, P. Theilmann, and D. F. Kimball, "A High Efficiency 780 MHz GaN Envelope Tracking Power Amplifier," in *2012 IEEE Compound Semiconductor Integrated Circuit Symposium (CSICS)*, 2012, pp. 1-4.

[69]     H. Tango, T. Hashinaga, K. Totani, H. Kuriyama, Y. Hamada, and T. Asaina, "A 60% efficient envelope tracking PA for 40W, 2.6GHz LTE base station with in/output harmonic tuning," in *Microwave Symposium Digest (IMS), 2013 IEEE MTT-S International*, 2013, pp. 1-4.

[70]     Y. Liu, C. S. Yoo, J. Fairbanks, J. Yan, D. Kimball, and P. Asbeck, "A 53% PAE envelope tracking GaN power amplifier for 20MHz bandwidth LTE signals at 880MHz," in *2016 IEEE Topical Conference on Power Amplifiers for Wireless and Radio Applications (PAWR)*, 2016, pp. 30-32.

[71]     P. T. Theilmann, J. J. Yan, C. Vu, J. S. Moon, H. P. Moyer, and D. F. Kimball, "A 60MHz Bandwidth High Efficiency X-Band Envelope

Tracking Power Amplifier," in *2013 IEEE Compound Semiconductor Integrated Circuit Symposium (CSICS)*, 2013, pp. 1-4.

[72]    B. Merrick and T. J. Brazil, "Analysis of the integration of envelope tracking with Continuous Class F amplifiers," in *Integrated Nonlinear Microwave and Millimetre-Wave Circuits (INMMIC), 2012 Workshop on*, 2012, pp. 1-3.

# Chapter 3

# Class-F Power Amplifier Behaviour in a Variable Drain Bias Setting

## 3.1    Introduction

In the previous chapter, the efficiency aspect of a power amplifier (PA) is discussed in two types of implementation, firstly improving the efficiency at peak power using high efficiency *modes* and secondly improving efficiency during output back-off (OBO) through the use of high-efficiency *architectures*. This research work focuses on integrating a high efficiency mode, namely class-F into a high-efficiency architecture, namely envelope tracking (ET). Such integration starts with analysing the behaviour of a class-F mode PA in a variable drain bias setting, which is the focus of this chapter.

The first objective of this chapter is to analyse the requirements for maintaining a class-F PA mode in a variable drain setting which represents an envelope tracking environment, and to understand the impact of the variation in device output capacitance ($C_{DS}$) with drain supply on efficiency when the class-F amplifier impedance environment is optimised at a single drain bias ($V_{DS}$) setting.

The second objective is to analyse the linearity performance of different PA modes in an ET environment, and the possible trade-offs with efficiency

through the use of different envelope shaping functions. The experimental investigation of these effects on class-AB and class-F PA modes is performed using a 10W LDMOS device. The use of waveform engineering to formulate a shaping function to linearise the ET PA is then compared to previous work of using baseband injection as a PA linearising method [1].

This chapter begins by describing the measurement system and device under test used in this work. This is followed by the investigation of class-F behaviour in ET, with simulation and experimental results. The subsequent experiment then looks at what is achievable and the trade-offs possible when using different shaping functions, followed by a discussion on the comparison with baseband injection work. A comparison with class-AB mode of operation is shown in each experiment, as it is the current PA mode usually used in ET PAs [2].

## 3.2      Measurement System and Device under Test

### 3.2.1      Waveform Engineering Measurement System

The waveform engineering approach [3] which was developed at Cardiff University uses an active load-pull system to construct the desired current and voltage waveforms at the transistor's intrinsic current generator plane. This is achieved by synthesizing the required fundamental and harmonic load impedances at any bias point, hence setting up any PA mode of operation. This can be thought of as emulating a harmonic balance simulation through actual measurement [4].

The active load-pull measurement system is described in detail in Appendix A. It is based around an Agilent N5242A PNA-X Nonlinear Vector

Network Analyser (NVNA) as a receiver. The load-pull system is run using the *Mesuro* software environment which enables 3-harmonic load search, multi-parameter sweeps, and 3 layers of de-embedding. No input matching was applied on the device input side in this research work, instead the input drive level was increased accordingly to overcome the mismatch losses to arrive at the desired delivered input power level. The fundamental frequency for this work was set at 900MHz.
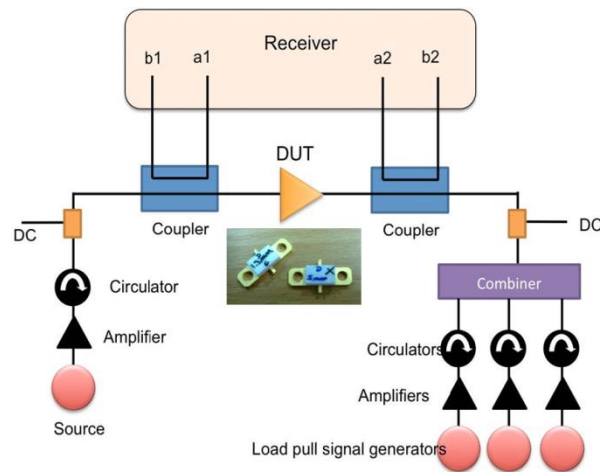


**Figure 3.1 - Active load-pull system and the device under test**

### 3.2.2    Device under Test and De-embedding

The transistor device used in this work was a packaged 10W high voltage LDMOS (HVLDMOS) from Freescale (now NXP) with a gate width of 5.2 mm. As it was a test device made for this research work, it only had a single bond wire each at the gate and the drain. The knee voltage was approximately 10V while its maximum operating drain voltage of 50V provided higher output impedance compared to a 30V device of the same power capacity. To avoid the knee and breakdown regions, the ET drain bias range was defined to be from 16V to 48V in 4V steps. Hence there were 9 static ET

bias points where the measurements were performed, namely: 16V, 20V, 24V, 28V, 32V, 36V, 40, 44V, and 48V.

The device model used in Keysight ADS simulation software was provided by Freescale.   The device static $C_{DS}$ values for different drain voltages was also provided, which therefore enabled a static de-embedding process from the device package to the device current generator plane for a particular bias.   The model was found to correlate well with the actual device and this verification process is described in more detail in Appendix A.

For load-pull measurements that involved drain bias variation, a two-layer de-embedding approach was used to obtain the waveform information at the device current generator plane.   The first layer was a fixed de-embedding that includes the test fixture and the device package.   The second layer was a bias-dependent de-embedding to cater for the changing $C_{DS}$ value with the applied drain bias.   For this work the feedback capacitance between the gate and the drain ($C_{GD}$) was not considered as the value was too small and can be neglected.

## 3.3     Maintaining Class-F in a Variable Drain Setting

This section investigates the requirement in maintaining a class-F PA in a variable drain setting and the efficiency degradation when it is optimised at one bias point due to the device output capacitance ($C_{DS}$).

### 3.3.1     Methodology

For this analysis, three scenarios were investigated in order to understand the impact of $C_{DS}$ on drain efficiency in an ET setting. Firstly, when the class-F fundamental impedance environment was optimised at each drain

voltage throughout the ET range (best case scenario); secondly, when the class-F mode was optimised at the maximum drain voltage of 48V; and thirdly, when the class-F mode was optimised at a static value of $V_{DS}$=28V, which represents an average voltage value during output back-off condition where the class-F PA would spend most of its time, as demonstrated in [5] for an LTE signal.  A similar approach was used in [6], but with a class-B/J mode and only addressed the first two scenarios, namely optimised at each drain voltage and at maximum drain voltage.

To optimise a class-F impedance at any drain bias point, a load-pull search was performed to find the optimum load for efficiency at 1dB compression level.  The constant compression level was chosen in this experiment as it provided a standardised search criterion and was close to the maximum efficiency point.  Using the appropriate $C_{DS}$ de-embedding (an example is described in Appendix A), the load-pull system was then used to engineer the class-F voltage and current waveforms at the device current generator plane.  The desired class-F waveforms were established for each optimisation step – thus it can be said that the class-F operational condition established through waveform engineering and dynamic load-line manipulation relative to the I-V space, provided a very robust way of normalizing the measurement, and demonstrating that class-F operation was being maintained at different bias levels.

Finally, the experiment was repeated on a class-AB mode using the same method and scenarios.  For this mode the gate was biased such that the quiescent point was at approximately 3% of the device's maximum current to retain a high efficiency number.  The 2nd harmonic output current was shorted

at the current generator plane and no load-pull was performed on the 3$^{rd}$ harmonic.

### 3.3.2    Results and Discussions

### *3.3.2.1    Class-F in ET Optimised at Individual $V_{DS}$ (Best Case Scenario)*

This scenario is important as it provides the best-case performance that would result if the output matching network could somehow dynamically adjust along with the rapidly changing drain voltage.  For this scenario, a different de-embedding value was used for each drain voltage, according to the dynamic $C_{DS}$-$V_{DS}$ relationship to cater for the variation in $C_{DS}$.
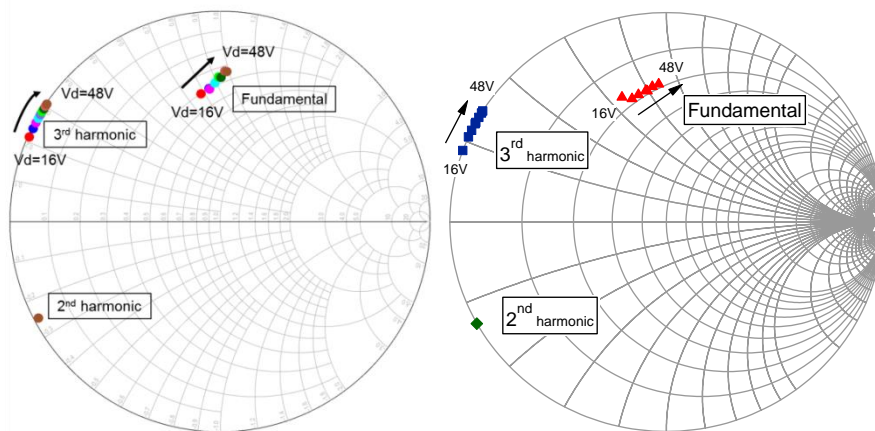


**Figure 3.2 - Optimum load trajectory at the device package plane from simulation (left) and measurement (right).**

Fig. 3.2 shows how these individual impedances optimised at the current generator plane translated into impedances at the device package plane, both from simulation and measurement.  The arrows show the movement of the package-plane load impedances as drain voltage is increased.  These were the measured impedances that the packaged device needed to 'see' in order to maintain a class-F mode of operation throughout

40

the ET range. This is useful as it gives a measure of the magnitude of change required when optimising for different modulation schemes for example.

The load-pull grid resolution used in measurements and simulation limited the accuracy of the optimum load locations; however the Smith charts present the trend of the load trajectory at the package plane. There were 2 factors that affected the shift of the optimum fundamental load. On the current generator plane, the optimum fundamental real impedance increased with drain bias, since the quiescent point on the I-V plane moved further away from the knee region and the slope of the dynamic load line became lower (more negative) to maintain high efficiency. At the same time, the nonlinear $C_{DS}$ variation with drain bias presented a reactive impedance shift at different bias points. This variation effect can also be seen on the $3^{rd}$ harmonic load trajectory, which presents an open circuit on the current generator plane at each bias point. The $2^{nd}$ harmonic load on the package plane did not change with drain bias as the $2^{nd}$ harmonic voltage was shorted at the current generator plane.

Fig. 3.3 shows the time-domain class-F voltage and current waveforms, as well as the dynamic load lines at the current generator plane when the class-F mode was optimised for each value of $V_{DS}$. The measured drain current at the device current generator plane swung below zero due to residual displacement current from the dynamic output capacitance ($C_{DS}$). This happened because the static de-embedding parameter used at each $V_{DS}$ was only appropriate for one particular DC drain voltage, and not the whole voltage swing. The achieved 'maximum available efficiency' and output power are plotted in Fig. 3.4, where the comparison with other scenarios is shown.

41
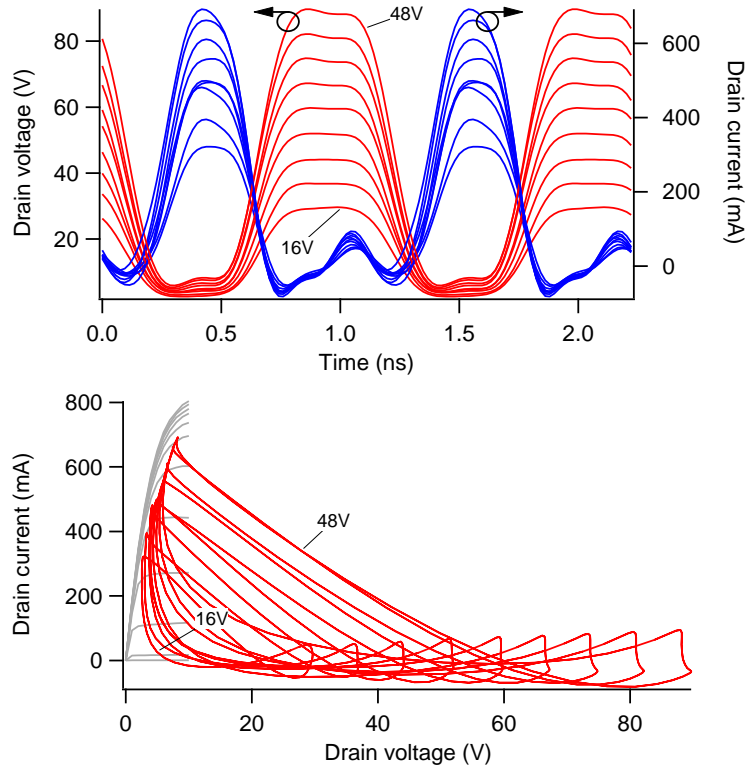
**Figure 3.3 – Voltage and current waveforms (top) and dynamic load lines (bottom) of the class-F mode in ET when optimised at each drain bias.**

### 3.3.2.2    *Class-F in ET Optimised at 48V and 28V Drain Voltages*

These two separate scenarios allow for the estimation of the drain efficiency degradation that can be expected in a real circuit where the load is fixed.  The optimal fundamental, $2^{nd}$ harmonic and $3^{rd}$ harmonic class-F load impedances were identified at one drain bias (48V or 28V), and then kept constant while the device was characterised for drain bias points from 16V to 48V in 4V steps.

Optimising the matching network at a peak drain bias of 48V produced a high peak efficiency of 74% but this rapidly dropped to 64% and 56% at 7.5dB and 9dB OBO, respectively.  This can present a significant disadvantage when used with signals with high peak to average power ratio (PAPR), where the PA only reaches peak power less than 1% of the time [7].
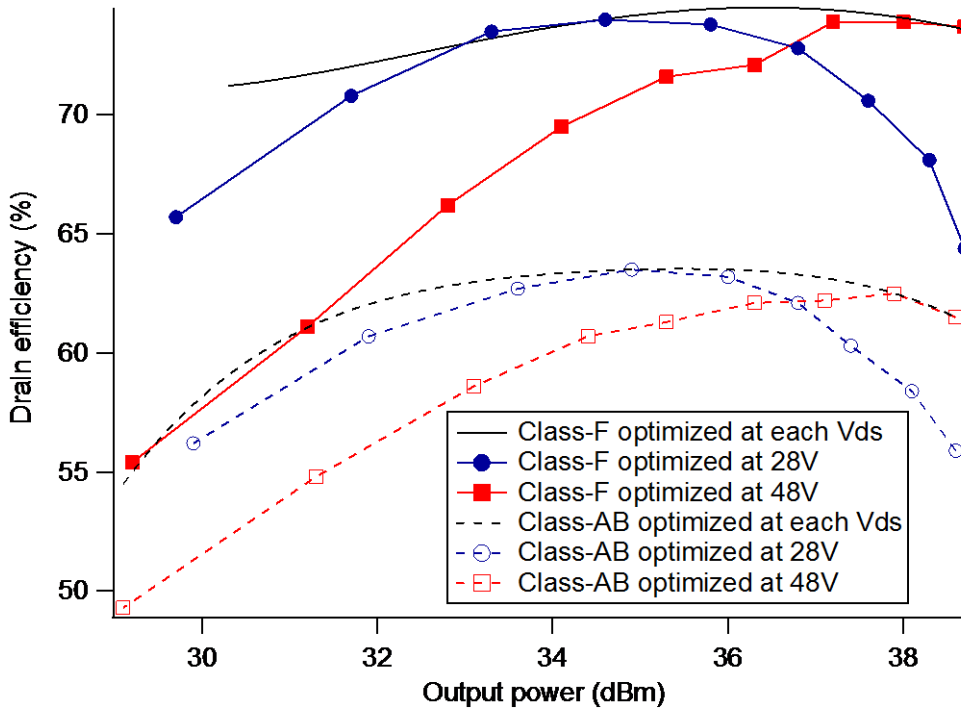
**Figure 3.4 - Efficiency comparison between the 3 scenarios for class-F and AB.**

Optimising the class-F PA at 28V shifted the peak efficiency to approximately 4.5dB below peak power and the efficiency only degraded by 6%-point at 9dB OBO instead of 18%-point as observed when optimised at 48V. Depending on the PAPR of the signal, the location of the peak efficiency can be adjusted by optimising the PA mode at the right drain bias. The optimisation at 28V drain bias was observed to offer a good compromise between the higher and lower output region, which suits the typical case where the PA spends most of its time several dBs below peak power. The impact on efficiency was observed to be less severe compared to when the device was optimised at 48V.

A similar trend was also observed for class-AB, which had a peak efficiency of approximately 63%. A drop of 10% and 4% from peak efficiency

was observed at 9dB OBO when it was optimised at 48V and 28V, respectively.

## 3.4    Analysing the Linearity vs. Efficiency Trade-Off for Different PA Modes in an ET Architecture

In an ET system, the selection of the drain bias supply for a particular input envelope voltage is accomplished through the definition of an envelope shaping function. This shaping function can be formulated for example to target optimum efficiency by keeping the device in the right compression level at all times where possible, or it can also be used to target linearity by maintaining a constant gain [7].

In this section, the linearity versus efficiency trade-off analysis was performed by examining the effects of these different shaping functions: the first was the *max-PAE* shaping function that targets maximum power added efficiency (PAE) and the second function referred to in this work as the *flat-gain* shaping function that targets a constant gain for linearity. The primary objective of this analysis is to quantify the efficiency trade-off when the *max-PAE* shaping function is used in a high-efficiency mode such as class-F. Waveform engineering was utilised in this analysis, revealing the intrinsic device behaviour under these different shaping functions in an ET environment.

The second objective is to relate the findings on the ET shaping functions for linearity improvement from this work with the previous baseband injection work in [1, 8-12], and being able to finally understand its impact on efficiency, which was not analysed before.

### 3.4.1      Methodology

#### 3.4.1.1    *Experimental setup and Engineering the PA Mode*

Using the same active load-pull system and the appropriate de-embedding, the device was configured to operate in a class-F mode at 900MHz with a fixed fundamental load of 117Ω, which was the optimum class-F fundamental load impedance when biased at 28V from the previous experiment. The drain bias range to emulate an ET setting was set from 16V to 48 in 4V steps. A similar experiment was repeated with the device set to operate in class-AB mode.

#### 3.4.1.2    *Characterising Gain at Different $V_{DS}$ to Extract Shaping Functions*

Once the desired mode was established at the selected fixed load, the device was characterised through a series of power sweeps performed at different $V_{DS}$ values. From these measurements, two different ET shaping functions were defined for each PA mode, relating input carrier envelope voltage magnitude ($|V_{IN}|$) to the drain voltage ($V_{DS}$); the first function tracks the peak efficiency for each $V_{DS}$ and the second tracks a constant gain. This step enables the efficiency versus linearity trade-off analysis for the two PA modes.

#### 3.4.1.3    *Applying Shaping Functions for Performance Comparison*

When applying the $V_{DS}$ versus $|V_{IN}|$ relationship defined by the above shaping functions, it is possible to relate how the different functions affect the PA performance when used in an ET environment, since the voltage and current information is available at the device plane. The parameters of interest are PAE, the device dynamic transconductance (AM-to-AM distortion), and AM-to-PM distortion as a function of input envelope voltage magnitude.

### 3.4.2        Experimental Results

Fig. 3.5 shows the series of gain curves at different $V_{DS}$ for class-F and class-AB as a function of output power together with the locations where the maximum PAE sits within those curves.  Due to the power sweep resolution used, the maximum PAE trajectory was not smooth.
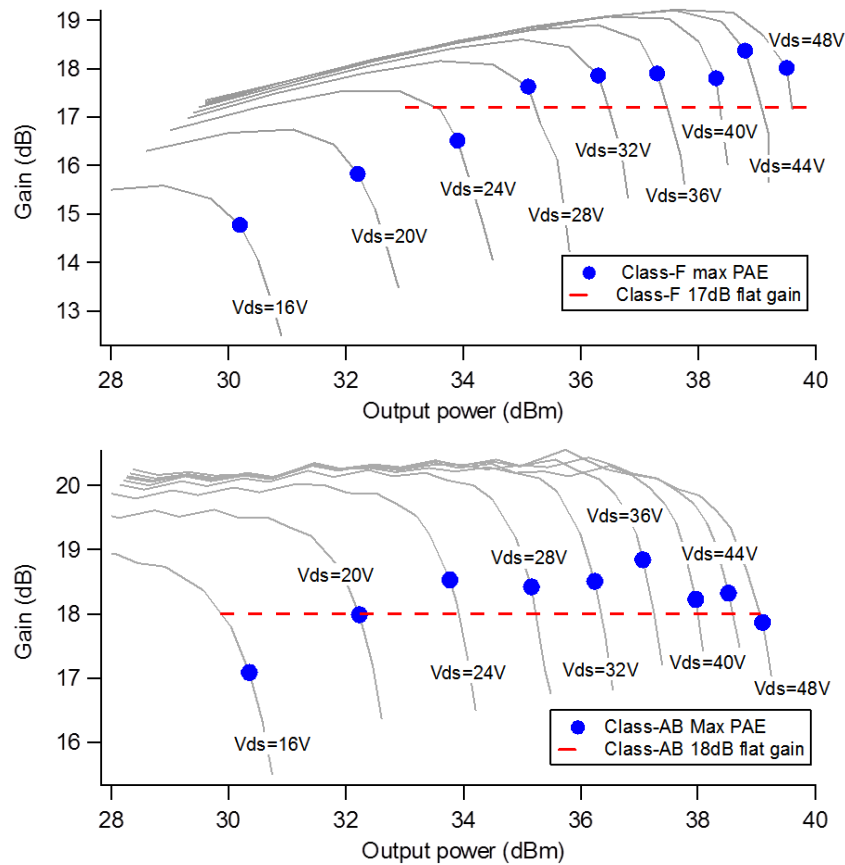


**Figure 3.5 – Measured gain characteristics of class-F (top) and class-AB (bottom). The blue dots indicate the location of maximum PAE and the dotted red line shows the desired constant gain.**

As well as establishing a $V_{DS}$-$|V_{IN}|$ relationship that delivers maximum PAE for each $V_{DS}$, from these gain curves it is also possible to select a constant gain scenario from each $V_{DS}$ state, thus defining a shaping function that will deliver minimum AM-AM distortion when ET is applied.  For example for class-AB, a constant gain of 18dB was chosen which was obtainable for

9dB of the output power range. For class-F, due to the gain expansion-compression characteristic, a constant gain of 17dB was selected, which was obtainable for 6dB of the dynamic range from peak power. The resulting '*max-PAE*' and '*flat-gain*' shaping functions that described the relationship between the required drain supply voltage and the magnitude of the input envelope voltage ($|V_{IN}|$) for class-F and class-AB modes are shown in Fig. 3.6.
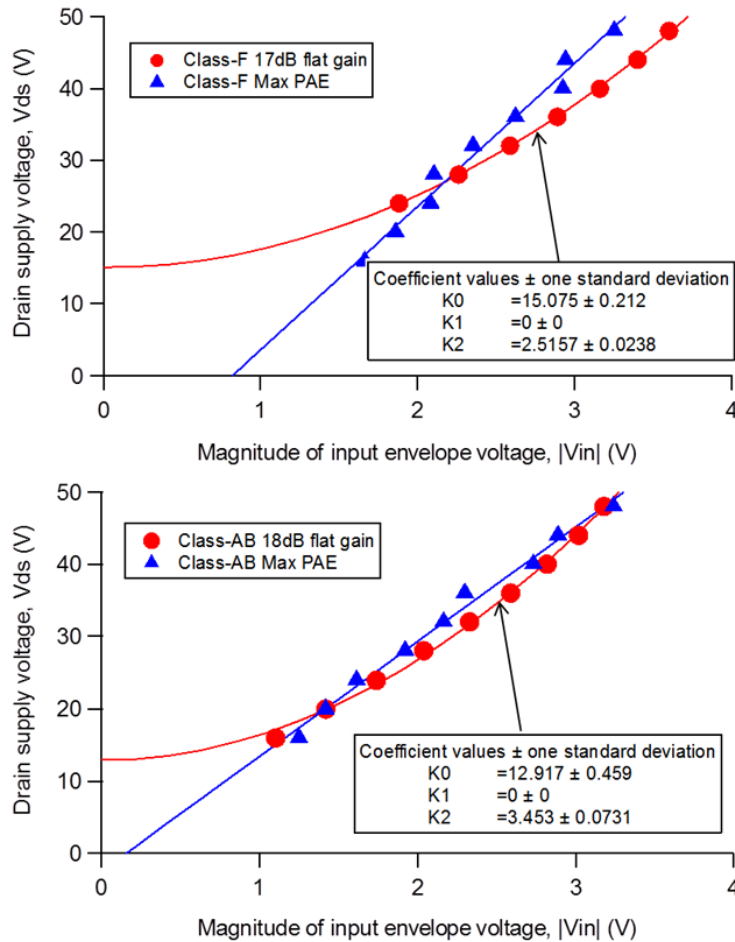


**Figure 3.6 – Extracted shaping functions for efficiency (blue) and linearity (red) for class-F (top) and class-AB (bottom).**

For both PA modes, the '*flat-gain*' shaping function has a quadratic relationship with the input envelope voltage, consisting of second-order polynomial terms. While this behaviour was extracted from a set of CW power

sweeps this result is consistent with experimental dynamic observations with complex modulation presented in the baseband injection work in [1] where the baseband signal consisting of even order terms, when injected at the drain minimized AM-AM distortion. This was due to the mixing process between the input RF signal and the injected baseband signal, as the device was constantly driven into compression throughout the ET range. The '*max-PAE*' scenario on the other hand appeared to require a linear relationship. In practice a minimum $V_{DS}$ is set above the knee voltage in the shaping function to avoid gain collapse at low drive levels [13].

Fig. 3.7 shows the efficiency comparison between '*flat-gain*' and '*max-PAE*' shaping functions, for both modes of amplifier. Since the class-F loads were optimised when the device was biased at 28V which represented average power, the resulting overall ET efficiency peaked somewhat in the middle of the output power range, as expected. Remarkably, for class-F, it can be seen that the efficiency degraded only by approximately 2% when the '*flat-gain*' shaping function was used in place of the '*max-PAE*' function.
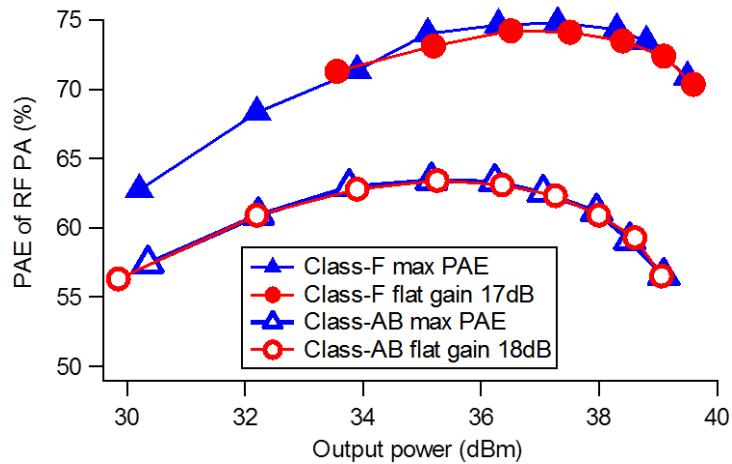


**Figure 3.7 – Measured PAE comparison between the 2 shaping functions for class-F and class-AB.**

However, the available output power range to obtain this linear performance was limited to approximately 6dB. A lower gain selection is required if the ET output power range is to be extended further, as indicated by Fig. 3.5. For the class-AB case, there was virtually no PAE degradation when the '*flat-gain*' shaping function was used, due to its different gain characteristic.
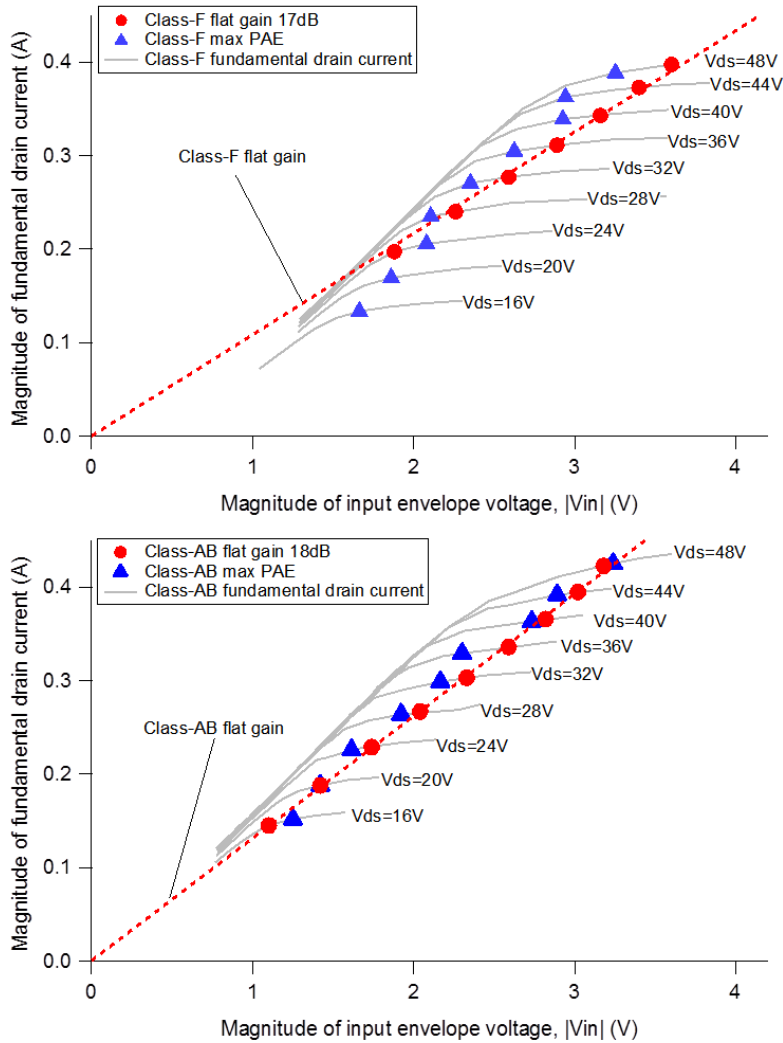


**Figure 3.8 - Measured transconductance of class-F (top) and class-AB showing a linear relationship for '*flat-gain*' shaping function (red)**

It is useful to compare the location of the shaping functions on the measured device dynamic transconductance – the relationship between the fundamental drain current magnitude and the input voltage magnitude, and this

49

is plotted in Fig. 3.8. The '*flat-gain*' shaping function yields a linear relationship through the origin, between input voltage and output current throughout the ET range, with any deviations being due to the limited resolution of the power sweep. This characteristic suggests that there would be minimal distortion terms generated at the output when the device is excited with a complex and wideband modulation signal such as LTE. The result also suggests that the formulated shaping function used for achieving a linear performance is attributed to the device characteristics and should be independent of the envelope shape or modulation bandwidth, as observed in [11, 12].

It is noted that the AM-to-PM distortion exhibited by the '*flat-gain*' shaping function was comparable to that of the '*max-PAE*' shaping function for the same dynamic range, as shown in Fig. 3.9. The observed AM-PM performance was the characteristic of the device itself and was not affected by the selection of shaping functions, similar to the observations made in [10].
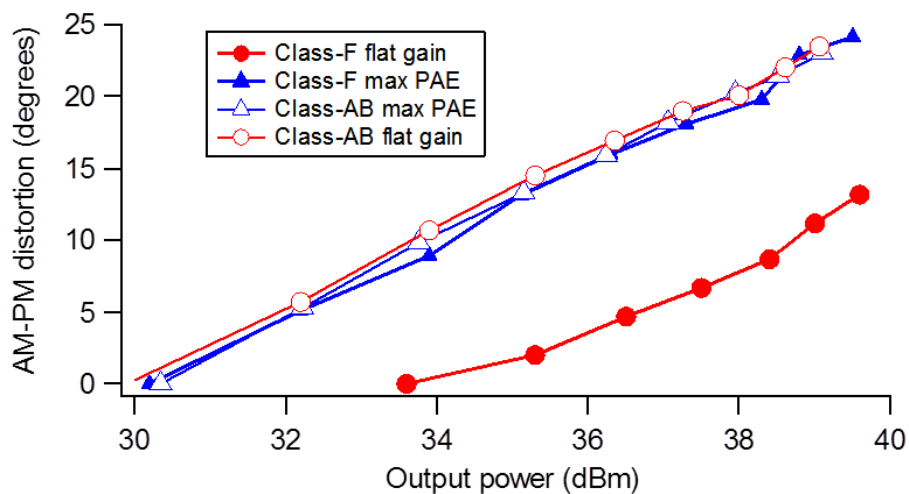


**Figure 3.9 – Measured AM-PM distortion comparison for class-F and class-AB for the two shaping functions.**

### 3.4.3    Discussions

The effects of using different shaping functions for maximum PAE and flat gain have been shown for both class-AB and class-F modes, operating in an ET environment. Experimental results indicate that there was only a small efficiency trade-off when the *flat-gain* shaping function relating drain supply voltage signal to the input voltage magnitude was used within the compression region of the LDMOS device. It is noted that while the absolute PAE number obtained from the *max-PAE* shaping function in Fig. 3.7 was determined by the fixed load presented to the device, the efficiency trade-off figure (the difference between the red and blue curves in Fig. 3.7) would vary with the selection of the constant gain value used in defining the *flat-gain* shaping function.

The extracted *flat-gain* shaping function consisted of only even order terms and was shown to be effective in linearising the device transconductance in comparison to the maximum PAE case. These results are consistent with the experimental work carried out in [1, 10-12], indicating a possibility of using ET drain bias as a linearising baseband signal without significantly impacting efficiency.

In using the *flat-gain* shaping function for class-F, the output power range where this takes effect is determined by the constant gain value selected, as shown in Fig. 3.5. The selection of the gain value therefore needs to consider the signal PAPR. The other ET parameter that is dependent on this constant gain value is the minimum drain bias in the case of the class-F mode.

Also, if the signal PAPR is known, the selection of the constant gain value for the *flat-gain* shaping function can be made to coincide with the gain value which has the maximum PAE at average power. This will increase the likelihood of attaining the highest possible average efficiency performance under the constraint of the using a shaping function that targets linearity.

The absolute maximum output power is determined by the fundamental load impedance selection. This output power requirement may well be a design constraint that will limit overall efficiency performance. It is noted that the optimum load for output power at maximum drain bias point is different from the optimum load for efficiency for the same drain bias. However in ET the optimum efficiency load is targeted at average power which sits at a lower drain bias. This reduces the trade-off between maximum output power and efficiency at the ET system level.

## 3.5 Relating the ET Linearity Improvement Results with Previous Baseband Injection Work

Before concluding this chapter, the experimental results of the *flat-gain* shaping function for linearity improvement are now compared to the baseband injection method to understand their correlations, the effectiveness of utilising ET's modulated drain bias as a baseband linearisation signal, and the effect of baseband injection on efficiency, which was not previously analysed.

The previous baseband injection works in [1, 10-12] formulated the baseband signal in the envelope domain and applied it to the drain of a device. The device operated in a class-AB mode with a fixed drain bias under modulated excitations using discrete tones. The output of the device package

plane was terminated into 50Ω and was not presented with an optimum load for efficiency. With the device driven 1.5dB into compression, the baseband formulation algorithm iteratively calculates the 2$^{nd}$ and 4$^{th}$ order coefficients of the baseband signal to linearise the device transconductance and suppressing the IM3 and IM5 products. The maximum current ($I_{MAX}$) and voltage ($V_{MAX}$) were kept constant before and after the baseband signal injection because of the multiple solutions available for the coefficients.

This section tries to replicate that setup in a simulation environment taking advantage of the excellent device model available in this work that has been proven to show a good correlation with load-pull results. For this simulation, a simple second order baseband signal is injected at the drain while keeping the maximum current ($I_{MAX}$) and voltage ($V_{MAX}$) constant. The ability to present optimum loads and calculate efficiency is now added in simulation to evaluate the impact of baseband injection on efficiency. The transfer function of drain current versus input voltage is also extracted for comparison with the ET shaping function.
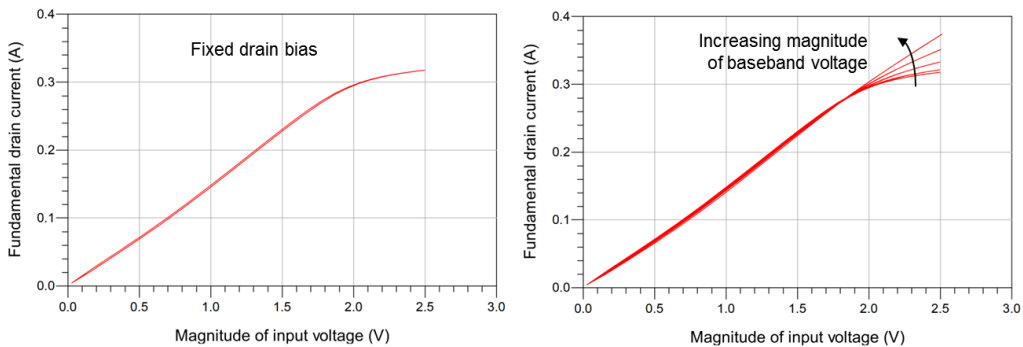
### 3.5.1    Simulation Setup: Baseband Injection Approach for PA Linearisation

For this analysis, an Envelope simulation in ADS was used and a two-tone signal was used for the input as it would enable the baseband signal to be formulated using a simple sine wave with certain amplitude and phase combination. Fig. 3.10 shows the schematic of the setup.
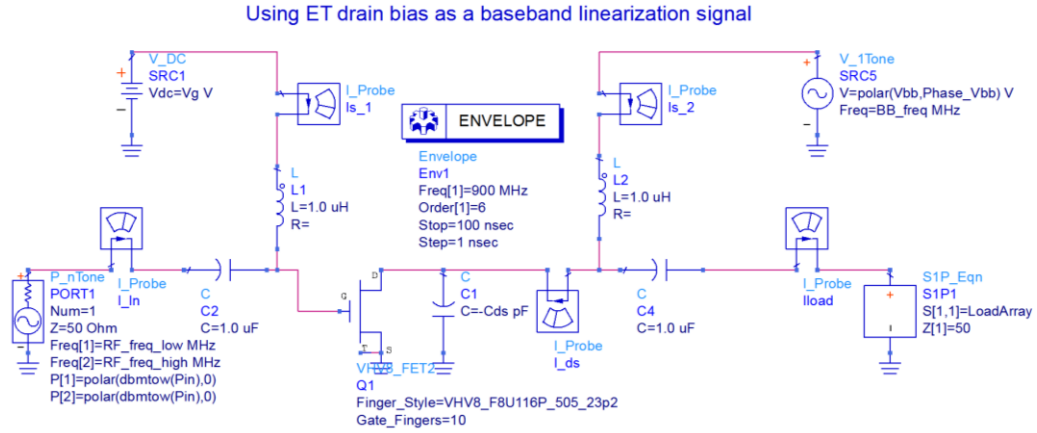
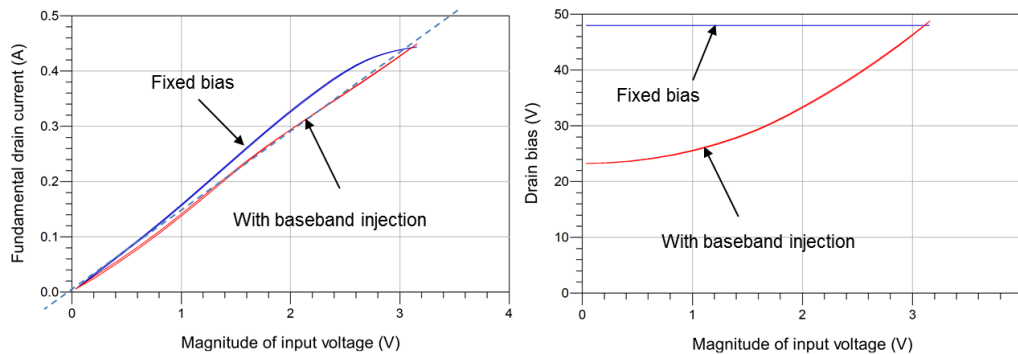**Figure 3.10 - Baseband injection simulation setup in ADS**

The two-tone signal used in this simulation had a signal separation of 20MHz and was applied at the input to drive the device into compression in a class-AB mode and then class-F, both with the proper fundamental and harmonic terminations. For each PA mode, the device transconductance was observed, first with a fixed drain bias at the drain and second with a lower DC supply combined with a sine wave of a defined magnitude and phase. The magnitude and phase of this sine wave and DC combination were adjusted so that it would produce a modulated drain supply that will linearise the device transconductance, as shown in Fig. 3.11.



**Figure 3.11 – Simulating the linearising effect of baseband injection.**

### 3.5.2        Baseband Injection Simulation Results: Class-AB

Fig. 3.12 shows simulation results before and after applying the baseband injection on a class-AB mode PA while keeping $I_{MAX}$ and $V_{MAX}$ constant, as well as the resulting $V_{DS}$-$|V_{IN}|$ relationship.    The resulting transconductance was more linear after injecting the baseband although some weakly nonlinear effect was still visible since only a second order baseband signal was applied.   The injected baseband transfer function is shown on the right plot in Fig. 3.12, where it resembled the ET shaping function that targets a constant gain from Fig. 3.6.



**Figure 3.12 - The comparison before (blue) and after (red) baseband injection on class-AB simulated transconductance (left) and drain bias (right).**

The simulated efficiency and intermodulation products are shown in Table 3.1.  Although in this case the maximum PAE was the same as with fixed bias, the average PAE did improve with the baseband injection, in this example by almost 6%.  The IM3 products in this example were suppressed by 7dB relative to fixed bias to be around -30dBc and this number can be further improved with higher order coefficients.  As a point of reference, the measured baseband injection work in [12] achieved -40dBc on a GaN device with a 4th order baseband signal coefficient for a 3-tone 20MHz signal bandwidth, and it was noted in [10] that the method was more effective on a GaN device

compared to LDMOS. The IM5 products were reduced by 17dB to -50dBc in this simulation.

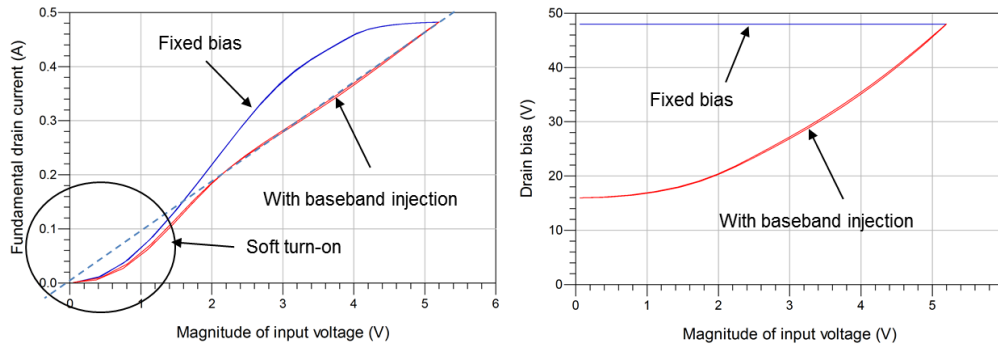| Class-AB | Before baseband injection | After baseband injection | Delta |
|---|---|---|---|
| Maximum PAE (%) | 65.6 | 65.6 | 0.0 |
| Average PAE (%) | 47.7 | 53.6 | +5.9 |
| IM3 L/H (dBc) | -22.9/-22.9 | -31.3 / -30.2 | -8.4 / -7.3 |
| IM5 L/H (dBc) | -33.6/-33.6 | -51.8 / -50.1 | -18.2 / -16.5 |

**Table 3.1 - The simulated effect of baseband injection on class-AB PA**

### 3.5.3    Baseband Injection Simulation Results: Class-F

The same experiment was repeated for class-F and the results are shown in Fig. 3.13. Once again, modulating the drain shows similar characteristics to the ET *flat-gain* shaping function. Applying baseband injection for class-F linearised the top end of the transconductance curve in the compression region but was not able to linearise the soft turn-on region due to the device being biased at pinch-off. This is the limitation of the class-F mode which sits on a class-B gate bias. As a result, the IM3 products although improved relative to fixed bias, did not show the improvement seen on a class-AB mode as shown in Table 3.2. The suppressed IM3 product was -23dBc which indicated a 3.5dB improvement compared to fixed bias in this example. This number can potentially be further improved with higher-order baseband coefficients.

However in terms of efficiency, the class-F mode PA showed a much higher improvement with baseband injection compared to class-AB. The 68% average PAE with baseband injection was a 10%-point improvement

compared to fixed bias in this example, and also 14%-point higher than class-AB with baseband injection.



**Figure 3.13 - The comparison before (blue) and after (red) baseband injection on class-F simulated transconductance and drain bias.**

| Class-F | Before baseband injection | After baseband injection | Delta |
|---|---|---|---|
| Maximum PAE (%) | 77.6 | 81.4 | +3.8 |
| Average PAE (%) | 57.8 | 68.0 | +10.2 |
| IM3 L/H (dBc) | -19.6 / -19.4 | -23.6 / -22.9 | -4.0 / -3.5 |
| IM5 L/H (dBc) | -28.5 / -29.5 | -45.9 / -44.1 | -17.4 / -14.6 |

**Table 3.2 - The simulated effect of baseband injection on class-F PA**

### 3.5.4    Discussion on Baseband Injection Simulation Results

From the baseband injection simulation above it is observed that the baseband transfer function has similar characteristics as the ET shaping function that targets a constant gain for linearity.  This is the common ground for these 2 approaches towards improving the linearity: the baseband injection method formulates the baseband coefficients in the envelope domain to achieve a linear transconductance, while the ET method searches for a constant gain condition in the RF domain and extracts a shaping function which also produces a linear transconductance plot.

Another key observation is that both approaches improve the average efficiency of the class-AB and class-F PA compared to fixed drain bias while achieving a relatively linear performance. This highlights an opportunity of using the ET architecture to inject linearising baseband signals at the drain supply to offer some degree of 'linearisability' advantage without trading-off significant efficiency performance.

While class-F exhibits a much higher efficiency compared to class-AB, its linearity improvement is relatively smaller compared to that of class-AB due to the soft turn-on at low input voltage as a result of biasing the gate at pinch-off. Both the ET *flat-gain* shaping function and baseband injection were only able linearise the top part of the transconductance curve that is nonlinear due to compression, but not able to correct for the nonlinearities at the turn-on region. This presents limitation for a class-F linearity performance when implemented with baseband injection, and more importantly with a linearising ET shaping function. This limitation will be discussed in Chapter 5 where a class-F PA is designed, fabricated, and tested in an ET system.

## 3.6     Conclusions

Using waveform engineering, the behaviour of a class-F mode PA in a variable drain setting has been shown in terms of efficiency performance and optimum load trajectory. It has been observed that the device's $C_{DS}$ value affects the efficiency performance of class-F in an ET environment by as much as 18%-point at 9dB OBO as it shifts the optimum fundamental and harmonic loads at different drain bias settings. To reduce the efficiency degradation, the class-F PA needs to be optimised at the average voltage, depending on the

signal PAPR.  However this may prove to be a challenge in terms of producing the required output power.  This challenge will be analysed in the next chapter, in formulating an optimum design flow for ET applications.

It was also concluded that the device model used in this work has a good correlation with the actual device in terms of measurements at the current generator plane.  This provides a significant advantage in the next steps of research presented in the following chapters where experiments are carried out in simulations with high confidence and load-pull measurements are used primarily as a validation step.

This chapter also described how different shaping functions affect the linearity and efficiency performance of class-AB and class-F mode power amplifiers.  It was shown that there is minimal trade-off in efficiency when the shaping function used targets a constant gain, or linear performance, both for class-AB and class-F as long as the PA is in compression.

It was observed that an ET shaping function that targets a constant gain performance has a quadratic relationship between the supplied drain voltage and the magnitude of the input envelope voltage, while a shaping function that targets maximum efficiency has a linear relationship between these parameters.  This observation agrees with previous work in [1, 10-12] that an even-order baseband signal can be formulated to linearise and suppress IM3 and IM5 signals of a PA operating in a class-AB bias.  However it is suspected that the linearisation achieved from the shaping function is limited in class-F, due to the soft turn-on region at the lower part of the dynamic range.

In the next chapter a systematic method to optimise the RF PA design

for ET is formulated using waveform engineering and a class-F PA design and

fabrication is presented.

## 3.7     References

[1]     F. L. Ogboi, P. J. Tasker, M. Akmal, J. Lees, J. Benedikt, S. Bensmida*, et al.*, "A LSNA configured to perform baseband engineering for device linearity investigations under modulated excitations," in *Microwave Conference (EuMC), 2013 European*, 2013, pp. 684-687.

[2]     K. Bumman, M. Junghwan, and K. Ildu, "Efficiently Amplified," *Microwave Magazine, IEEE,* vol. 11, pp. 87-100, 2010.

[3]     P. J. Tasker, "Practical waveform engineering," *Microwave Magazine, IEEE,* vol. 10, pp. 65-76, 2009.

[4]     P. J. Tasker and J. Benedikt, "Waveform Inspired Models and the Harmonic Balance Emulator," *Microwave Magazine, IEEE,* vol. 12, pp. 38-54, 2011.

[5]     K. Joon Hyung, J. Gweon Do, O. Jung Hoon, K. Young Hoon, L. Kwang Chun, J. Jae Ho*, et al.*, "High-Efficiency Envelope-Tracking Transmitter With Optimized Class-F-1 Amplifier and 2-bit Envelope Amplifier for 3G LTE Base Station," *Microwave Theory and Techniques, IEEE Transactions on,* vol. 59, pp. 1610-1621, 2011.

[6]     M. S. Alavi, F. van Rijs, M. Marchetti, M. Squillante, T. Zhang, S. J. Theeuwen*, et al.*, "Efficient LDMOS device operation for envelope tracking amplifiers through second harmonic manipulation," in *Microwave Symposium Digest (MTT), 2011 IEEE MTT-S International*, 2011, pp. 1-1.

[7]     Z. Wang, *Envelope Tracking Power Amplifiers for Wireless Communications*: Artech House, 2014.

[8]     M. Akmal, V. Carrubba, J. Lees, S. Bensmida, J. Benedikt, K. Morris*, et al.*, "Linearity enhancement of GaN HEMTs under complex modulated excitation by optimizing the baseband impedance environment," in *Microwave Symposium Digest (MTT), 2011 IEEE MTT-S International*, 2011, pp. 1-4.

[9]     J. Lees, M. Akmal, S. Bensmida, S. Woodington, S. Cripps, J. Benedikt*, et al.*, "Waveform engineering applied to linear-efficient PA design," in *Wireless and Microwave Technology Conference (WAMICON), 2010 IEEE 11th Annual*, 2010, pp. 1-5.

[10]    F. L. Ogboi, P. Tasker, Z. Mohkti, J. Lees, J. Benedikt, S. Bensmida*, et al.*, "Sensitivity of AM/AM linearizer to AM/PM distortion in devices," in *Microwave Measurement Conference (ARFTG), 2014 83rd ARFTG*, 2014, pp. 1-4.

[11]    F. L. Ogboi, P. J. Tasker, M. Akmal, J. Lees, J. Benedikt, S. Bensmida*, et al.*, "Investigation of Various Envelope Complexity Linearity under Modulated Stimulus Using a New Envelope Formulation Approach," in *Compound Semiconductor Integrated Circuit Symposium (CSICs), 2014 IEEE*, 2014, pp. 1-4.

[12]    F. L. Ogboi, P. J. Tasker, M. Akmal, J. Lees, J. Benedikt, S. Bensmida*, et al.*, "High bandwidth investigations of a baseband linearization approach formulated in the envelope domain under modulated stimulus," in *Microwave Conference (EuMC), 2014 44th European*, 2014, pp. 1305-1308.

[13]    K. Bumman, K. Jungjoon, K. Dongsu, S. Junghwan, C. Yunsung, K. Jooseung*, et al.*, "Push the Envelope: Design Concepts for Envelope-Tracking Power Amplifiers," *Microwave Magazine, IEEE,* vol. 14, pp. 68-81, 2013.

# Chapter 4

# Using Waveform Engineering to Optimise PA Design for Envelope Tracking Applications

## 4.1     Introduction

In the previous chapter, the waveform engineering approach was used to understand the behaviour of a class-F PA in a variable drain voltage setting. The effect of optimising the load terminations at different bias points has been demonstrated and the linearity-efficiency trade-off of class-F and class-AB PA's was described for different shaping functions. The efficiency of the RF PA in an ET system determines the highest achievable efficiency of the transmitter [1].  Additionally, ET has the potential to linearise highly efficient but nonlinear RF PA's, with carefully designed shaping functions [2].

The objective of this chapter is to formulate an optimum PA design methodology for ET applications using waveform engineering, which takes into account efficiency, linearity, output power, and signal PAPR aspects through suitable load conditions and shaping function definitions.  Subsequently, this method is then used to design a 10W RF PA using an LDMOS device from Freescale for an ET application towards the end of this chapter.

**4.1.1       Design Goals**

As part of the Opera Net 2 project [3], the optimisation of the base station hardware was to be achieved through the use of a class-F PA in an ET architecture.  The design goals are shown in Table 4.1.

| | |
|---|---|
| Peak output power | >39 dBm |
| Average efficiency | >60% (ET modulator + PA) |
| Signal PAPR | 7.5dB |
| Bandwidth | 40MHz |
| Frequency range | 880MHz to 920MHz |

**Table 4.1 - Design goals**

**4.2       Formulating the Design Flow of a Class-F PA for an ET Application**

① Determine impedance that balances max power at max $V_{DS}$ and ET system PAE at output back-off

② Identify max-PAE points for each $V_{DS}$ from gain curves

③ Identify '*average*' drain bias ($V_{D\_AVG}$) whose max-PAE sits at average power. Assign a constant gain ($G_{OPT}$) that coincides with this point and use it for all $V_{DS}$

④ Determine lowest $V_{DS}$ that can still meet the gain requirement of $G_{OPT}$

⑤ Extract the shaping function ($V_{DS}$-$V_{IN}$) fixing the gain of each $V_{DS}$ to $G_{OPT}$

⑥ Verify the linear transconductance curve

**Figure 4.1 - Formulated design flow**

With the observations from Chapter 3, a systematic approach can be formulated in designing an RF PA to be used in an ET architecture.  The design flow considers the factors that will influence the PA performance in terms of efficiency and linearity with the constraint on output power and signal

PAPR. This is to be achieved through the design of an optimised output matching circuit based on an assumed signal PAPR and through the formulation of a shaping function that targets a constant gain performance. Fig. 4.1 shows the proposed design flow of the PA, achieved through waveform engineering.

This section describes the design flow together with measurement results of a class-F PA to be used in an ET system. The useable drain bias range for ET is from 16V to 48V to avoid the knee and breakdown regions.

### 4.2.1     Finding the Optimum Fundamental Load

The first step is to find the optimum fundamental load for the output matching circuit. This selection is a critical step as it determines the maximum achievable efficiency and maximum output power, as described in Chapter 3. Since this is fixed throughout the operation of the PA and the device $C_{DS}$ will shift the optimum fundamental load at different drain bias, a compromise between maximum output power at 48V bias, and efficiency with ET at average power is needed.

The optimum fundamental impedance ($R_{OPT}$) is determined by performing a load sweep at the maximum drain bias of 48V. To aid the process, an ET simulation template in ADS is developed to run a 3-dimension sweep: fundamental real load, drain bias, and input power. The 3dB-compression output power at peak $V_{DS}$ of 48V and the *ET efficiency* at 7.5dB OBO are recorded. The *ET efficiency* is defined as the trajectory of maximum PAE curves of different drain bias within the ET drain supply range of 16V to 48V.

Fig. 4.2 shows the outcome of this step, both from simulation and from measurement. The simulated ET system PAE at 7.5dB OBO is also included in this plot, even though this is not performed in measurement. This is because it is not known, at this point, which drain voltage will have the highest efficiency at 7.5dB OBO therefore performing an exhaustive load-pull is not practical. However looking at the high correlation between simulation and the measurement data trend at 48V bias, the simulation information about the ET efficiency at OBO presents a good prediction of the actual device behaviour.
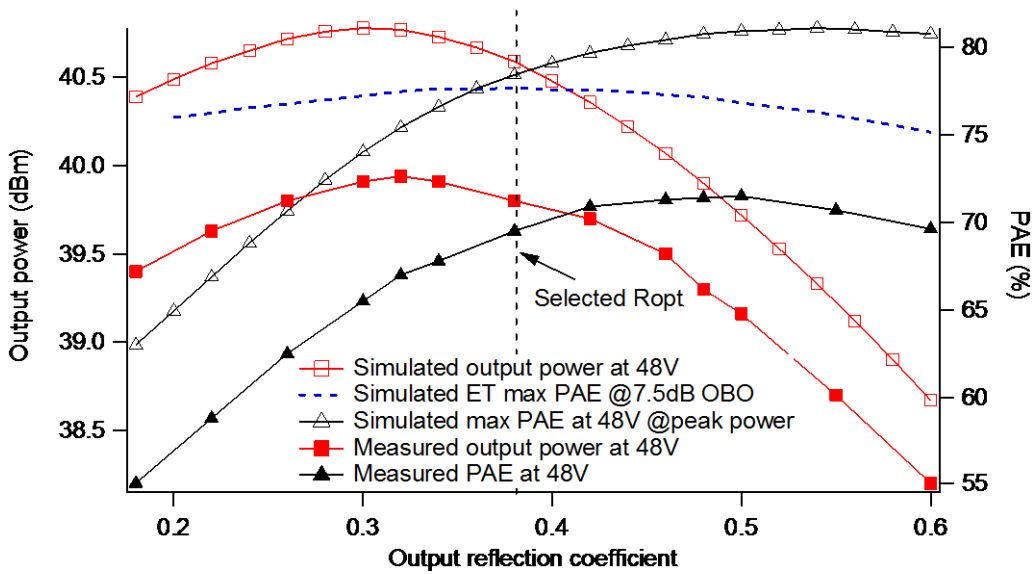


**Figure 4.2 – Simulated output power at 48V bias and the corresponding PAE at 7.5dB OBO with ET applied**

As expected the optimum load for peak power at 48V drain bias is different from the optimum load for efficiency at average power at 7.5dB OBO. For this PA design, the chosen output reflection coefficient is 0.34 which corresponds to an optimum load of 101.5Ω as it provides a good compromise between peak power and efficiency at average power.

## 4.2.2      Identifying Maximum-PAE locations, Assigning Constant Gain (G$_{OPT}$), and Minimum Drain Bias (V$_{D\_MIN}$) from Gain Curves

The next step is to obtain the device gain characteristics when presented with the selected fundamental load at the current generator plane, for different drain bias points.  A family of gain curves is obtained from power sweeps at different drain bias points with the device operating in a class-F mode, as shown in Fig. 4.3.

For each drain bias point, the point of maximum PAE is identified.  The drain bias point that has its maximum PAE closest to the average power in this case is 20V, and the intersecting gain of 15.4dB is chosen as the target constant gain value (G$_{OPT}$) for each V$_{DS}$.  The lowest drain bias (V$_{D\_MIN}$) that can still provide this target gain value is 16V.  This value is set as the minimum for the ET drain supply range.

The measured PAE, also shown in Fig. 4.3, indicates a 3% worst-case degradation in efficiency when the ET shaping function for constant gain is used, while the output power range where this constant gain can be achieved is approximately 10dB.  This small trade-off in efficiency agrees with the measured results from Fig. 3.7 in Chapter 3, even though a different load (117Ω) is used.  This indicates, potentially, that ET can provide both efficiency and linearity improvements simultaneously.

The maximum output power was measured to be 39.6dBm at 48V drain bias.  With a PAPR of 7.5dB, the average power is estimated to be 32dBm. The measured PAE at average power is 67% when the drain is biased at 20V.

Since the load was selected to balance output power and PAE, the efficiency did not peak at the average power; instead it peaked at around 3dB OBO.
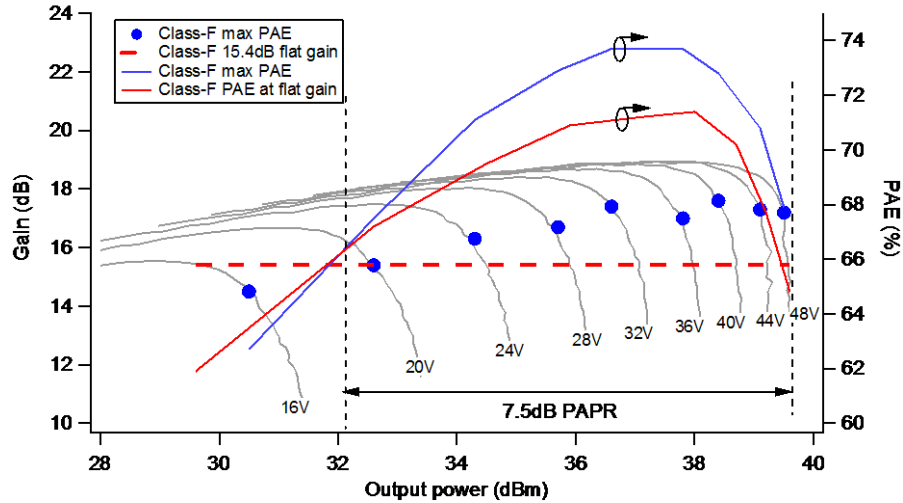


**Figure 4.3 - Measured gain curves with locations of maximum PAE (blue dots) and flat 15.4dB gain (red dash lines), and the corresponding measured PAE.**

### 4.2.3      Extracting the Shaping Function

From the previous step, the relationship between the output power, gain, delivered input power, drain supply voltage, input voltage, and output current that will yield a flat gain or maximum PAE performance can be determined from the waveform engineering process.  It is therefore possible to generate the shaping function that would produce a flat gain performance when ET is applied.  Fig. 4.4 shows the extracted ET shaping function from the previous step, which describes the relationship between the input voltage and the drain supply voltage.  The first shaping function (blue) targets maximum efficiency throughout the ET operating range while the second one (red) targets a flat gain performance and therefore linearity.  The quadratic feature of the *flat-gain* shaping function agrees with the observation from Chapter 3.

The input voltage range is bigger for the flat gain shaping function because the PA is highly compressed at 48V during peak power in order to go down to the same gain level as when it is biased at 20V. The lowest input voltage that will enable this flat gain performance is shown in the Fig. 4.4 as $|V_{IN}|$ minimum.
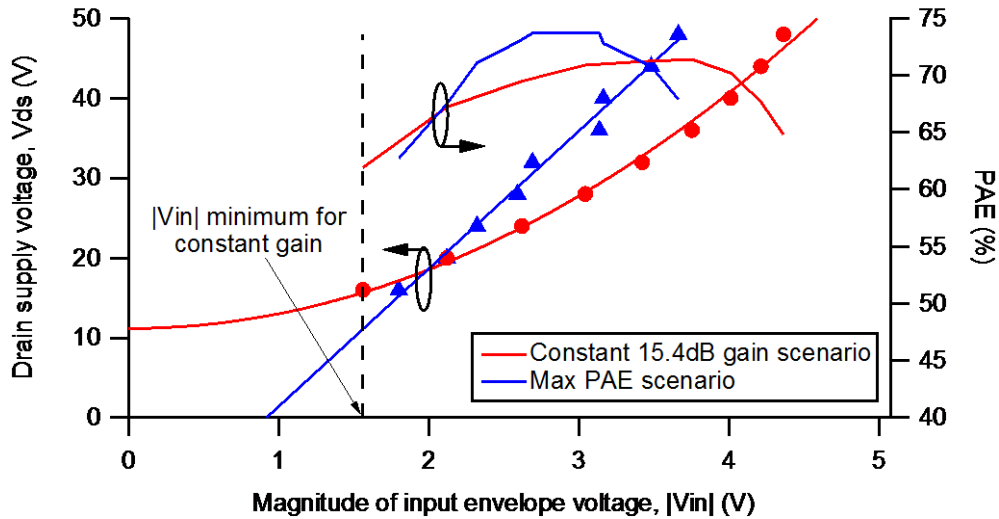


**Figure 4.4 - Extracted shaping function for maximum PAE (blue) and constant 15.4dB gain (red) from measurement, together with the corresponding PAE's.**

### 4.2.4     Verifying the Transconductance Curve

Finally, the linearity performance can be verified by the transconductance plot, which describes the relationship between output current and input voltage. Fig. 4.5 shows the resulting transconductance plot for the *flat-gain* and *max-PAE* shaping functions. As expected the *flat-gain* shaping function yields a linear relationship between the input voltage and the output fundamental current of the device. However this linear relationship has a limited range – when the input voltage is above the minimum $|V_{IN}|$. For lower input voltage magnitudes, the trace will follow the transconductance curve of the lowest $V_{DS}$.
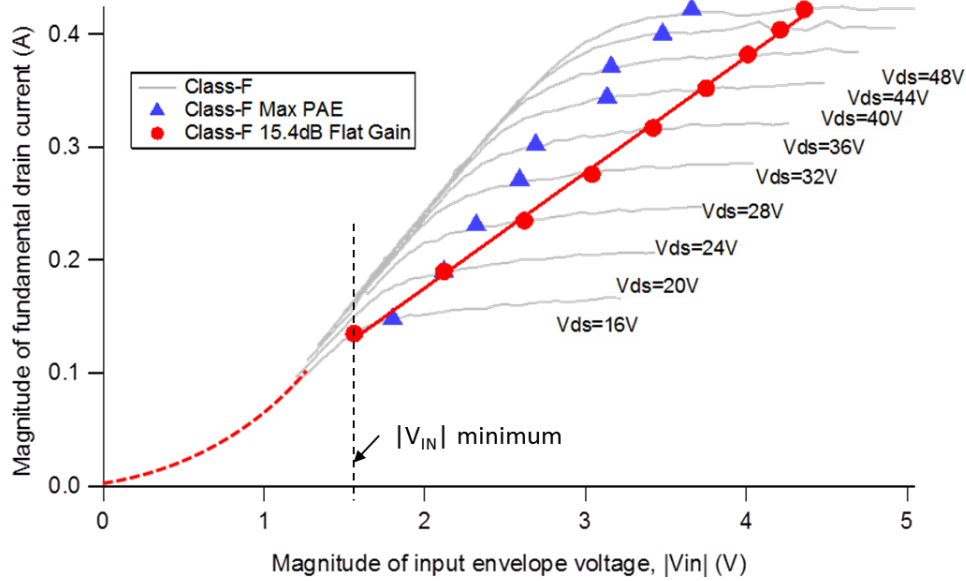
**Figure 4.5 - Verifying the simulated linear performance from the transconductance plot.**

## 4.3      Designing the PA

The design of the class-F PA needs to consider how it would be integrated into a larger ET system, especially in terms of dimension and drain bias connections.  The ET system that was used is a customized *Arelis*[1] ET system with a proprietary ET modulator.  The class-F PA was connected through an adapter board and the drain bias was connected using a through-hole pin that passed through the class-F PA, as shown in Fig. 4.6.  For this design, only one drain bias pin was needed that would connect the ET modulator signal to the drain of the device.  Therefore a through-hole path was needed in the output matching circuit design.

The PA was designed on an aluminium-backed RT/duroid 5880 substrate from Rogers Corporation.  It has a dielectric thickness of 20 mil (508 µm) with a relative permittivity of 2.2 and loss tangent of 0.0004 [4].  The copper

[1] Formerly Thomson Broadcast, founder member of the Opera Net consortium.

conductor thickness is 17 μm, and a 50Ω transmission line has a width of 1.54 mm.  The 250 mil (6.35 mm) aluminium provides the ground as well as acting as a heat sink.
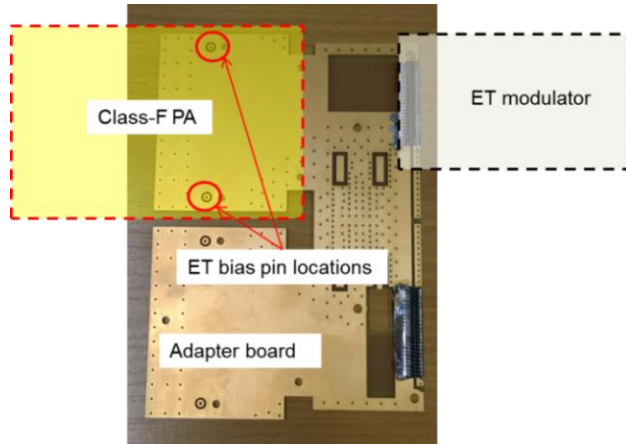


**Figure 4.6 - Hardware connections between the PA and the ET modulator.**

### 4.3.1     The Input Match
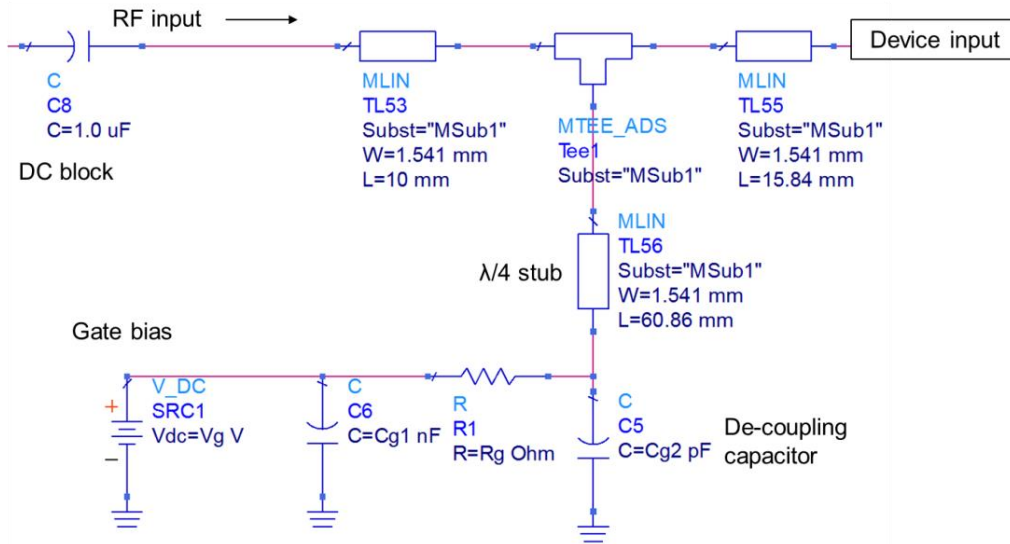


**Figure 4.7 - Input matching circuit**

From the load-pull data, the gain of the device without an input matching circuit was approximately 15dB.  For this proof of concept PA, the input matching network was not the main focus and therefore an extensive

analysis of the design of the input matching was not performed.  The PA input was intended to have the same transmission line length as the test fixture used during load-pull so that the input drive level would be similar.  Therefore, for this PA, only the gate bias insertion circuit was included using a simple short-circuited quarter wavelength stub with a de-coupling capacitor, as shown in Fig. 4.7.

### 4.3.2      Designing the Class-F Output Matching Network

The class-F PA output harmonic matching network was designed for up to the 3$^{rd}$ harmonic. In section 4.2.1, the selected optimum fundamental load was 101.5Ω as it provides a balance between peak output power and efficiency at average power.  In the class-F mode of operation, the 2$^{nd}$ harmonic current is shorted and a high impedance is presented to the 3$^{rd}$ harmonic current component at the current generator plane [5].    The theoretical maximum efficiency with such configuration is 82% [6].

Therefore the output matching network consisted of three open or short-circuited stubs to cater for the 3 frequency components.  One of the stubs included a bias insertion network that will connect to the ET modulator via a through-hole pin.  The de-embedding information was used to translate the impedance at the current generator plane to the device package plane, resulting in the reflection coefficient values shown in Table 4.2.  These values were then used to design the output matching network using ideal transmission lines in Keysight ADS using the concept as shown in Fig. 4.8.

The 3$^{rd}$ harmonic impedance matching stub is located closest to the device and designed with a half-wavelength short circuit stub using a de-

coupling capacitor, isolating 3rd harmonic current from the fundamental and 2nd harmonic matching networks.  This also enabled the insertion of the drain bias network that connects to the ET modulator.   The 2nd harmonic matching network was therefore designed with the inclusion of the 3rd harmonic matching network in consideration, and an open-circuit quarter wavelength stub was used to isolate it from the fundamental matching network.  Subsequently, the fundamental load was designed with the inclusion of the 2nd and 3rd harmonic load matching networks.

| | Current generator plane | | Device package plane | |
|---|---|---|---|---|
| | Magnitude of reflection coefficient, $|\Gamma|$ | Angle of reflection coefficient, $\arg(\Gamma)$ | Magnitude of reflection coefficient, $|\Gamma|$ | Angle of reflection coefficient, $\arg(\Gamma)$ |
| Fundamental | 0.34 | 0° | 0.61 | 99.7° |
| 2nd harmonic | 1.00 | 180° | 1.00 | -151.8° |
| 3rd harmonic | 1.00 | 0° | 1.00 | 152.0° |

**Table 4.2 – Translating the output impedances at the current generator plane to the device package plane.**
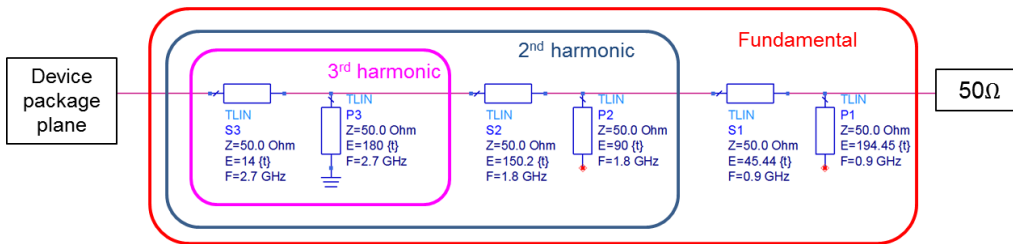


**Figure 4.8 – Class-F output matching network using ideal transmission lines.**

The resulting simulated impedances seen from the device package plane are shown in Fig.4.9, and the corresponding current generator plane impedances were close to the target values listed in Table 4.2
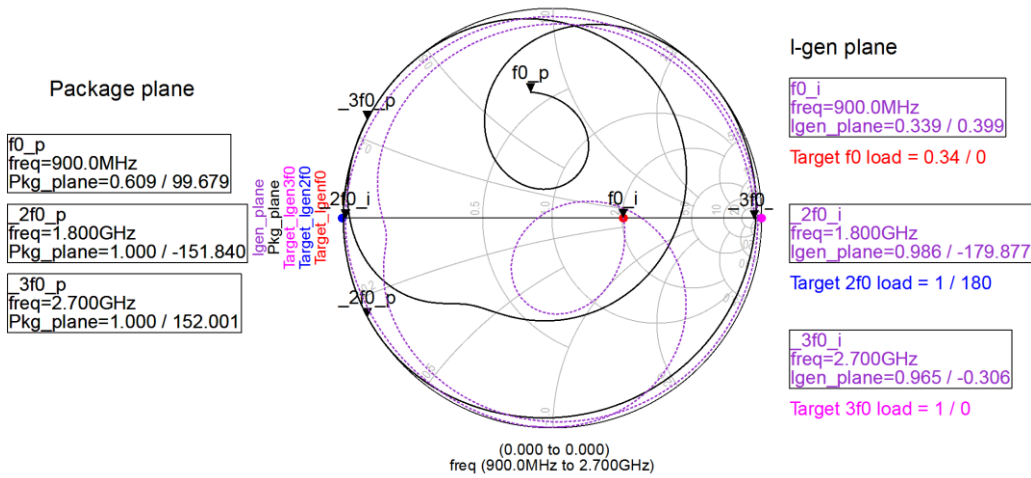
**Figure 4.9 - The resulting fundamental and harmonic loads at the device package plane (black), I-gen plane (purple), and the target I-gen plane loads (dots).**

The next step was to convert the ideal transmission lines (*TLIN*) into microstrip element (*MLIN*) in ADS using the substrate definition according to the 5880 RT/duroid specifications.  This was the intermediate step towards generating the layout of the network, and is shown in Fig. 4.10.
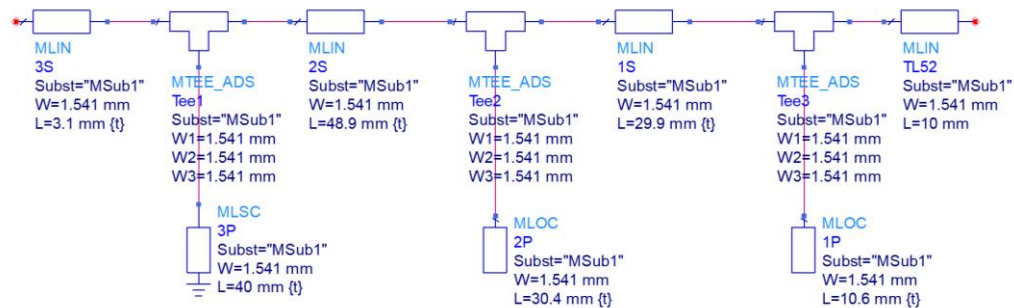


**Figure 4.10 - Output matching network using microstrip elements (*MLIN*) in ADS.**

The conversion from *TLIN* to *MLIN* added a lossy element to the network, and some small adjustment of the length of the transmission lines were required to bring back the loads to the right location on the Smith chart.

To understand the effect of transmission length inaccuracy, a quick analysis of the effect of length tolerance on the impedance seen by the current generator plane was performed using *MLIN*, as shown in Fig. 4.11.   This analysis was important as it provides a reference for troubleshooting the PA, in cases where the transmission line lengths needed to be modified after fabrication.   The magnitude and angle of the fundamental reflection coefficient, which was expected to impact the performance the most, was simulated to shift approximately by 0.005 and 0.66° respectively, for each 0.1mm change in transmission line length.
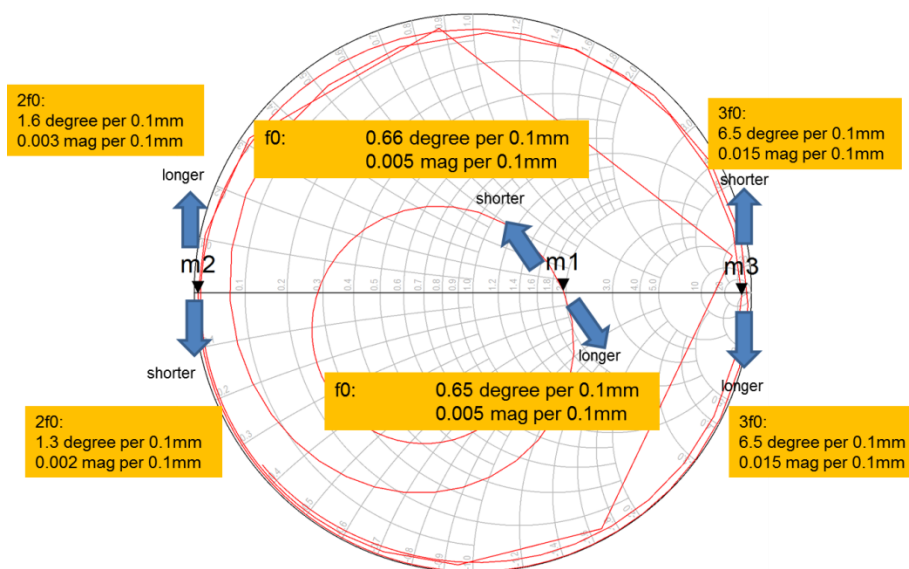


**Figure 4.11 - Simulating the tolerance due to transmission line lengths on the current generator plane impedances.**

### 4.3.3      Designing the Circuit Layout in ADS Momentum

The final step was to design the layout using ADS Momentum, where the lengths of the transmission lines were initially constructed to match the lengths obtained from schematic.   However as Momentum adds a more realistic lossy element to the simulation, further fine tuning of the lengths were

needed to pull the loads back to the original intended location, as much as possible. The lossy transmission lines mean that ideal short and open circuits were no longer possible at the current generator plane. Another addition to the design was the bias network at the 3rd harmonic short-circuited stub, 'behind' a decoupling capacitor. Fig. 4.12 shows the layout of the output matching network in Momentum and the impedances presented to the device package plane and current generator plane.
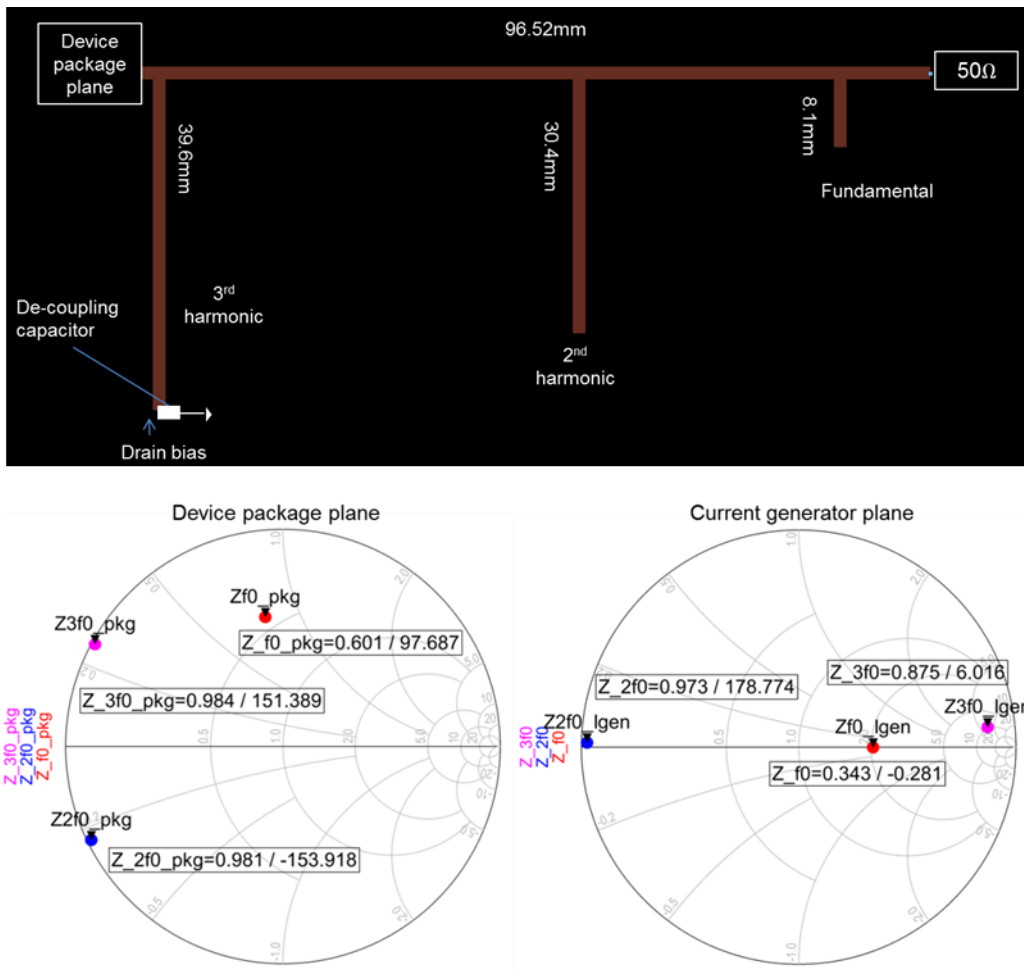


**Figure 4.12 - Output matching network layout in Momentum (above), the impedances it presents to the device package plane (bottom left) and current generator plane (bottom right).**

The class-F PA performance was verified using a Momentum co-simulation where the 2D-EM model of the output matching network was used in the schematic environment to run Harmonic Balance simulation.  Fig. 4.13 shows the simulated PAE performance at different drain bias values from 16V to 48V in 4V steps, operating at 900MHz.  The simulated output power peaked at 40.6dBm while the PAE peaked at approximately 3dB OBO from peak power.  At 7.5dB OBO, the simulated PAE was 71%.
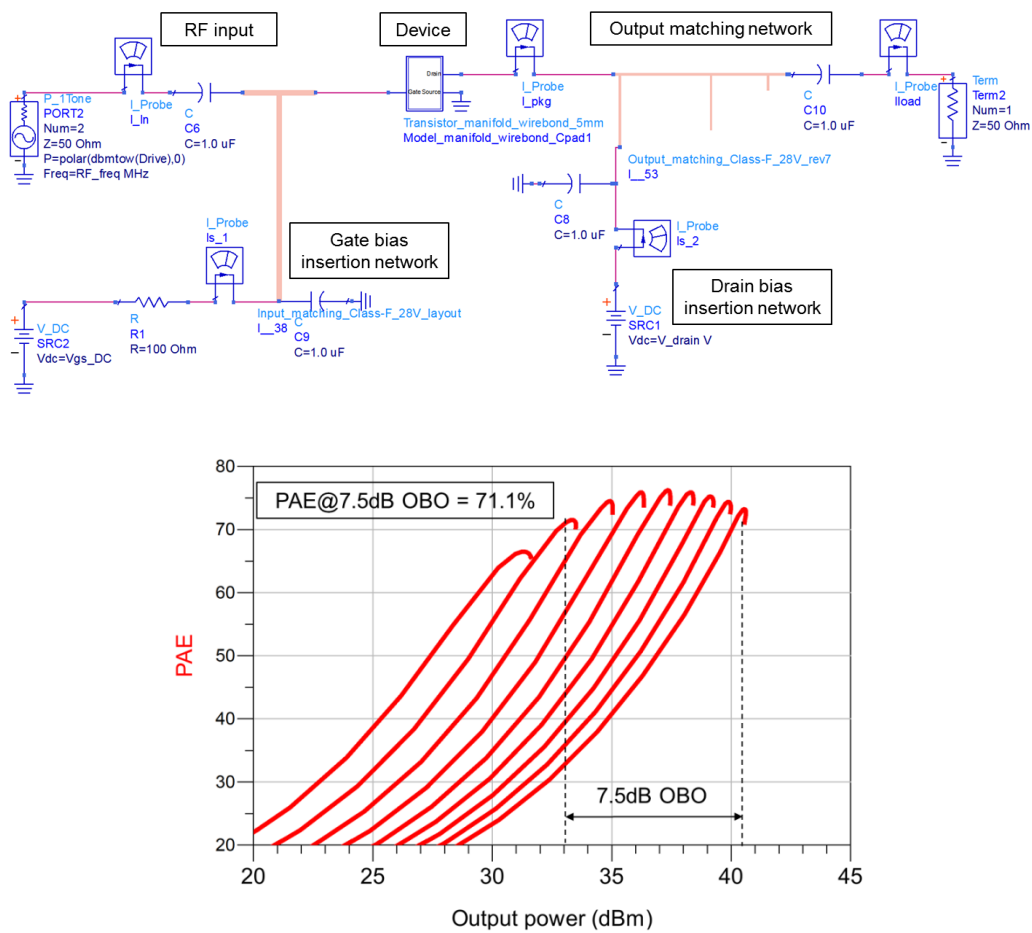
**Figure 4.13 - ADS Momentum co-simulation of the class-F PA (above) and the simulated PAE performance in static ET.**

76

**4.3.4     Completing the Layout**

The next addition to the layout was the connection for the drain bias input via the ET modulator. This was achieved by adding a hole near the 3rd harmonic matching stub, and following the de-coupling capacitor as shown in Fig. 4.14. The connection to the ET modulator was done by way of a through-hole pin that comes from the ET adapter as shown in Fig.4.6. In case the fundamental and 2nd harmonic open circuit stubs need to be extended after fabrication, some copper rectangles of the same width as the stubs were added during fabrication. Additionally, a small series resistor and some low-frequency filtering capacitors were added to the gate bias network for stability purpose. The class-F PA was fabricated in-house using a milling machine. Fig. 4.14 shows the final layout and the fabricated class-F PA.

## 4.4     Conclusions

Working with modulated signal of a known PAPR, a design method has been formulated using the waveform engineering approach to achieve an optimum efficiency-linearity performance of an RF PA for ET applications. The method utilizes the waveform engineering capability to determine the optimum load and a linearising shaping function.

The formulated design method has been used to design an actual class-F PA that will be integrated it into to a real ET system. The PA uses a 10W device from Freescale with a defined ET drain bias range of 16V to 48V. From simulation the RF PA efficiency at 900MHz at 7.5dB OBO was 71%, constrained by the output power requirement at peak power, while CW load-pull measurement data of the device predicted it to be 67%.
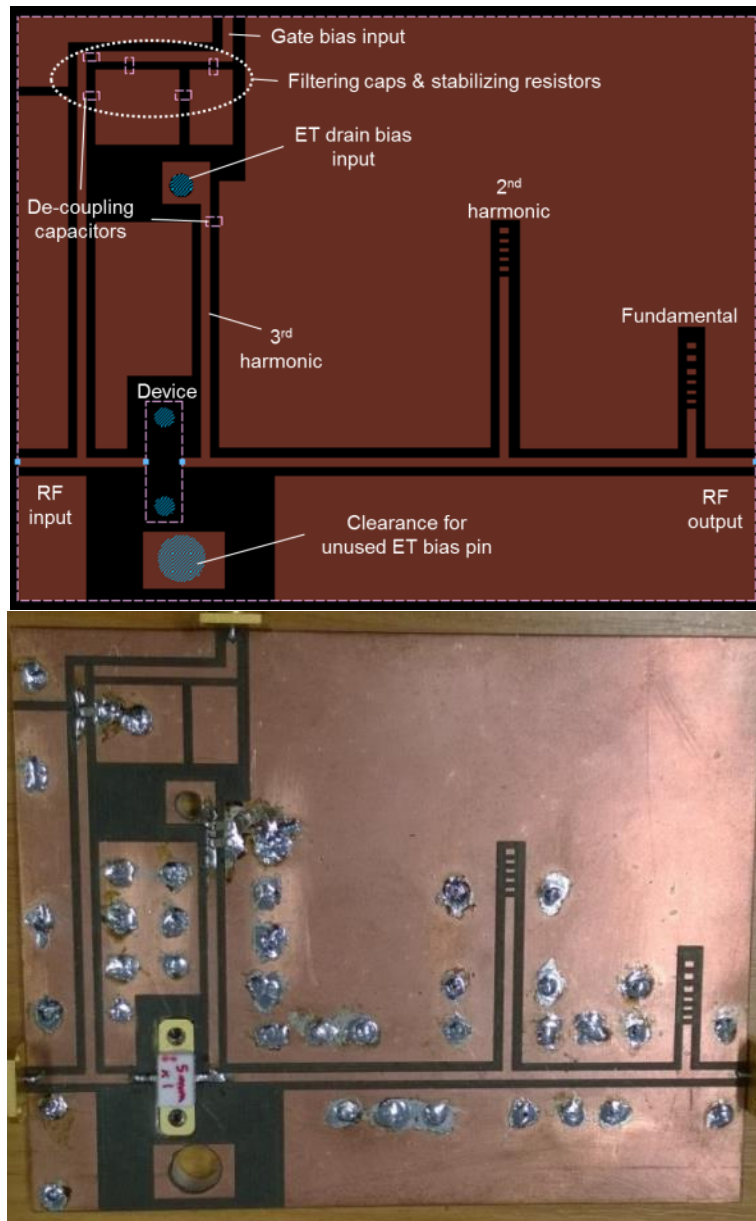
**Figure 4.14 - The final layout (top) and the fabricated class-F PA (bottom).**

The *flat-gain* shaping function is expected to produce a linear performance but its input range is limited on the low input level side, due to the defined minimum drain bias.

For this PA, the input matching circuit was not a priority and hence was not optimised for maximum gain. Therefore for the subsequent PA

performance analysis, the drain efficiency (DE) measurement was used instead of power-added efficiency (PAE).

In the next chapter, the PA performance is tested as a standalone amplifier using a CW signal to verify its performance before being paired up with an ET modulator in a full ET setup for a system level performance test with an LTE signal of 7.5dB PAPR.

## 4.5     References

[1]     E. McCune, *Dynamic Power Supply Transmitters*: Cambridge University Press, 2015.

[2]     Z. Wang, *Envelope Tracking Power Amplifiers for Wireless Communications*: Artech House, 2014.

[3]     M. Lasanen, M. Aubree, C. Cassan, A. Conte, J. David, S. E. Elayoubi*, et al.*, "Environmental friendly mobile radio networks: Approaches of the European OPERA-Net 2 project," in *Telecommunications (ICT), 2013 20th International Conference on*, 2013, pp. 1-5.

[4]     RT/duroid ® 5870/5880 High Frequency Laminates Datasheet [Online]. Available:     http://www.rogerscorp.com/documents/606/acs/RT-duroid-5870-5880-Data-Sheet.pdf

[5]     S. C. Cripps, *RF Power Amplifiers for Wireless Communications*: Artech House, 2006.

[6]     F. H. Raab, "Maximum efficiency and output of class-F power amplifiers," *IEEE Transactions on Microwave Theory and Techniques,* vol. 49, pp. 1162-1166, 2001.

# Chapter 5

# Envelope Tracking System Level Integration and Testing

## 5.1      Introduction

In the previous chapter, the design flow of an RF PA for ET applications utilising waveform engineering has been demonstrated.  A 10W class-F RF PA has been fabricated using this formulation.

In this chapter, the test method and results of the fabricated class-F PA are presented, first as a standalone PA and then integrated into a real ET system at Arelis, France.  Due to the test setup limitation at Arelis, the ET system level test was performed at 885MHz, which was found to still be within the capability of the class-F PA.  The advantages and limitations of using a class-F PA in an ET system are explained together with simulation results that replicate the ET system level test.

## 5.2      Initial PA Standalone Performance Test

### 5.2.1      Efficiency & Output Power using CW Signal

The fabricated class-F PA was first tested as a standalone amplifier in a static-ET setting using a CW signal at 900MHz to verify its performance.  For this CW test the drain was biased through a wire soldered onto the drain bias terminal and connected to a DC supply.  Replicating the static ET procedures

from the load-pull testing stage, the drain bias was stepped from 16V to 48V in 4V steps and for each drain bias a power sweep was performed. Fig. 5.1 shows the drain efficiency and gain curves for each $V_{DS}$ from 16V to 48V in 4V steps at 900MHz.

The drain efficiency peaked at 73% at approximately 3dB from peak power, which was the trend predicted by the ADS Momentum co-simulation in Fig. 4.13, although the simulated peak efficiency was higher by 3%. At 7.5dB output back-off the drain efficiency from this CW measurement was 68%. It was observed that the location of the de-coupling capacitor at the output matching network along the 3$^{rd}$ harmonic matching stub had a significant impact on drain efficiency, as this effectively alters the load termination of the 3$^{rd}$ harmonic and the fundamental. This was further confirmed through Momentum co-simulation where the location of the de-coupling capacitor was varied by 3mm on the layout and the drain efficiency dropped by approximately 5%-point.

The measured trade-off in efficiency was approximately 2% if the applied ET shaping function targeted a constant gain operation. This was also consistent with the load-pull characterisation results in Fig. 4.3. However the optimum gain value was now lower (14dB) because the input was not properly matched.

In preparing for the ET system level test, the PA efficiency performance was also measured at 885MHz. As shown in Fig. 5.1, this caused the peak efficiency to drop by approximately 2%-point but it also moves the peak efficiency region much closer to the average power.
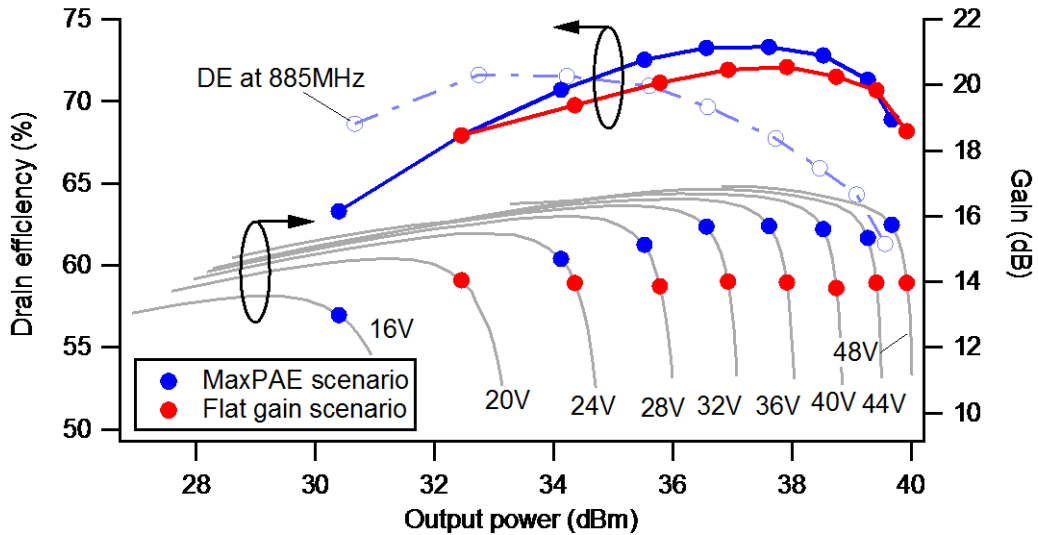
**Figure 5.1 - Measured PA gain characteristics and efficiency.**

## 5.3 Integrating the Class-F PA into the ET System

### 5.3.1 The Arelis ET System

The integration of the class-F PA into an ET system was performed at Arelis, France, one of the Opera Net 2 project partners who developed the prototype system as part of the project deliverables. The heart of the FPGA-based system is a proprietary ET drain modulator which has a bandwidth of 40MHz and efficiency of 93%. It is designed to work with a 50V device and capable of providing an output voltage from 16V to 50V.

The ET drain modulator is connected to the class-F PA via an adapter board which provides 2 drain bias feed points from the modulator via through holes. The class-F PA has a through-hole connection to accommodate one of the drain bias feeds. Suitable bypass capacitors that are small enough not to significantly load the baseband signal components need to be placed on the class-F PA drain bias path to prevent the RF power from going into the ET drain modulator and also to prevent ringing in the bias signal.

The ET system is controlled using software developed by Arelis, which generates a 5MHz LTE signal from a pseudo-random bit sequence (PRBS) baseband and has a signal PAPR of 7.5dB. The power level is adjusted using an intermediate-frequency (IF) gain control panel to ensure the PA reaches a suitable compression level. The envelope shaping function is entered manually by the user through a graphical user interface which shows a plot of the drain supply versus the input envelope, as shown in Fig. 5.2. The interface allows the user to set 7 points on the graph to alter the shaping function of the ET modulator. The system also has digital pre-distortion (DPD) capability to perform nonlinear correction on the PA and improve the adjacent channel power ratio (ACPR) performance.
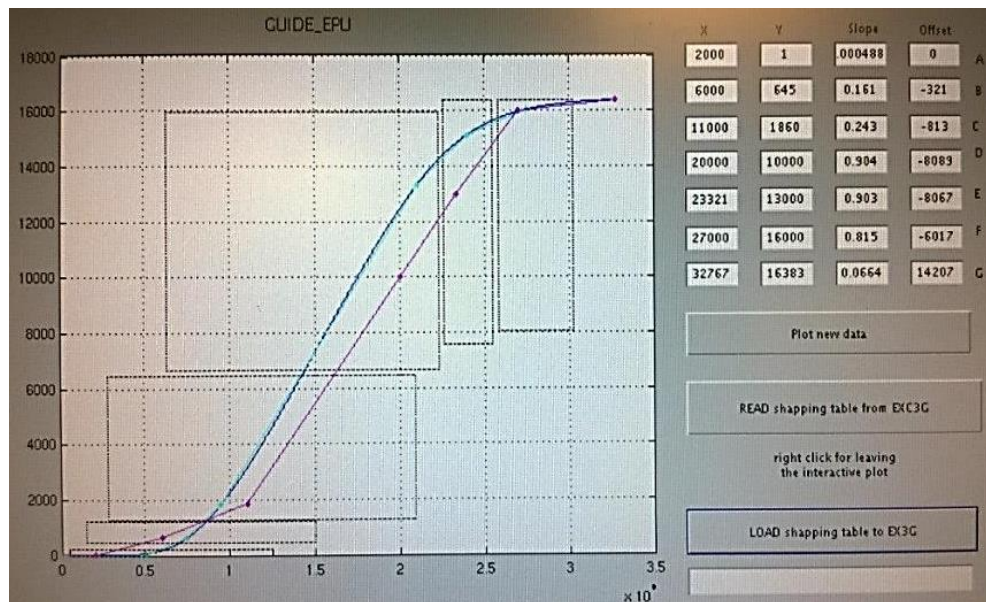


**Figure 5.2 - ET shaping function entry.**

## 5.3.2    Integrating the Class-F PA into the ET System: Hardware Connections

The class-F PA was mechanically attached to the ET adapter board to allow for the drain feed pin to be inserted through the hole that was designed

for it as previously shown in Fig. 4.14, with an insulating Teflon dielectric to hold it within. The other end of the adapter board was connected to the ET drain modulator and the control board. To monitor the modulated ET drain bias signal, a cable was soldered onto the drain bias feed pin and connected to an oscilloscope with a series resistor. A second oscilloscope channel was used to monitor the LTE RF input signal. The gate was biased using a separate DC power supply. Fig. 5.3 shows the hardware connections to the class-F PA.
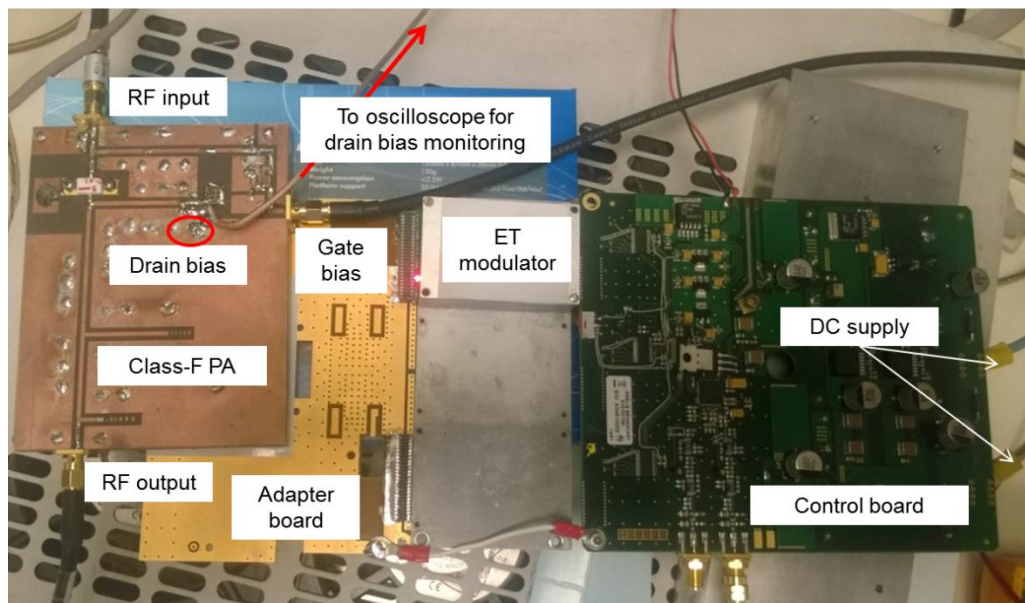


**Figure 5.3 – Hardware connections to the class-F PA.**

The same Minicircuit ZHL-42 driver amplifier that was used during load-pull at Cardiff lab was used again in this system to boost the input power. The output of the class-F PA was connected to a coupler which then terminated into a 50Ω load. The coupled arm of the coupler was split using a power splitter and characterised and connected to a spectrum analyser and a power sensor.

The ET control board was powered by a DC supply unit that supplied 48VDC to the ET modulator as well as to the digital control circuitry that can turn the modulator on or off.  A digital multimeter was connected in series between the DC supply unit and the ET control board to enable current measurement.  Fig. 5.4 shows the test setup with its block diagram.
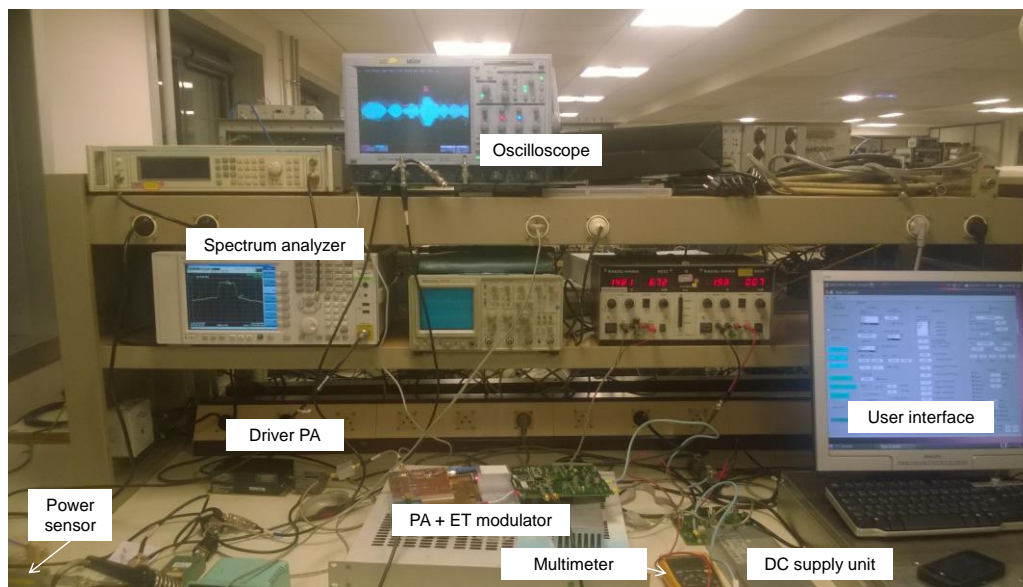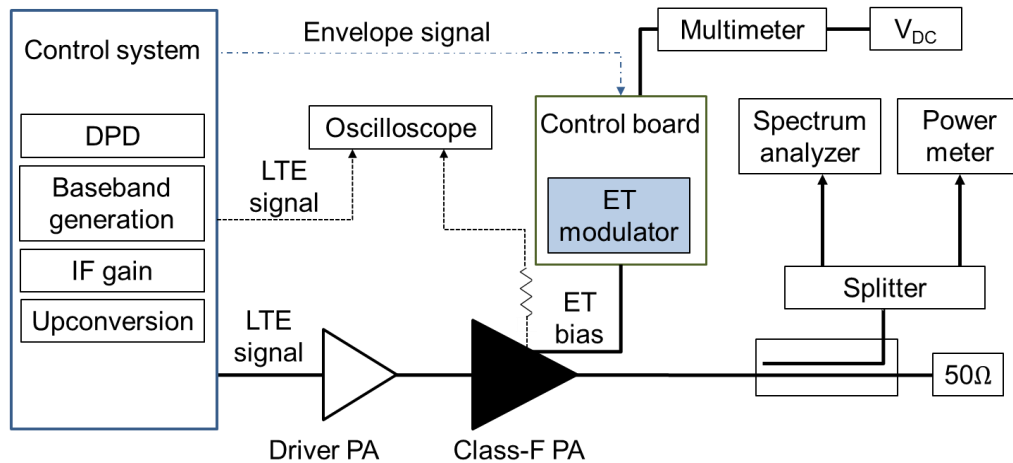


**Figure 5.4 – The Arelis ET test setup.**

### 5.3.3     ET Test Setup & Method

The combined DC power consumption of the ET drain modulator and the class-F PA was calculated as the product of the supplied DC voltage

(48VDC) and the measured incremental DC current when the ET modulator was turned on. The power consumption of the control board, which had been characterised to be 90% efficient, was not taken into account in this case. It was not possible to measure the efficiency of the class-F PA alone from the combined efficiency of the ET modulator and the class-F PA, but it can be estimated since the efficiency of the modulator was previously characterised to be 93%.

Due to the frequency limitation of the ET system, the centre frequency of the input signal was limited to 885MHz instead of 900MHz, which was still within the operating frequency range of the PA, as shown in Fig. 5.1. In fact with the lower frequency the PA efficiency profile changed such that it peaked around the average power, but the peak power was now reduced by 0.5dB to 39.2dBm.

The system IF gain was used to adjust the average output power to approximately 32dBm, which was the estimated average power based on CW characterisation. The effect of the IF gain adjustment was also characterised by sweeping its value and observing the effect on efficiency and linearity.

Several changes were made to the shaping function to observe its effect on the performance. The shaping functions that would replicate the *max-PAE* and *flat-gain* shaping functions were also applied.

The Arelis control software also has the capability to perform nonlinear correction to provide DPD capability. The non-linear correction was applied in this measurement to observe the improvement in measured ACPR. The input

signal had a 5MHz bandwidth and the adjacent channel power was measured

at a 5MHz offset.  Fig. 5.4 shows the Arelis ET system test setup.

## 5.4      ET Measurement Results & Discussions

### 5.4.1      De-coupling Capacitor Change

Initial observation showed ringing effect in the ET modulated drain bias

signal.  To reduce this effect, two 2.7nF bypass capacitors at the 3$^{rd}$ harmonic

short circuit stub were removed and lower values were tested.  It was found

that empirically a 470pF capacitor was able to remove the ringing effect.  It was

observed that the peak drain efficiency at a single bias without ET was close to

70%, indicating that the original performance was still maintained after the

changes made to the de-coupling capacitor.
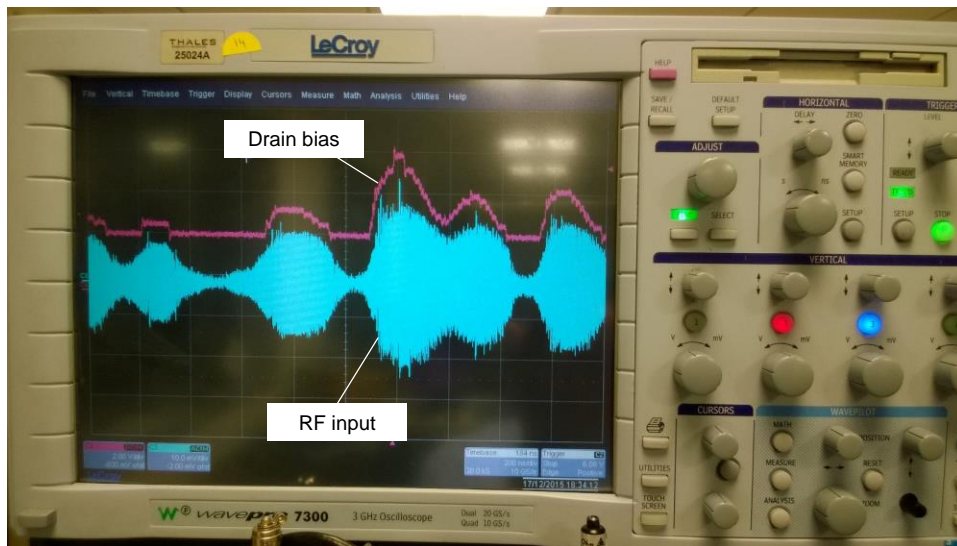


**Figure 5.5 - Oscilloscope display of RF input and drain bias.**

Fig. 5.5 shows the ET modulated drain bias signal and the LTE RF

input signal measured on the oscilloscope display, indicating that the ET

operation was behaving as expected.

### 5.4.2      Adjusting the IF Gain

The IF gain is a variable gain control parameter during the up-conversion stage of the LTE input signal. The effect of IF gain adjustment on the ET PA system performance was characterised by performing a sweep over its range, as shown in Fig. 5.6. The average power was observed to reach 32dBm when the IF gain was set to -9dB and the PA started to go deeper into compression as the IF gain was increased further.

The average drain efficiency of the PA + ET modulator combination was initially just below 40% at 32dBm average output power and the ACPR at 5MHz offset was -23dBc. The low efficiency performance at this point was due to an un-optimised shaping function.
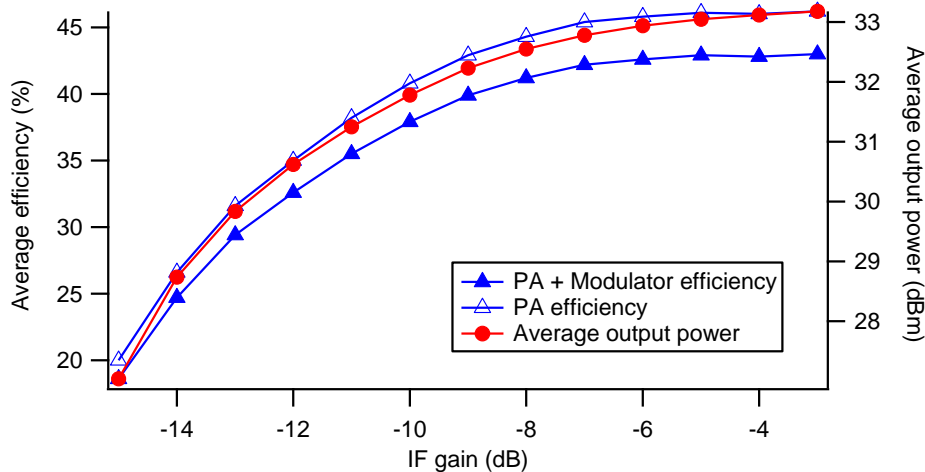


**Figure 5.6 - Characterizing the effect of IF gain.**

### 5.4.3      Applying the Shaping Functions

Finally the shaping function was modified using the FPGA-based controller. In this ET system level test, two different shaping functions were applied in an attempt to replicate the shaping functions formulated in Chapter

3.  The minimum drain bias was clipped to 16V as this was the ET modulator lower limit.   However since the shaping function entry works in the digital domain and uses DAC values, only an estimate of the shaping function was used (Fig. 5.7).   The IF gain was re-adjusted to bring the average power to approximately 32dBm.   Table 5.3 shows the comparison of average drain efficiency and ACPR results when these 2 shaping functions were used.

The measured average efficiency for the class-F PA + ET modulator combination was 64% using the *max-PAE* shaping function.   With the efficiency of the modulator previously characterised to be 93%, the calculated PA-only average efficiency was 69% which was slightly lower than the measured efficiency at CW.  This is expected and the difference between them depends on the time-domain profile of the signal.   The 64% combined efficiency obtained with a 10W LDMOS device was relatively high compared to the work done in [1] where a 10W GaN device operating in ET at 889MHz achieving 60% drain efficiency when excited using a 5MHz LTE signal with a 6.5dB PAPR.

| | Average efficiency (PA + ET Modulator) | Average efficiency (PA only) | Average output power | ACPR @5MHz offset without DPD | ACPR @5MHz offset with DPD |
|---|---|---|---|---|---|
| Replicating max PAE shaping function | 64% | 69% | 32.2 dBm | -27 dBc | -32 dBc |
| Replicating flat gain shaping function | 61% | 66% | 32.0 dBm | -27 dBc | -32 dBc |

**Table 5.1 - ET performance results.**

It was found that using the quadratic-shape shaping function to replicate the *flat-gain* shaping function the average efficiency did drop by

approximately 3%-point but the ACPR performance did not improve.   The

ACPR performance in this case did not vary from the ACPR performance when

using the first shaping function, which targeted maximum efficiency.  This could

be due to a few reasons.  Firstly the shaping function entry in the ET system

level was done in the digital domain interface using DAC values as shown in

Fig. 5.7.  This factor, accompanied by the limited resolution in the shaping

function curve only allowed for an estimation of the desired shaping function

and there could be room for further optimisation in the shaping function used.

The correlation between the PA gain characteristics against the load-pull

results where the shaping function was formulated could have also contributed

to this uncertainty.   However, the DPD correction that was applied in these

measurements would have corrected the AM-AM response that resulted from a

non-optimised *flat-gain* shaping function.
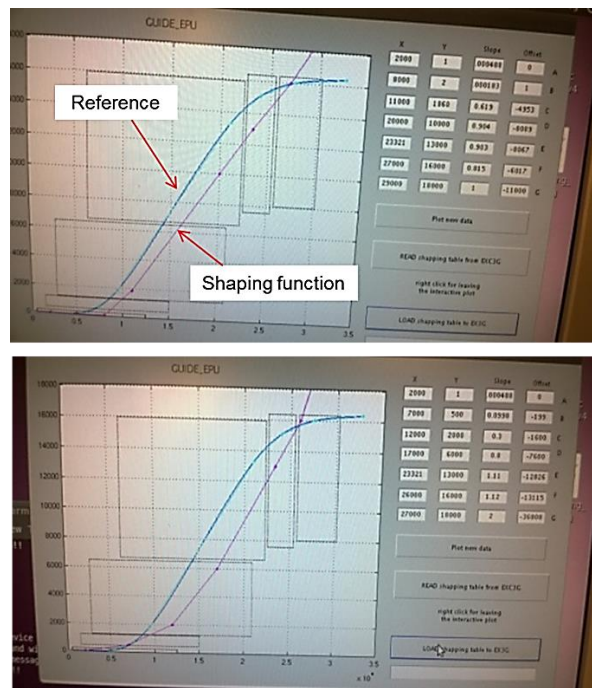


**Figure 5.7 - Shaping function to replicate optimisation for efficiency (above) and linearity (bottom).**

The main contributor to the linearity performance in this case was suspected to be the soft turn-on characteristic of the class-F PA transconductance as a result of a class-B bias. This effectively means that the *flat-gain* shaping function can only linearise the upper half of the output power range but will not be able to correct for the nonlinearities of the lower half of the dynamic range, as seen in section 4.2.

The DPD used in this system was designed to work with class-AB type of amplifiers where they are biased at a distance away from the pinch-off region, avoiding the nonlinearity from the soft turn-on effect at very low drive levels. Therefore the use of DPD in this setup was not able to correct for the nonlinearity at the very low drive level but was more effective at the compressive region of the transconductance curve at the top end. Fig. 5.8 shows the spectral plot before and after applying the DPD from the Arelis ET system.



**Figure 5.8 - Spectral display of the output signal before (left) and after (right) applying DPD.**

## 5.5 Verifying the Measured ET Test Results in Simulation

To further verify the ET efficiency and linearity results, an ADS simulation was established to replicate the ET system level measurements performed at the Arelis facilities.

### 5.5.1 CW Simulation to Generate Shaping Functions

Fig. 5.9 shows the CW simulation that was done as part of Chapter 4's design flow formulation shown in Appendix B. From this result, 2 shaping functions were derived: targeting a constant 14.5dB gain (*flat-gain*) and maximum efficiency (*max-PAE*).
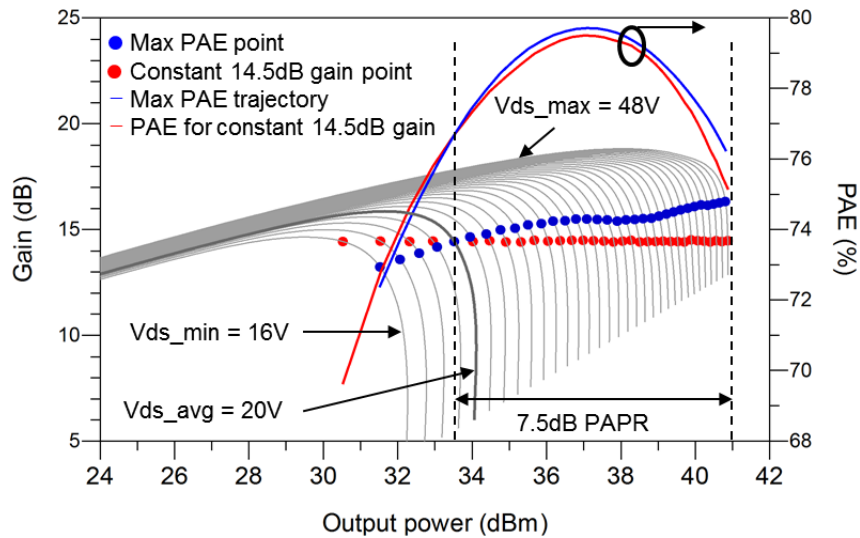


**Figure 5.9 - CW characterisation to extract ET shaping functions**

### 5.5.2 ET System Simulation Setup

The ET simulation setup, shown in Fig. 5.10 is a modified version of the Keysight template and uses an Envelope simulation controller and ideal symbolically-defined devices (SDDs) for the ET modulator. Only the efficiency of the RF PA is considered while the ET modulator is considered ideal.

The input signal is a 5MHz LTE that is read from a signal source dataset, and the adjustable parameters are the gain and centre frequency. An *IQ_DemodTuned* element which has a high input impedance is used to sample the input signal and demodulate it into in-phase (I) and quadrature (Q) components whose squared values are summed up by an *SDD3P* element. This summation produces the squared envelope signal and therefore the envelope value can be calculated to retrieve the corresponding drain voltage from a *DataAccessComponent* (*DAC*) element.
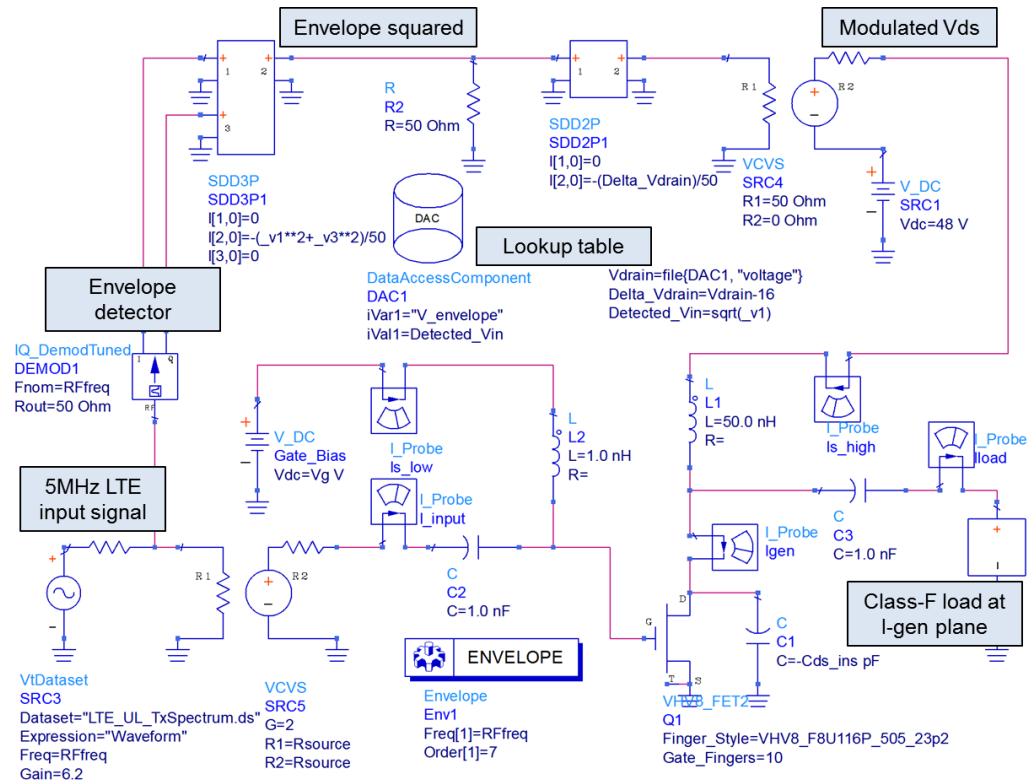


**Figure 5.10 - System level ET simulation setup using ideal ET drain modulator.**

The *flat-gain* and *max-PAE* shaping functions are applied in this envelope simulation. The device is presented with the same class-F fundamental and harmonic loads at the current generator plane that were used for the PA design. The input power, which is controlled by the gain parameter

of the LTE source is adjusted to provide the average power of approximately 33.5dBm as a reference point as obtained from Fig. 5.9.

### 5.5.3 ET System Simulation Results & Discussion

The resulting shaping functions and a time domain snapshot of their drain supply profiles when aligned against the LTE input envelope signal are shown in Fig. 5.11. As expected, when the input voltage swings below 2V, the drain bias remains at 16V since this was the minimum bias voltage.
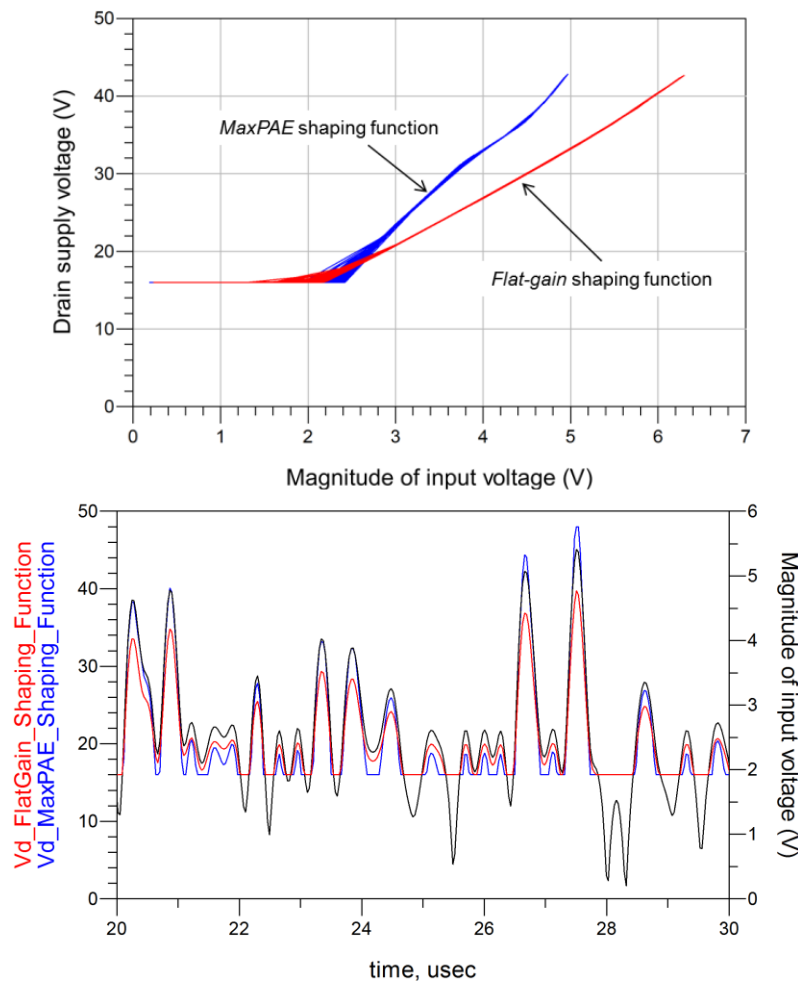


**Figure 5.11 – Top: the 2 shaping functions used in this ET system simulation. Bottom: a snapshot of the resulting drain supply against the input signal.**

Fig. 5.12 shows the PAE comparison between the 2 shaping functions and the corresponding output power distribution while Table 5.4 lists the performance comparison.
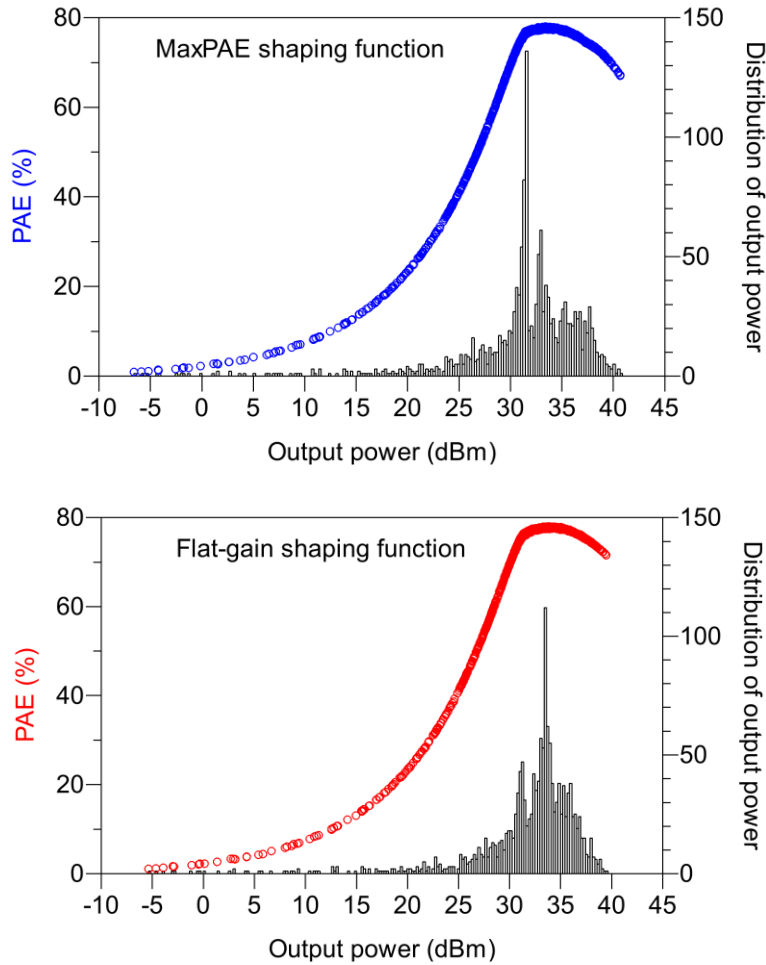


**Figure 5.12 – Simulated PAE comparison and distribution of output power between the 2 shaping functions.**

|                        | *Max-PAE* shaping function | *Flat-gain* shaping function |
|------------------------|----------------------------|------------------------------|
| Average output power   | 33.5 dBm                   | 33.5 dBm                     |
| Peak power             | 40.7 dBm                   | 39.5 dBm                     |
| Signal PAPR            | 7.1 dB                     | 6.0 dB                       |
| PA average efficiency  | 73.6 %                     | 75.1 %                       |
| Lower channel ACPR     | -25.7 dB                   | -28.5 dB                     |
| Upper channel ACPR     | -28.7 dB                   | -32.0 dB                     |

**Table 5.2 - Simulated performance comparison between the two shaping functions.**

95

Several observations can be made about the simulation results. Firstly, the average efficiency was 1.5%-point higher for the *flat-gain* shaping function for this 5MHz LTE input signal. This was initially indicated from Fig. 5.9 where not only the trade-off in PAE was observed to be minimal when the *flat-gain* shaping function was in use, but also, below the average power the PAE for the *flat-gain* shaping function started to go higher than the *max-PAE* shaping function.

Secondly, the output signal PAPR varied with the shaping function used because of the gain variation at different drain voltages. The *max-PAE* shaping function has a relatively higher overall gain than the *flat-gain* shaping function. In this simulation in order to get the same average power of 33.5dBm, the signal PAPR was 7.1dB and 6.0dB for the *max-PAE* and *flat-gain* shaping functions, respectively. If the PAPR was used as a normalizing factor the resulting average power would be different.

Thirdly, in this simulation the flat-gain shaping was formulated to obtain a constant 14.5dB gain as shown in Fig. 5.9, which takes effect from peak power to 10dB output back-off. Although its resulting ACPR performance was found to be approximately 3dB better than the *max-PAE* shaping function, it was only able to reach -32dBc at best. This number was very close to the measured ACPR performance with DPD applied in Table 5.1, where the DPD takes on the role of flattening the gain profile across the output power range. Fig. 5.13 shows the simulated spectral plots for the 2 shaping functions.

A closer look into the simulated transconductance plot in Fig. 5.13 shows that the *flat-gain* shaping function produces a linear relationship

between the output current and the input voltage, but only for input voltage range of above 2V magnitude. At lower input level, the soft turn-on characteristics of the class-B bias started to contribute to the nonlinear transconductance. This soft turn-on characteristic was also present when using the maximum PAE shaping function, as it was caused by the gate bias and not able to be corrected by the ET shaping function. This was also the case when DPD correction is applied, as only the higher input voltage gets corrected for linearity leaving residual nonlinearities coming from low input level. Although the effect of DPD was not simulated here, the *flat-gain* shaping function was supposed to perform the same role.
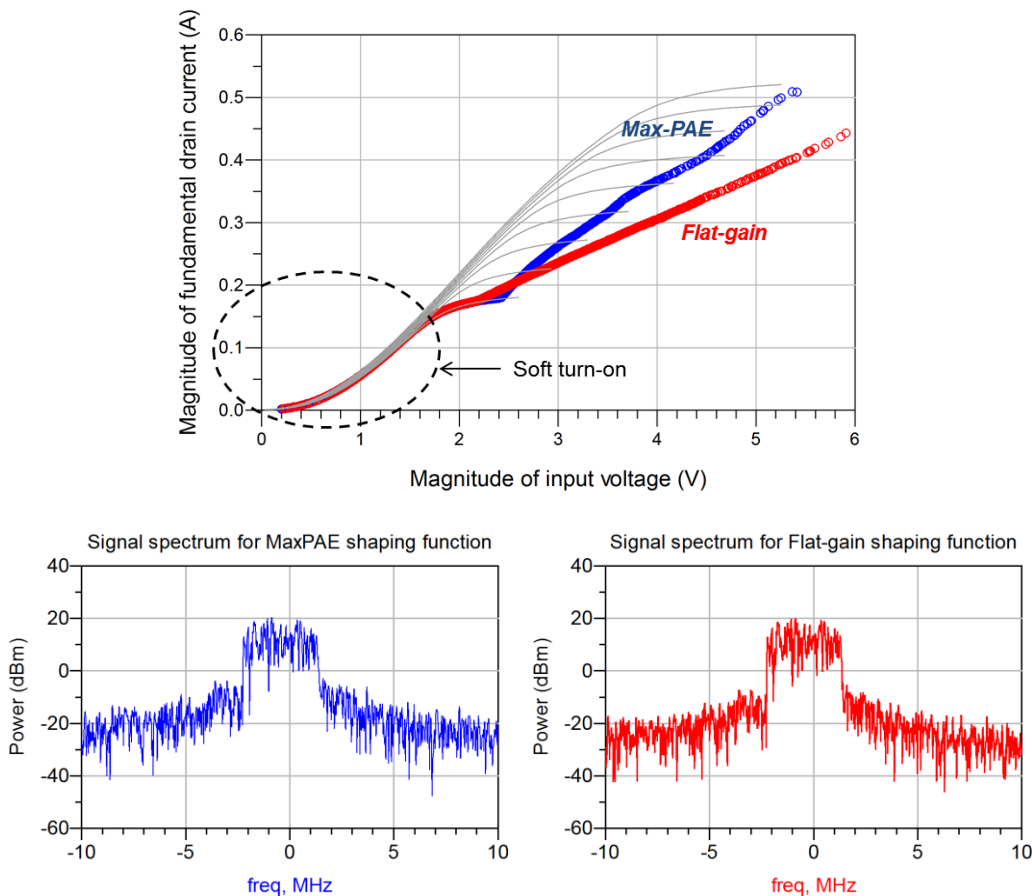


**Figure 5.13 – Top: Simulated transconductance curve with ET. Bottom: simulated signal spectrum for the *max-PAE* (left) and *flat-gain* (right) shaping functions.**

## 5.6     Conclusions

The integration of the class-F PA into a real ET system has been presented. The measured ET drain efficiency for the PA and ET modulator combination was 64% with a 5MHz LTE input signal. This number potentially can be improved with the use of a GaN device which has a smaller knee region and output capacitance. Even so, this efficiency performance is among the highest compared to the state-of-the-art ET PA's in [1-10] which were mostly GaN-based, as shown in Fig. 5.14.
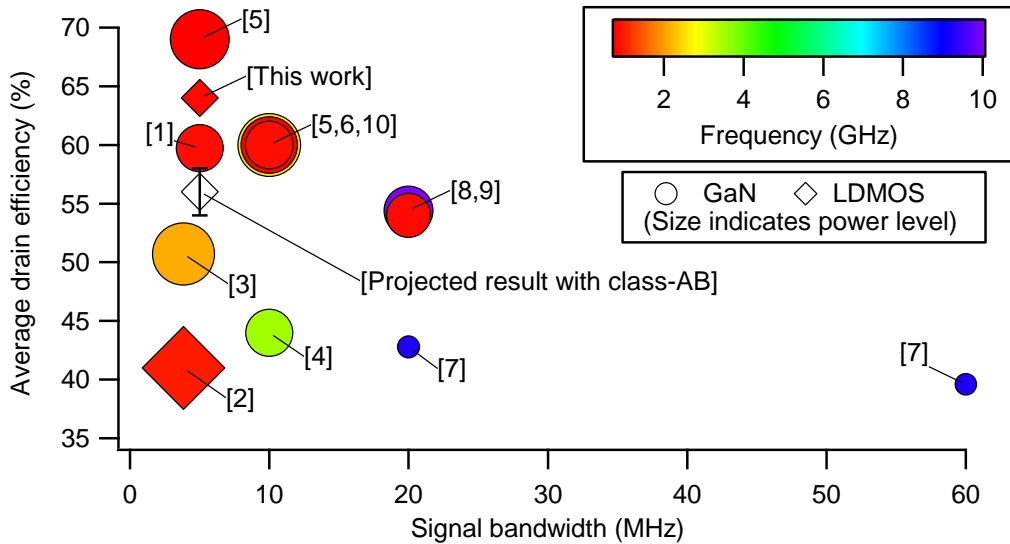


**Figure 5.14 – Comparison with state-of-the-art ET PA's. The projected result from this work if class-AB was used is also included.**

The main challenge in using class-F mode PA in ET is the linearity performance. The best-case measured ACPR was -32dBc due to the limitation of the soft turn-on region not being able to be corrected by DPD. As a comparison, the class-AB mode used in [1] achieved -45dBc while the class-AB PA in ET from the Opera Net 2 project achieved -40dBc, both with DPD. Based on the CW measurement and simulation data, the class-AB efficiency was approximately 8 to 10%-point lower than class-F for this device. With its

higher gate bias point it is expected to produce comparable ACPR results, trading-off efficiency. The projected result if class-AB was used in this work is also shown in Fig. 5.14

Another way to address this is to have a gate bias variation as a function of the input envelope, which would raise the gate bias above pinch-off at low input levels, just enough to meet the desired ACPR performance. This is explored in simulation in Chapter 8 under *Future Work*, which presents an opportunity of improving linearity while retaining some level of class-F efficiency performance. Another way is to use an alternative nonlinear correction method that would also address the nonlinearities at low input levels.

Another aspect of the PA performance that was not discussed in this chapter is bandwidth. The class-F PA has a limited bandwidth from its narrowband matching network design. The continuous class-F mode, which is an extension of this class-F mode developed to increase its bandwidth will be discussed the next chapter, where the behaviour of continuous mode PA's in a variable drain setting for an LDMOS device is investigated.

## 5.7    References

[1]    K. Jungjoon, S. Jungwhan, J. Seunghoon, K. Seokhyeon, and K. Bumman, "Optimization of Envelope Tracking Power Amplifier for Base-Station Applications," *Microwave Theory and Techniques, IEEE Transactions on,* vol. 61, pp. 1620-1627, 2013.

[2]    P. Draxler, S. Lanfranco, D. Kimball, C. Hsia, J. Jeong, J. van de Sluis*, et al.*, "High Efficiency Envelope Tracking LDMOS Power Amplifier for W-CDMA," in *Microwave Symposium Digest, 2006. IEEE MTT-S International*, 2006, pp. 1534-1537.

[3]    D. F. Kimball, J. Jeong, H. Chin, P. Draxler, S. Lanfranco, W. Nagy*, et al.*,    "High-Efficiency    Envelope-Tracking    W-CDMA    Base-Station

Amplifier Using GaN HFETs," *Microwave Theory and Techniques, IEEE Transactions on,* vol. 54, pp. 3848-3856, 2006.

[4]　J. H. Kim, G. D. Jo, J. H. Oh, Y. H. Kim, K. C. Lee, J. H. Jung*, et al.*, "High-Efficiency Envelope-Tracking Transmitter With Optimized Class-F-1 Amplifier and 2-bit Envelope Amplifier for 3G LTE Base Station," *IEEE Transactions on Microwave Theory and Techniques,* vol. 59, pp. 1610-1621, 2011.

[5]　J. J. Yan, P. Theilmann, and D. F. Kimball, "A High Efficiency 780 MHz GaN Envelope Tracking Power Amplifier," in *2012 IEEE Compound Semiconductor Integrated Circuit Symposium (CSICS)*, 2012, pp. 1-4.

[6]　H. Tango, T. Hashinaga, K. Totani, H. Kuriyama, Y. Hamada, and T. Asaina, "A 60% efficient envelope tracking power amplifier for 40W, 2.6GHz LTE base station with in/output harmonic tuning," in *Microwave Symposium Digest (IMS), 2013 IEEE MTT-S International*, 2013, pp. 1-4.

[7]　P. T. Theilmann, J. J. Yan, C. Vu, J. S. Moon, H. P. Moyer, and D. F. Kimball, "A 60MHz Bandwidth High Efficiency X-Band Envelope Tracking Power Amplifier," in *2013 IEEE Compound Semiconductor Integrated Circuit Symposium (CSICS)*, 2013, pp. 1-4.

[8]　G. Collins, J. Fisher, F. Radulescu, J. Barner, S. Sheppard, R. Worley*, et al.*, "C-band and X-band class F, F-1 GaN MMIC PA design for envelope tracking systems," in *Microwave Conference (EuMC), 2015 European*, 2015, pp. 1172-1175.

[9]　Y. Liu, C. S. Yoo, J. Fairbanks, J. Yan, D. Kimball, and P. Asbeck, "A 53% PAE envelope tracking GaN power amplifier for 20MHz bandwidth LTE signals at 880MHz," in *2016 IEEE Topical Conference on Power Amplifiers for Wireless and Radio Applications (PAWR)*, 2016, pp. 30-32.

[10]　J. Kim, J. Moon, J. Son, S. Jee, J. Lee, J. Cha*, et al.*, "Highly efficient envelope tracking transmitter by utilizing sinking current," in *Microwave Conference (EuMC), 2011 41st European*, 2011, pp. 1197-1200.

# Chapter 6

# Utilising Continuous Mode Power Amplifiers in Envelope Tracking & the Varactor Effect

## 6.1    Introduction

High-efficiency mode power amplifiers such as class-F provide a high-efficiency performance but only over narrow bandwidth because the optimisation of the output matching network is done at a single frequency. To mitigate this limitation and maintain a high efficiency performance over wider bandwidth, a concept of extending the design space for the PA modes was introduced by Cripps and Tasker in [1]. In that work, a new design space was presented identifying a continuum between class-B and class-J, enabling a design that maintains a class-B performance in terms of power and efficiency, and that as a result paves the way for high-efficiency mode design over considerable bandwidth. In [2] the continuous mode theory was extended to class-F, validating a new design space using an active load-pull measurement setup that led to the realization of a continuous class-F PA in [3] which produced a class-F level efficiency of 74% over an octave bandwidth using a 10W GaN device, with only a small variation in output power.

For the same periphery, an LDMOS device however has a relatively large output capacitance compared to GaN [4] and its operation in a

101

continuous class-F mode of operation has not been experimentally investigated before in literature at the time of writing.

The first objective of this chapter is to fill this gap and investigate how far the class-F power amplifier performance obtained with an LDMOS device in Chapter 4 can be maintained over bandwidth, which is represented by the continuous class-F mode of operation.

The second objective is to explore the application of a continuous mode PA in an envelope tracking (ET) setting. A theoretical analysis of integrating a continuous class-F amplifier in ET was first presented in [5], but in this case the analysis was limited to simulation and did not include an experimental validation. This chapter aims to extend that analysis for both simulation and load-pull measurements, in a variable drain bias environment which represents an ET application.

The third objective of this chapter is to identify and analyse in detail the limitations presented by the nonlinear output capacitance $C_{DS}$ to the continuous mode of operation.

This chapter begins with an overview of the continuous mode theory of class-BJ and continuous class-F, followed by the experimental investigation of applying continuous class-F to an LDMOS device in fixed and variable drain bias settings. The results obtained from simulation and measurements suggest some difficulty of maintaining a continuous mode of operation due to the variation of the device $C_{DS}$ as a function of output voltage, or the varactor effect. The final section of this chapter presents a novel mathematical analysis

to show the positive and negative contribution of this varactor effect on continuous mode operation.

## 6.2      Formulation of the Continuous Class-BJ and Class-F

The formulation of the continuous mode is explained in detail in Appendix C. In summary, the continuous mode applies a raised sine function of the continuous mode operator $(1 - \alpha \sin \vartheta)$ to the class-B and class-F output voltages, as shown below for a 3-harmonic voltage component [6]:

$$V_{Cont\_BJ} = V_{max}(1 - \cos \vartheta) \cdot (1 - \alpha \sin \vartheta) \tag{6.1}$$

$$V_{Cont\_F} = V_{max} \left( 1 - \frac{2}{\sqrt{3}} \cos \vartheta + \frac{1}{3\sqrt{3}} \cos 3\vartheta \right) \cdot (1 - \alpha \sin \vartheta) \tag{6.2}$$

The range of α is defined from -1 to 1 in order to keep the voltage above zero. Fig. 6.1 shows the ideal normalized output voltage and current waveforms of continuous class-BJ and class-F power amplifiers as the variable α is varied from -1 to 1 in 0.2 steps as well as the load trajectories with the same $R_{OPT}$ of 101.5Ω from the previous chapter. The class-F 3$^{rd}$ harmonic load remains in an open circuit condition while the trajectories of fundamental and 2$^{nd}$ harmonic loads move in opposite directions. At α=0 the voltage waveform returns to the conventional class-B and class-F output states. It is noted that the continuous mode voltage swings at α=-1 and α=1 are higher than the class-B and class-F states by almost a factor of 1.5 and 1.7 from α=0, respectively. The resulting normalized output power is maintained at 1 and the theoretical efficiencies for these limited harmonic cases are 78.5% and 90.7% for class-BJ and class-F, respectively throughout α values from -1 to 1 as shown in Fig. 6.2.
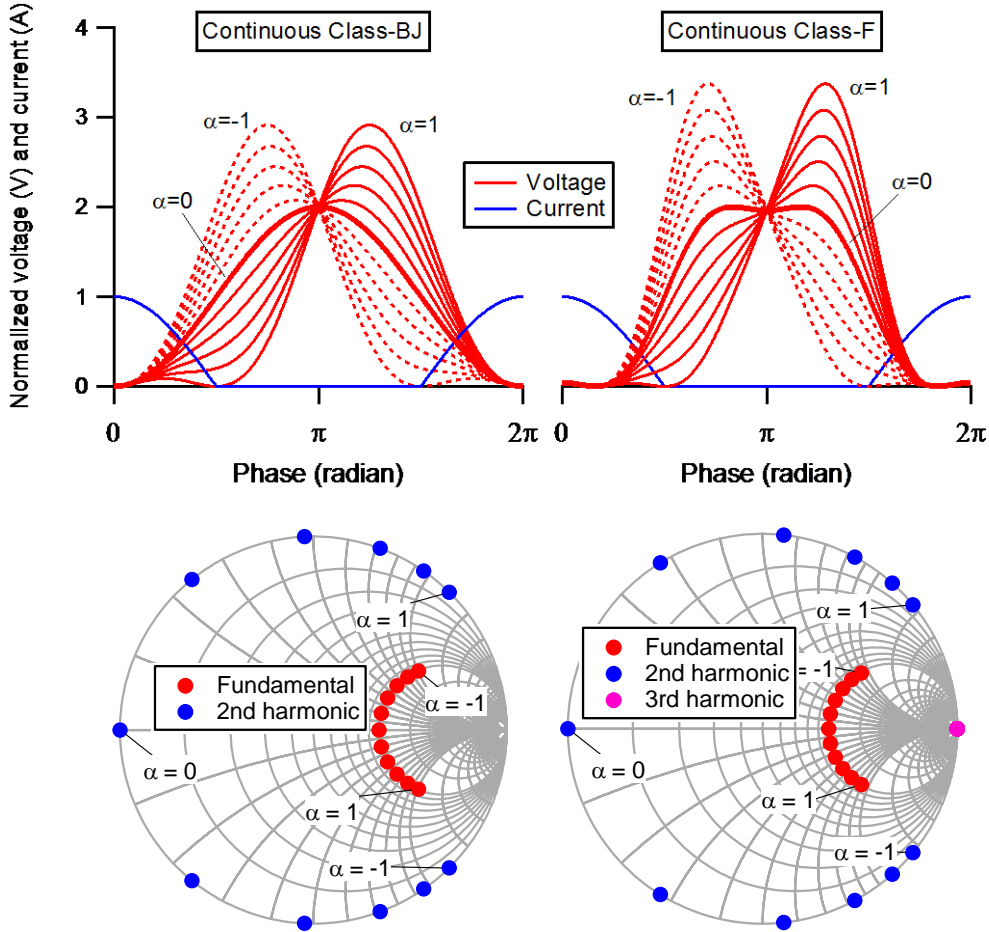
**Figure 6.1 – Voltage and current waveforms for continuous class-BJ and F for -1≤α≤1 in 0.2 steps (top), and the load trajectories with $R_{OPT}$=101.5Ω (bottom).**
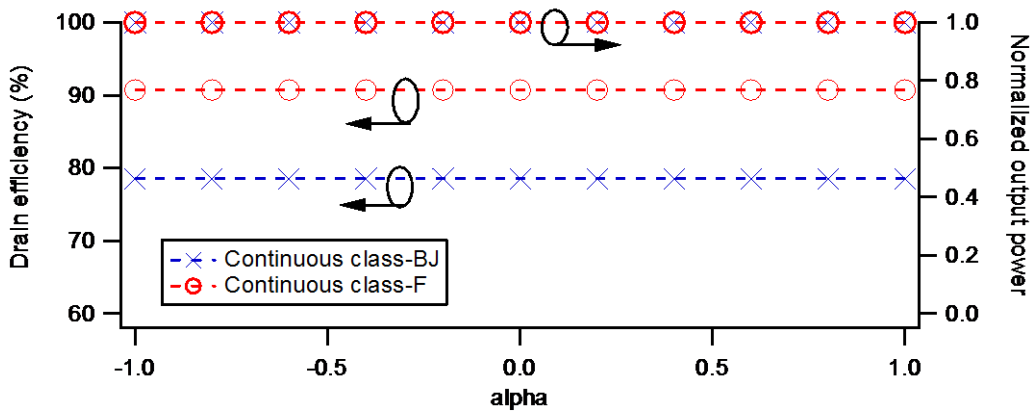


**Figure 6.2 - Efficiency and normalized output power for continuous class-BJ and class-F with up to 3 harmonic voltage components.**

The analysis in Chapter 3 was performed on a class-F mode, which is a subset of the continuous class-F mode with α=0. The work in this chapter further extends the investigation to include simulations and measurements at the full range of α values from -1 to 1 which translates into the full range of the continuous class-F mode. The continuous class-F mode analysis will be shown in 2 stages: at a single drain bias in Section 6.3, and in a variable drain bias setting in Section 6.4.

## 6.3 Investigating the Continuous Class-F Mode of an LDMOS Device at a Single Drain Bias

### 6.3.1 Characterisation Method: Continuous Class-F at 28V Bias

Using the active load-pull system and also Keysight ADS, the 10W LDMOS device from the previous chapter was initially setup to operate in class-F mode (α=0) at 28V drain bias with a fundamental load of 101.5Ω and driven to approximately 1dB into compression. The continuous class-F mode was then obtained by applying the fundamental and harmonic loads shown in Fig. 6.1 at the device current generator plane.

As for the input power level, there were 2 scenarios that were analysed; firstly a constant maximum drain current ($I_{MAX}$), and then with a constant input power ($P_{IN}$) at the gate terminal. For the first scenario, the input drive at each value of α was adjusted such that the measured peak drain current remained constant, which was the approach used in [1, 7]. The assumption is that the half-rectified current output waveform should remain constant as α is varied within the continuous mode range, therefore any fluctuation in current is due to the change in input power as a function of frequency, represented by α.

For comparison, in the second scenario (constant $P_{IN}$) the input drive level was adjusted such that the gate terminal was always presented with a constant input power after taking account of mismatch loss, as α was varied from -1 to 1. Hence this scenario does not compensate for the change in the drain current and provides an insight of the varactor effect of the device nonlinear $C_{DS}$ on continuous mode PA's. In a real circuit, this takes away the effect of frequency response of the input matching network and presents the gate with the intended constant power throughout the continuous mode range. This scenario is also relevant when it comes to the implementation of the ET shaping function, where a given input power is used to determine the required operating drain bias.

### 6.3.2    Results & Discussions: Continuous Class-F at 28V Bias

Fig. 6.3 shows the measured voltage and current waveforms of the continuous class-F mode at 28V drain bias. The reference state α=0 produced a waveform current maximum of 600mA corresponding to an input power of 11dBm at the gate terminal. Therefore these values are used for the constant-$I_{MAX}$ and constant-$P_{IN}$ scenarios, respectively.

Several observations are made from the voltage and current waveform measurements at 28V drain bias. Firstly for the constant $I_{MAX}$ scenario, even though the current waveform peak reached the desired value of 600mA for each value of α, the current waveform shape had changed considerably. Targeting a constant $I_{MAX}$ required a higher drive level on the positive α region as shown in Fig. 6.4. This is consistent with [7, 8], where the continuous mode was setup with its drive level adjusted to compensate for changes in the drain current.
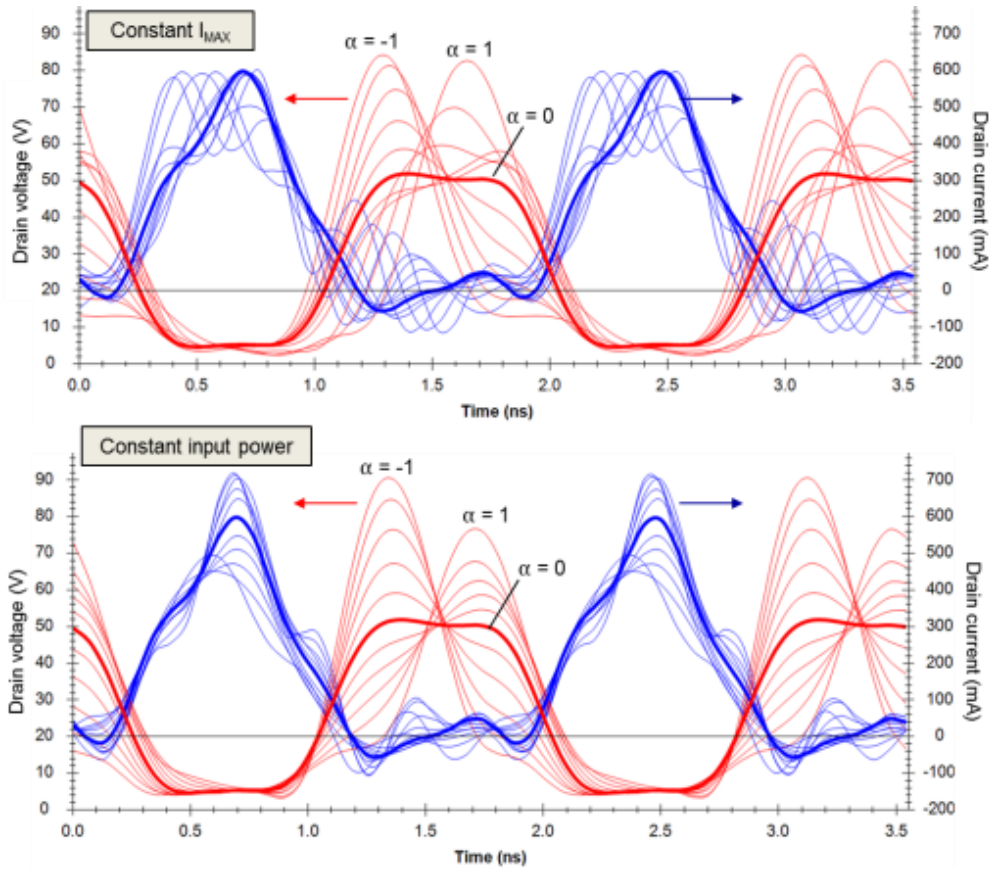
**Figure 6.3 – Measured voltage (red) and current (blue) waveforms of the continuous class-F for constant $I_{MAX}$ (top) and constant input power (bottom).**
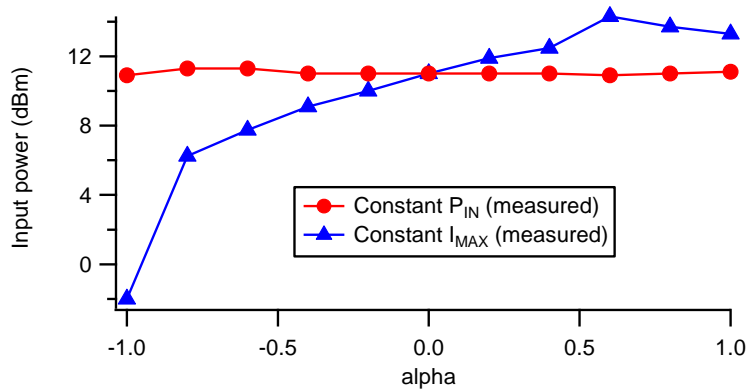


**Figure 6.4 - Measured input power for the 2 scenarios.**

The second observation is that the measured voltage waveforms in the positive α region have changed from the expected continuous class-F voltage waveform shape.  This was suspected to be caused by the nonlinear variation

of the device $C_{DS}$, or the varactor effect, where the displacement current changes the optimum fundamental and harmonic load locations from the theoretical trajectory shown in Fig 6.1. This phenomenon is further explored in Section 6.5.

If the input power at the gate was kept constant (scenario 2), the voltage waveforms that are closer to the expected shape were observed but the voltage swings at negative α values were bigger than those of positive α values. The peak drain current also increased at the negative α values compared to α=0 and positive α values. The increase and decrease of peak voltage and current waveforms are another suspected phenomenon attributed to the nonlinear $C_{DS}$.

The measured PAE and output power performance for the 2 scenarios are compared in Fig. 6.5 together with simulation results. In the case of constant $P_{IN}$, the efficiency and output power were relatively higher at α<0 values compared to α>0 with a difference of up to 12%-point and 2dB, respectively. The same trend was also observed in simulation with even a bigger delta: 25%-point difference in PAE and 3.4dB in output power. This is suspected to be another artefact of the nonlinear $C_{DS}$ effect which will be discussed further in Section 6.5.

By comparison the constant $I_{MAX}$ scenario showed a more consistent output power performance especially for α between -0.8 and 0.8. However its PAE performance behaviour trend was similar to the constant $P_{IN}$ scenario with the α<0 region generally exhibiting a higher PAE than those of α>0. For the

next analysis of continuous class-F in a variable drain setting, this constant $I_{MAX}$

scenario was used.
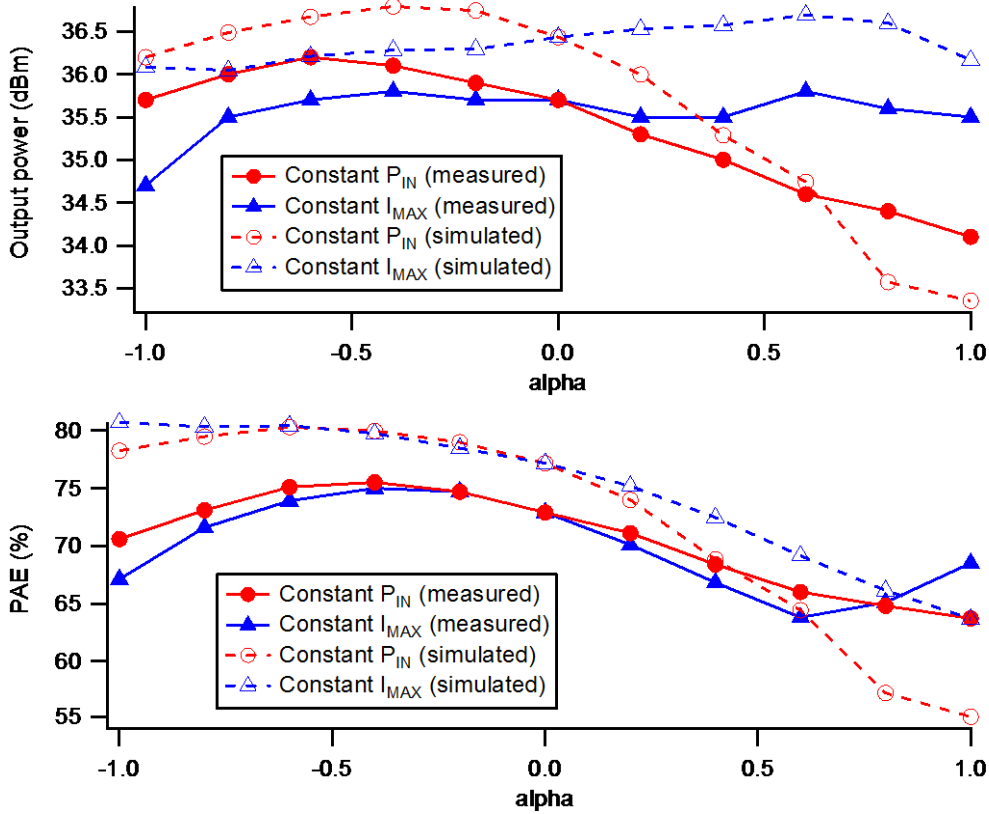


**Figure 6.5 - Measured and simulated PAE and output power for the 2 scenarios.**

## 6.4      Investigating the Continuous Class-F Mode of an LDMOS Device at a Variable Drain Setting

In an ET system, the drain bias is changed according to the shaping

function used, regardless of the input signal bandwidth.  Therefore, to observe

the behaviour of a continuous class-F PA in an ET environment, the previous

experiment is repeated over the full ET bias range, from 16V to 48V.

### 6.4.1     Characterisation Method: Continuous Class-F at ET Bias Range of 16V–48V

The same *flat-gain* shaping function from Chapter 3 was applied in this characterisation process at $\alpha=0$ to define the relationship between input power and drain bias. For each bias value, the $\alpha$ value was then varied between -1 to 1 in 0.2 steps while the drive level was adjusted to maintain a constant $I_{MAX}$. The constant $I_{MAX}$ normalizing method was selected for consistency reason with previous works in [1, 7]. Both simulation and load-pull measurements were performed under these settings at 900MHz. A fixed de-embedding approach was used for the $C_{DS}$ which corresponds to the 28V drain bias condition, making the 28V class-F mode the reference setting.

Additionally, the simulation was also performed at a significantly reduced frequency of 9MHz to remove the effect of $C_{DS}$ (and other parasitics), and to isolate its impact on device performance. According to the device model, the value of $C_{DS}$ at 28V bias is 1.3pF, which gives rise to a shunt reactance of 136Ω at 900MHz and 13.6kΩ at 9MHz. With a 101.5Ω load the $C_{DS}$ effect is therefore negligible at 9MHz.

### 6.4.2     Simulation and Measurement Results: Continuous Class-F in a Variable Drain Setting

The parameter of interest in this analysis is the efficiency performance as a function of $\alpha$ and drain voltage. Fig. 6.6 shows the PAE contour plot comparison between measurement and simulation as $\alpha$ was varied from -1 to 1 for each drain bias. The shaded areas in the plots indicate the condition where the target $I_{MAX}$ (obtained from $\alpha=0$ reference setting) was not achieved at these combinations of $\alpha$ and drain bias values. For comparison, the simulation at 9MHz represents a scenario of negligible $C_{DS}$ effect.

a) measured PAE
   at 900MHz
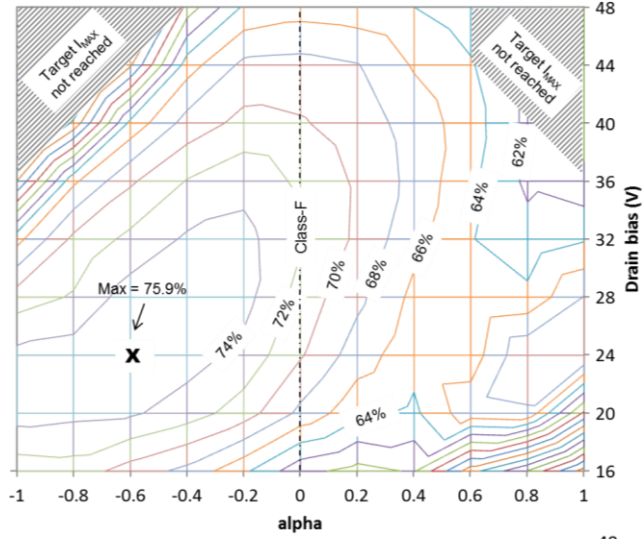
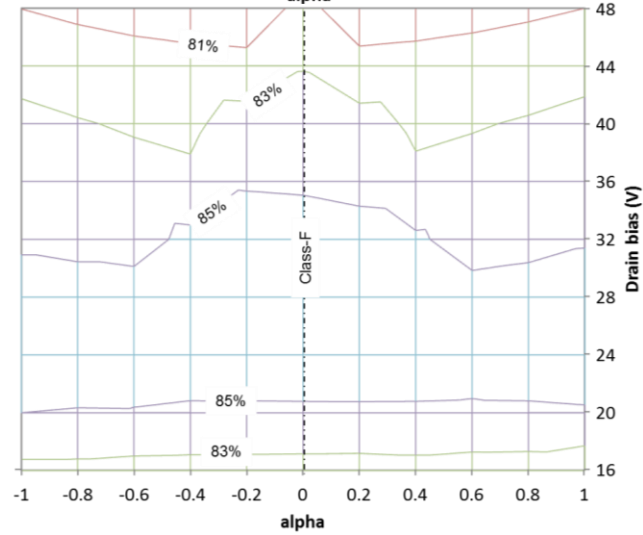b) simulated PAE
   at 900MHz
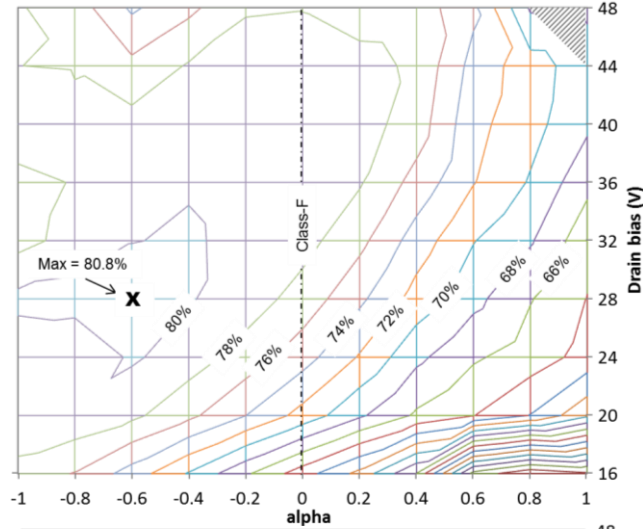
c) simulated PAE
   at 9MHz

**Figure 6.6 – PAE contour plots of the continuous class-F mode in a variable drain setting from load-pull measurement and simulations.**

At 900MHz, an almost diagonal plateau contour was observed from both measurement and simulation. Relative to the class-F 28V bias reference setting, the high-PAE region stretched towards the combination of low drain bias and negative α values as well as high drain bias and positive α values before degrading at extreme combinations of α and drain bias. The measured PAE peaked at α=-0.6 and 24V bias where it was approximately 5%-point higher than the class-F PAE. A similar trend was observed from simulation at 900MHz where the PAE peaked at α=-0.6 and 28V drain bias.

The simulation at 9MHz produced the expected almost-ideal outcome where only the drain bias variation affects the PAE performance while exhibiting a much less dependency on α. The slight PAE degradation with drain bias was a result of different optimum load requirements at different bias points whilst the device was terminated with a fixed 101.5Ω load.

### 6.4.3     Discussions

From the measured and simulated results of applying continuous class-F mode in a variable drain setting it was observed that there exists a region around α=-0.6 where the PAE performance was enhanced relative to the class-F (α=0) setting. This localized high-PAE region was not observed when the $C_{DS}$ effect is removed.

Importantly, for the 900MHz case where the $C_{DS}$ is active, the PAE was observed to degrade for positive α, and improve significantly in the negative α region, relative to the class-F (α=0) state. This phenomenon was caused by the nonlinear $C_{DS}$ property of the device and is mathematically analysed in the next section and experimentally validated in Chapter 7.

The measured PAE at 28V bias in the variable drain experiment in Section 6.4 had different performance characteristics compared to the single bias experiment in Section 6.3 due to a different selection of compression level at the α=0 reference setting. The single bias point experiment was conducted at 1dB gain compression at $V_{DS}$=28V whereas the variable drain bias experiment used a pre-defined shaping function which resulted in a 2dB compression level at 28V bias. It is therefore noted that the higher compression level causes a greater PAE enhancement at α=-0.6. One of the possible explanations is that at the higher compression level, the steep part of the $C_{DS}$ curve in the knee region is invoked, producing a higher displacement current magnitude.

The uncertain contribution of the displacement current at other α values poses an issue of using a constant $I_{MAX}$ as the normalizing method in a continuous mode PA characterisation. The other issue is that there are regions where the target $I_{MAX}$ is not achieved due to the superposition of displacement current from the nonlinear $C_{DS}$ which changes overall current waveform shape.

From the results, it was observed that the varactor effect on continuous class-F both improves and degrades the PAE. In addition, the required fundamental and harmonic load locations are modified, and the expected continuous class-F current (and as a consequence voltage) waveforms altered due to the contribution of displacement current, presenting a challenge in the characterisation process of a continuous mode PA from waveform engineering perspective. The next section presents a novel mathematical analysis of the

effect of the $C_{DS}$ variation, or the varactor effect, on continuous mode PA's, focusing on continuous class-BJ which is the most basic continuous mode.

## 6.5  A Novel Mathematical Analysis of the Varactor Effect on Continuous Mode Power Amplifiers

The ideal formulation of continuous class-BJ and class-F impedance trajectories shown in the previous section assumes a fixed $C_{DS}$.  In a real device however, the value of $C_{DS}$ changes nonlinearly with drain voltage, in a way that is specific to the device technology used.  Taking account of the nonlinear $C_{DS}$ to $V_{DS}$ relationship changes the impedance formulation for continuous modes, even at a single bias point.  This is not only because of the $C_{DS}$ variation during a drain voltage swing, but also the modification of the output voltage and hence the output capacitance, by the continuous mode operator α as it is varied from -1 to 1.  The variation in $C_{DS}$ changes the nature of the current delivered to the load, which then changes the effective load seen by the current generator plane.

This section aims to provide a mathematical explanation of the varactor effect on continuous mode power amplifiers, focusing on class-BJ power amplifier as it is the simplest form of continuous mode and involves only fundamental and 2nd harmonic load analysis.  The objective is to understand how the varactor and its displacement current change the fundamental and 2nd harmonic impedances seen by the current generator plane, when the output voltage adheres to the continuous class-BJ voltage definition.  The ultimate objective is to understand its impact on the device output power and drain efficiency.

### 6.5.1  Calculating the Varactor-Modified Impedance
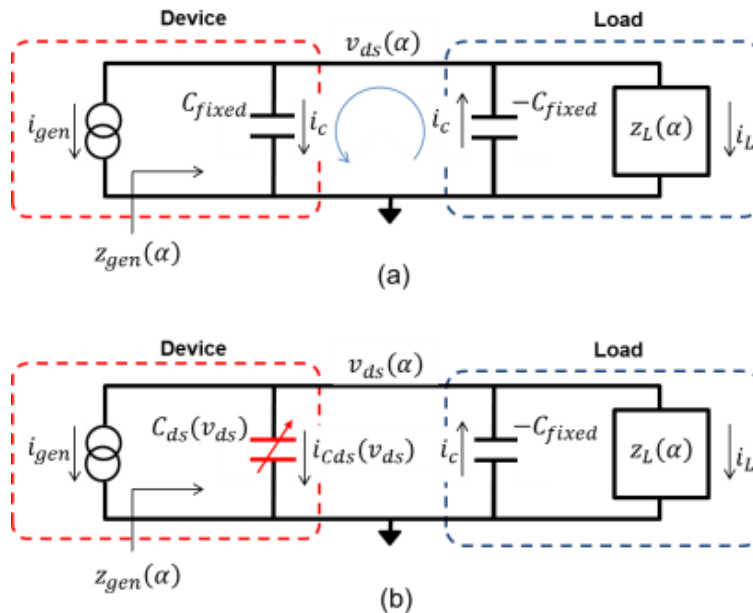


**Figure 6.7 - Simplified circuit diagram of the device with (a) an ideal, fixed output capacitance, and (b) a variable capacitance, connected to the load.**

Fig. 6.7 shows the equivalent circuit of a transistor operating in a continuous class-BJ mode, where the transistor is represented by a current generator in parallel with an output capacitor connected to a load. The top diagram illustrates an ideal scenario where the device output capacitance $C_{fixed}$ is of a fixed value regardless of the output voltage $v_{ds}(\alpha)$. The effect of this capacitor can be negated or *'resonated-out'* on the load side by an appropriate inductive load or in the case of waveform engineering and active load-pull, it can be de-embedded by adding a negative capacitance of the same value. In both cases the effect of the device output capacitance is cancelled out and the remaining current through the load ($Z_L$) is equal but opposite to that of the current generator.

With the output voltage strictly adhering to the continuous class-BJ definition, the output impedance seen by the current generator plane is given by (6.3) and the conventional continuous class-BJ fundamental and 2$^{nd}$ harmonic load trajectory from Fig. 6.1 is obtained:

$$Z_{gen}(\alpha) = -\frac{v_{ds}(\alpha)}{i_{gen}}$$

(6.3)

where $v_{ds}(\alpha)$ is the continuous class-BJ voltage as defined in (6.2).

In Fig. 6.7 (b) the ideal capacitor is now replaced with a variable capacitor, or varactor, whose value depends on the voltage across it. The static, de-embedding negative capacitor now does not completely cancel out the varactor current but rather it leaves a residual displacement current which is dependent on α. The current through the load is now given by:

$$i_L(\alpha) = -\left[i_{gen} + i_{Cds}(\alpha) - i_C\right]$$

$$= -i_{gen} + \frac{dv_{ds}(\alpha)}{dt}\left[C_{ds}(v_{ds}) - C_{fixed}\right]$$

(6.5)

With the output voltage constricted to the continuous class-BJ definition, the addition of this net variable current caused by the varactor modifies the fundamental and 2$^{nd}$ harmonic load impedances seen from the current generator plane. It is therefore important to know the C-V characteristic of the varactor in order to perform this mathematical analysis. The varactor's typical behaviour, which is dependent on the output voltage, can be modelled by the equation:

$$C_{ds}(v_{ds}) = C_{offset} + \frac{C_0}{\left(1 + v_{ds}/v_0\right)^m}$$

(6.6)

where $C_{offset}$, $C_0$, $v_0$, and $m$ are the adjustable parameters that describe the

shape of the C-V curve.   In Section 6.5.2 an approximation of the C-V

characteristics is shown using the parameters in (6.6) to match the

manufacturer's C-V model.   Applying (6.6) into (6.5) the load current can now

be expanded to:

$$i_L(\alpha) = -i_{gen} + \frac{dv_{ds}(\alpha)}{dt}\left[C_{offset} + \frac{C_0}{\left(1 + {v_{ds}}/{v_0}\right)^m} - C_{fixed}\right] \qquad (6.7)$$

Using FFT operation on the continuous class-BJ voltage described in

(6.1) and the current in (6.7), the resulting fundamental and 2nd harmonic

impedances seen by the current generator can be calculated.

### 6.5.2      Performing Numerical Analysis with Approximated Device Parameters

To proceed with this analysis a numerical approximation approach is

used as it simplifies the calculation and also provides a basis for comparison

with the simulation and measurement results.   The parameter values are

approximated and based on the device properties and the class-BJ operating

conditions (bias, output voltage and current swings).   The FFT operations,

calculations of the impedance, power, and drain efficiency are performed using

*Wavemetrics* Igor-Pro software.

| | |
|---|---|
| Maximum voltage magnitude ($V_{MAX}$) | 50V |
| Maximum current magnitude ($I_{MAX}$) | 0.8A (resulting in 10W output power) |
| Knee voltage | 0V |
| Conduction angle | 180° (Class-B bias) |
| Frequency | 1 GHz |

**Table 6.1 - Device settings and operating conditions used in the analysis.**

117

An approximation of the output capacitance behaviour as a function of drain voltage (C-V characteristic) is needed for this analysis. With the manufacturer's C-V model known, the parameters in (6.6) can be selected to produce a similar behaviour. Fig. 6.8 shows the values of these parameters in this mathematical analysis and how the approximated C-V curve compares to the manufacturer's model for this device.
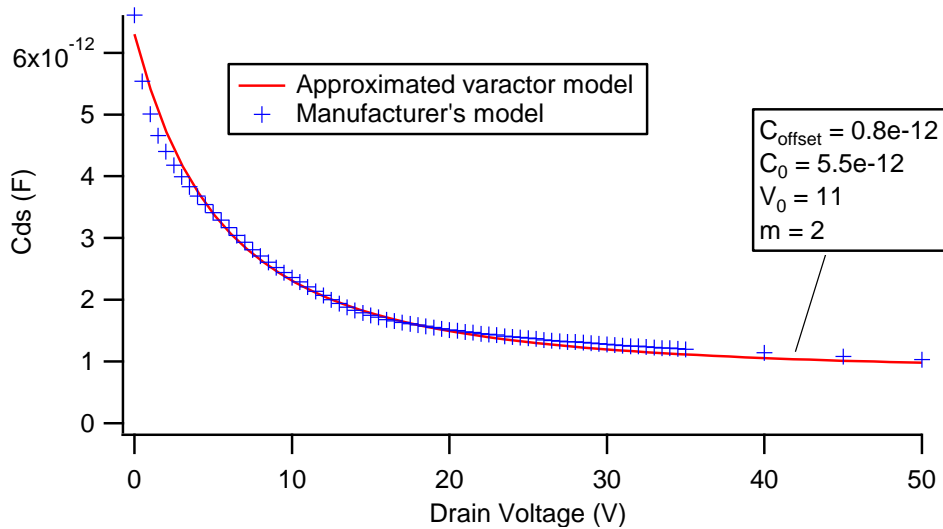


**Figure 6.8 - The C-V approximation used in this mathematical analysis and how it compares with the manufacturer's model.**

Applying the values from Table 6.1 and Fig. 6.8 into (6.1) and (6.7), the calculated time domain voltage and current are shown in Fig. 6.9. For this analysis the knee voltage effect is ignored. The displacement current generated by the varactor alters the ideal half-rectified current waveform even at $\alpha=0$. This is because the fixed de-embedding capacitor value used is not able to cancel out the nonlinear $C_{DS}$ throughout the voltage swing period.

Fig. 6.10 shows the calculated fundamental and 2nd harmonic load trajectories of continuous class-BJ mode for $-1\leq\alpha\leq1$ in 0.2 steps for the ideal case from Fig. 6.7 (a) and with the varactor of Fig. 6.7 (b).

118
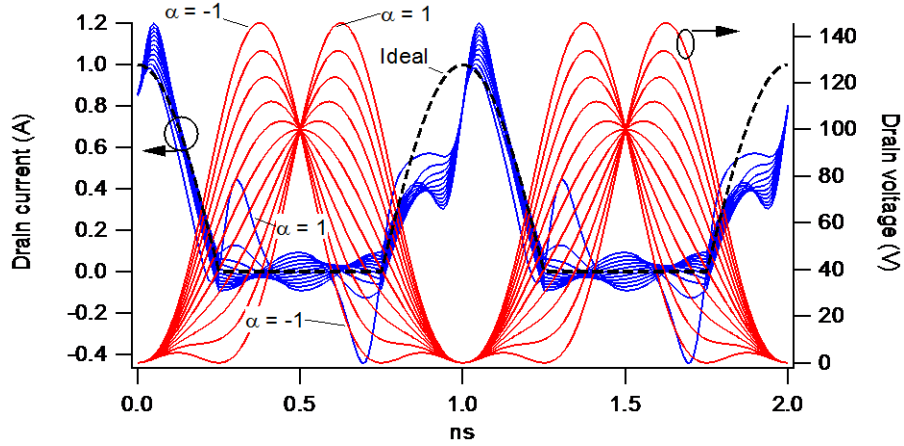
**Figure 6.9 – Calculated time domain voltage (red) and current (blue) waveforms.**
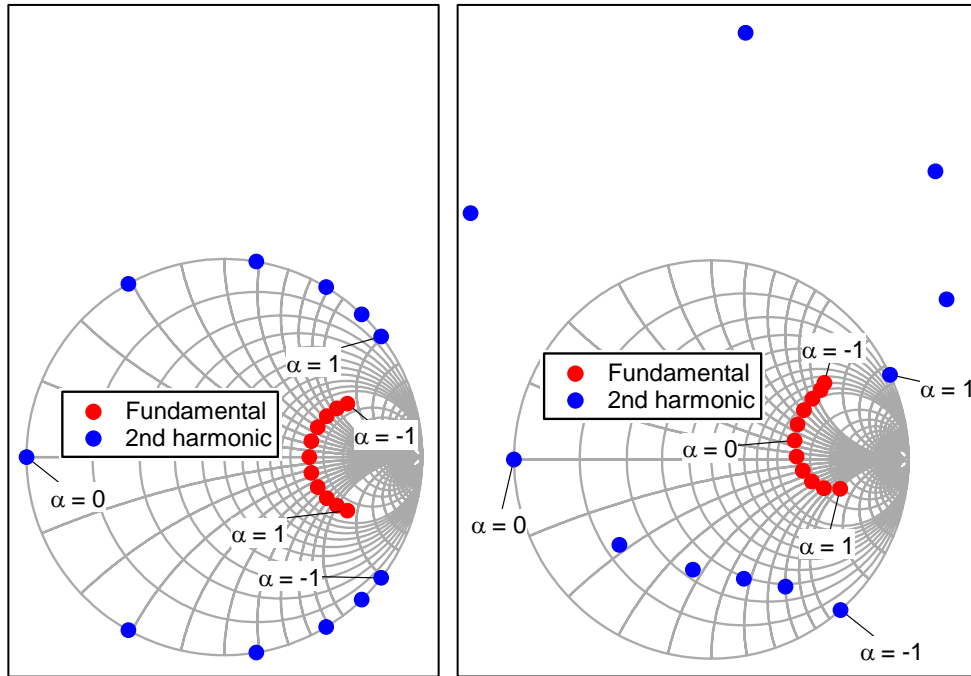


**Figure 6.10 – Calculated class-BJ fundamental and 2nd harmonic loads as a function of α for a fixed $C_{DS}$ (left) and a variable $C_{DS}$ (right).**

### 6.5.3    Observations and Discussions from the Mathematical Analysis

Fig. 6.10 indicates that with the varactor effect in place, the fundamental and 2nd harmonic load trajectories have been modified in order to maintain the established class-BJ output voltage waveforms with the varactor in effect. The calculated 2nd harmonic load trajectory goes inside the Smith

chart for $-1<\alpha<0$ indicating the presence of a resistive load requirement and consequential power dissipation, while for $0<\alpha<1$ the 2nd harmonic load appears outside the Smith chart indicating a varactor related 2nd harmonic 'injection' is taking place. It is worth noting that 2nd harmonic injection is an established way to improve PA efficiency [9-12].

Only at $\alpha=0$ is the original class-BJ 2nd harmonic load condition maintained, while at the extreme $\alpha$ values of -1 and 1, the 2nd harmonic load is located on the edge of the Smith chart, although with a phase offset from the ideal case. The trajectory of the fundamental load has also been slightly modified compared to its ideal class-BJ counterpart.

The modification of the load trajectories tallies with the calculated output power trend as a function of $\alpha$, for fundamental and 2nd harmonic as shown in Fig. 6.11. For $-1<\alpha<0$ as the 2nd harmonic load enters the Smith chart, the 2nd harmonic output power increases while the fundamental power drops by the same amount. This is an indication of an energy up-conversion where the energy at the fundamental frequency is transferred to the 2nd harmonic frequency. Subsequently the calculated drain efficiency, which depends on the fundamental power also drops compared to the ideal class-BJ efficiency for this range of $\alpha$, as shown in Fig. 6.11.

Conversely and importantly, for $0<\alpha<1$, where the 2nd harmonic load sits outside the Smith chart, energy down-conversion is observed where the 2nd harmonic energy is transferred to the fundamental frequency, causing the increase in fundamental power by the same amount as the drop in 2nd harmonic power. For this $\alpha$ range, an interesting observation is that the drain

efficiency has increased to approximately 85% compared to the ideal class-BJ

efficiency of 78.6%.  Therefore it can be concluded from this analysis that the

calculated impact of the varactor on fundamental output power in this example

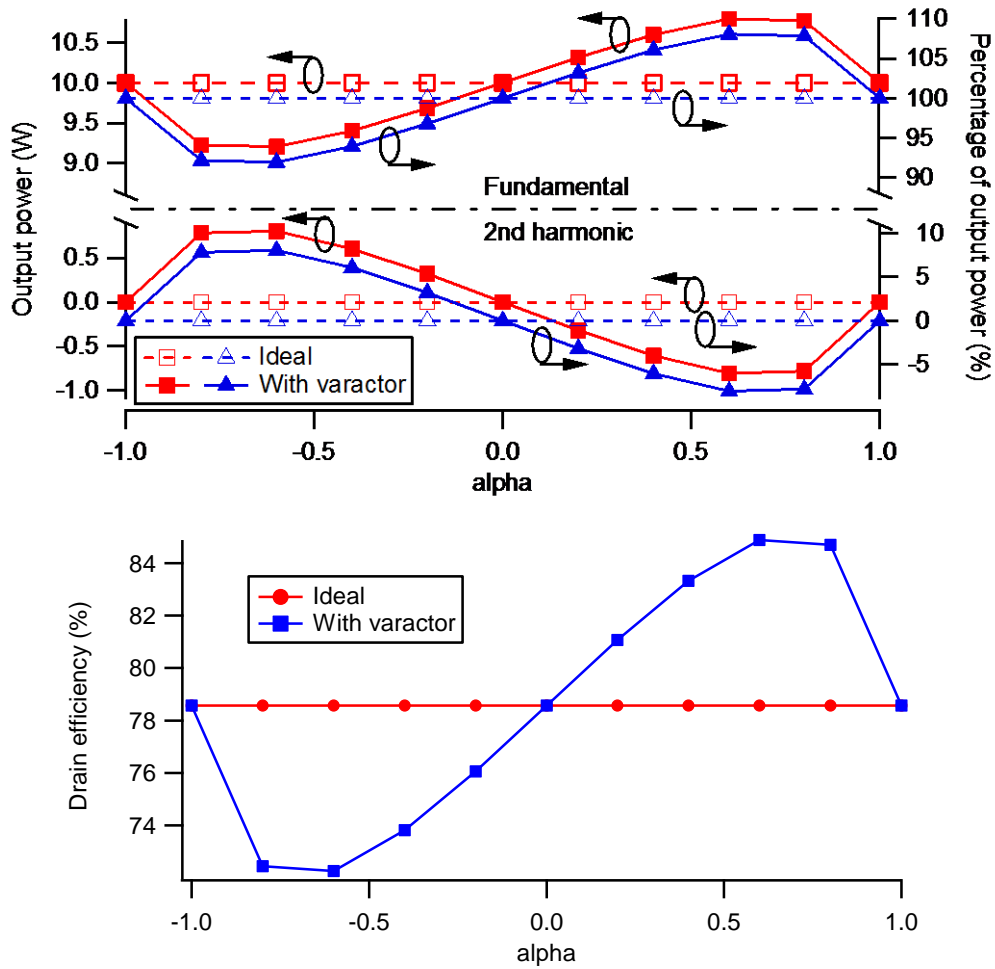is as much as ±8% and ±6.5% on drain efficiency, which is significant.



**Figure 6.11 - Calculated fundamental and 2nd harmonic power with and without varactor (top) and the resulting drain efficiency (bottom).**

At α=0, the 2nd harmonic power is zero even with the varactor in effect

since there is no 2nd harmonic voltage component.  As for the cases of α=-1

and 1, the calculated fundamental and 2nd harmonic power are also zero, just

as in the case of the ideal class-BJ.  This is because the phase of the 2nd

harmonic output voltage in these cases are 90 degrees out-of-phase from the

$2^{nd}$ harmonic current.  Since the power is the product of the voltage and current vectors, a 90-degree phase difference produces no $2^{nd}$ harmonic power and the power at fundamental is preserved.

### 6.5.4      Bringing the $2^{nd}$ Harmonic Load to the Edge of Smith Chart

The varactor causes the $2^{nd}$ harmonic load to shift inside and then outside the Smith chart for negative and positive α values, respectively in order to maintain the continuous class-BJ voltage at the output.  For the next step in this mathematical analysis, it is desirable to relocate these $2^{nd}$ harmonic loads to the edge of the Smith chart and there are 2 motivations for doing this.

Firstly, by pulling the $2^{nd}$ harmonic loads from outside the Smith chart (in the case of positive α range values) towards the edge, it becomes possible to achieve through passive network design.  Secondly, by pushing the $2^{nd}$ harmonic loads from inside the Smith chart towards the edge (in the case of negative α range values), a high-reflect is presented to the $2^{nd}$ harmonic frequency, preventing an energy up-conversion from the fundamental frequency hence improving efficiency.

The method used to bring the second harmonic loads towards the edge of the Smith chart is by applying a phase shift to the continuous class-BJ output voltage.  The equation (6.8) below describes the output voltage with the inclusion of a phase term, Φ.

$$v_{ds}(\alpha) = V_{max}(1 - cos(\theta + \varphi))(1 - \alpha\, sin(\theta + \varphi)) \qquad (6.8)$$

It is important to note that at α=1 and α=-1, no phase shift is needed since the $2^{nd}$ harmonic load for these cases are already located on the edge of the Smith chart.  As for α=0, it will be shown in the next section that a phase

shift is necessary to maintain the continuity of the fundamental load trajectory. Continuing from the example analysis from Section 6.5.2 above, an iterative search process is applied to the phase shift value Φ, such that the magnitude of the 2$^{nd}$ harmonic reflection coefficient is equal to 1 for all α other than α=-1, 0, or 1.  Fig. 6.12 shows the resulting phase shift required to bring the 2$^{nd}$ harmonic load to the edge of the Smith chart.    It is observed that by interpolation, the phase shift at α=0 is approximately -25°.  Even though the 2$^{nd}$ harmonic load at α=0 is already on the edge of the Smith chart, this phase shift is required to maintain continuity in the fundamental load trajectory.
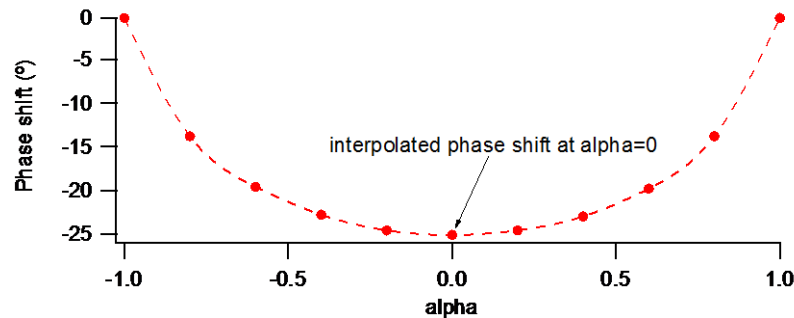


**Figure 6.12 – The required phase shift to bring the 2nd harmonic load to the edge of the Smith chart.**

Fig. 6.13 shows the resulting fundamental and 2$^{nd}$ harmonic load trajectories as a function of α after the phase shift is applied.  Note that the fundamental load at α=0 is now shifted from the real axis (ideal class-B load) as a result of applying the -25° phase shift to maintain the smoothness of the overall fundamental load trajectory.  The 2$^{nd}$ harmonic load at α=0 does not change since the 2$^{nd}$ harmonic voltage is shorted out.

The phase shifting counteracts the energy up-conversion and down-conversion phenomena from the varactor at negative and positive α,

respectively, keeping the calculated total output power at fundamental as α is varied from -1 to 1, as shown in Fig. 6.14.
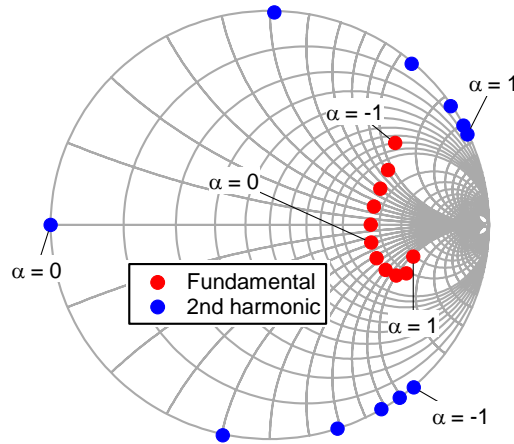


**Figure 6.13 - Fundamental and 2nd harmonic load trajectories after phase shifting.**
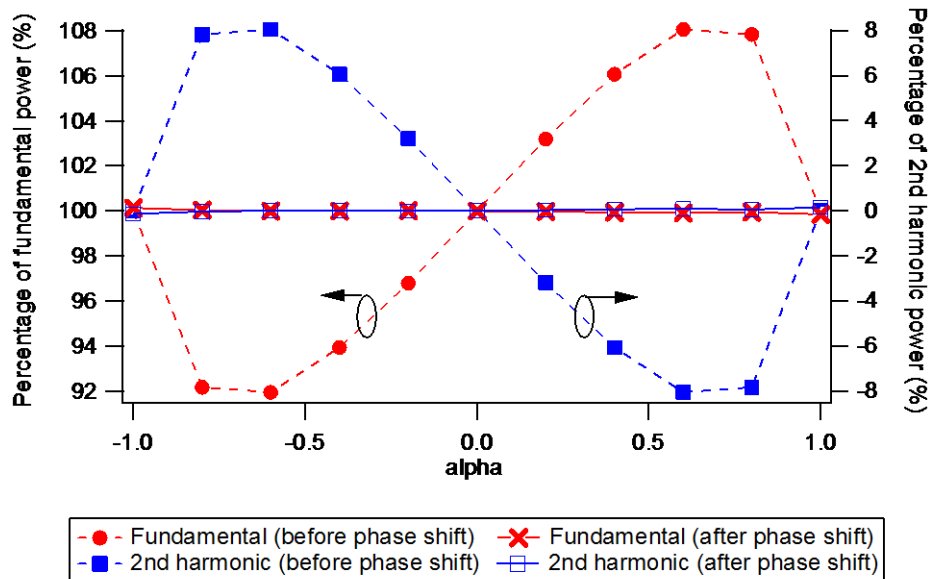


**Figure 6.14 - Output power distribution before and after phase shift.**

The phase shifting step consequently changes the calculated drain efficiency outcome, which results from the change in the fundamental output power as a function of α.  In the example above, applying phase shift shown in Fig. 6.12 results in the drain efficiency performance shown in Fig. 6.15.  As

expected at positive α values, the calculated efficiency drops since the 2nd harmonic injection effect from the varactor has been removed with the loads now relocated to the edge of the Smith chart.  At α=0, the efficiency drops from the ideal class-B number of 78.6% to 71% for this example, as the fundamental load has been shifted from the optimum location on the real axis of the Smith chart to cater for the overall load trajectory smoothness.
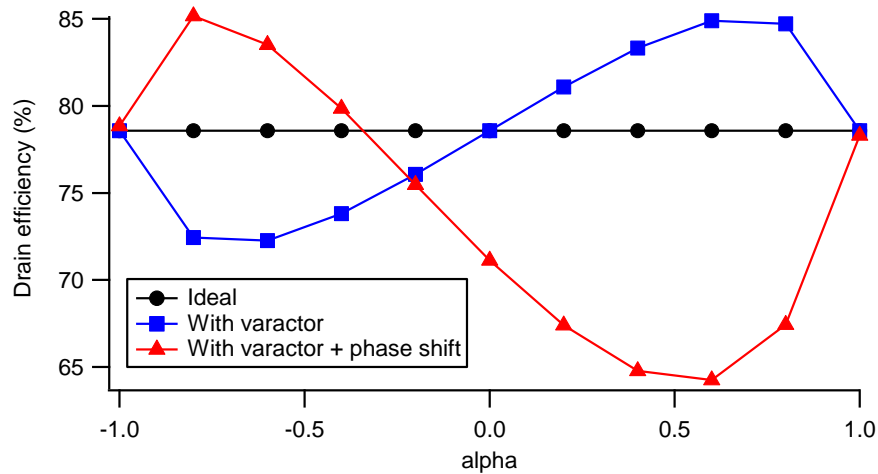


**Figure 6.15 - Drain efficiency before and after phase shift.**

However for α ≤ -0.4, the calculated drain efficiency is higher than the theoretical class-B efficiency number, since the varactor effect is now exploited to provide a 2nd harmonic injection effect within this range of α.  The highest drain efficiency achieved in this example is 85% when α=-0.8.  This presents an interesting proposition in the design of a class-BJ power amplifier, where the fundamental and 2nd harmonic now are all within the border of the Smith chart and a higher efficiency performance is possible to be achieved by exploiting the 2nd harmonic generating properties of the varactor.

### 6.5.5       Comparison with Previous 2nd Harmonic Injection Works

It is useful to revisit previous works where 2nd harmonic injection has been used for the same purpose and review their results as well as their methods of implementation.

The proof-of-concept of efficiency enhancement using 2nd harmonic injection is presented in [9] where an additional source is directly connected at the input to inject a 2nd harmonic signal. By adjusting the externally injected 2nd harmonic power, the PAE can be improved by 15% for a 4W GaN HEMT operating in a class-B mode at 2GHz. In [10] a source pull approach is used to inject the 2nd harmonic to shape the input waveform, enhancing the PAE of a pHEMT operating in class-B by 5.9% at 9GHz. In [11] the 2nd harmonic injection is obtained through a feedback loop with an added auxiliary class-E mode amplifier, enhancing the main amplifier PAE by 16%-point. An auxiliary PA is also used in [12] to inject a 2nd harmonic into a main PA operating in inverse class-F mode at 1GHz. For this particular example the improvement was not in terms of a higher PAE but in terms of the extended bandwidth of the high-efficiency (>80%) region, going from 60MHz to 180MHz.

However in these previous works an external circuit is required to supply the 2nd harmonic signal. The mathematical analysis in this chapter suggests that the varactor itself can be exploited to generate the 2nd harmonic injection to improve PA efficiency. In the next chapter the experimental investigation is performed to explore this possibility.

## 6.6　　Conclusions

The first part of this chapter presents the novel experimental work of integrating continuous class-F mode in an envelope tracking environment using waveform engineering approach. The observations made from the measurement results suggested that the varactor positively and negatively affects the drain efficiency performance of a continuous mode PA even at a single drain bias. This observation led to a deeper investigation of the varactor effect on continuous mode PA's to explain the measurement results.

The second part of this chapter presented the theory of the varactor effect on continuous mode PA's, focusing on the most basic continuous mode which is class-BJ. It can be shown mathematically that the varactor improves the drain efficiency performance on half of the continuous mode design space while it degrades the other half, relative to the class-B reference mode. The mechanism behind the efficiency performance change is the energy conversion between fundamental and $2^{nd}$ harmonic. In the case where efficiency is enhanced, the varactor acts as a $2^{nd}$ harmonic injection source, similar to the concept discussed in [9-12]. It is worth noting that the efficiency improvement amount will also depend on the $C_{DS}$-$V_{DS}$ characteristics.

The next chapter presents an experimental work to validate the theory of efficiency enhancement through the varactor alone, and discusses its limitations.

## 6.7　　References

[1]　　S. C. Cripps, P. J. Tasker, A. L. Clarke, J. Lees, and J. Benedikt, "On the Continuity of High Efficiency Modes in Linear RF Power Amplifiers," *Microwave and Wireless Components Letters, IEEE,* vol. 19, pp. 665-667, 2009.

[2] V. Carrubba, A. L. Clarke, M. Akmal, J. Lees, J. Benedikt, P. J. Tasker*, et al.*, "The Continuous Class-F Mode Power Amplifier," in *Microwave Conference (EuMC), 2010 European*, 2010, pp. 1674-1677.

[3] V. Carrubba, J. Lees, J. Benedikt, P. J. Tasker, and S. C. Cripps, "A novel highly efficient broadband continuous class-F RFPA delivering 74% average efficiency for an octave bandwidth," in *Microwave Symposium Digest (MTT), 2011 IEEE MTT-S International*, 2011, pp. 1-4.

[4] E. McCune, *Dynamic Power Supply Transmitters*: Cambridge University Press, 2015.

[5] B. Merrick and T. J. Brazil, "Analysis of the integration of envelope tracking with Continuous Class F amplifiers," in *Integrated Nonlinear Microwave and Millimetre-Wave Circuits (INMMIC), 2012 Workshop on*, 2012, pp. 1-3.

[6] P. Colantonio, F. Giannini, G. Leuzzi, and E. Limiti, "On the class-F power amplifier design," *International Journal of Rf and Microwave Computer-Aided Engineering,* vol. 9, pp. 129-149, Mar 1999.

[7] V. Carrubba, "Novel highly efficient broadband continuous power amplifier modes," PhD Thesis, Cardiff University, 2012.

[8] V. Carrubba, A. L. Clarke, M. Akmal, Z. Yusoff, J. Lees, J. Benedikt*, et al.*, "Exploring the design space for broadband PA's using the novel continuous inverse class-F mode," in *Microwave Conference (EuMC), 2011 41st European*, 2011, pp. 333-336.

[9] H. Matsubara, F. Kawanabe, and T. Nojima, "A 2-GHz band experiment on efficiency enhancement of a GaN power amplifier using 2nd harmonic injection," in *Microwave Conference, 2008. APMC 2008. Asia-Pacific*, 2008, pp. 1-4.

[10] M. Haynes, S. C. Cripps, J. Benedikt, and P. J. Tasker, "PAE improvement using 2nd harmonic source injection at X-band," in *Integrated Nonlinear Microwave and Millimetre-Wave Circuits (INMMIC), 2012 Workshop on*, 2012, pp. 1-3.

[11] H. R. Bae, C. S. Cho, and J. W. Lee, "Efficiency enhanced class-E power amplifier using the second harmonic injection at the feedback loop," in *Microwave Conference (EuMC), 2010 European*, 2010, pp. 1042-1045.

[12] M. Seo, H. Lee, J. Gu, H. Kim, J. Ham, W. Choi*, et al.*, "High-Efficiency Power Amplifier Using an Active Second-Harmonic Injection Technique Under Optimized Third-Harmonic Termination," *IEEE Transactions on Circuits and Systems II: Express Briefs,* vol. 61, pp. 549-553, 2014.

# Chapter 7

# Exposing the Varactor Effect in Measurement – The Voltage-Pull Method

## 7.1    Introduction

In the previous chapter, the varactor effect on continuous mode PA performance has been mathematically analysed.  The concept of exploiting the varactor for efficiency improvement has also been proposed using a phase shifting technique that is theoretically applied to the output voltage.

This chapter presents an experimental investigation of the varactor effect to validate the theory proposed in Chapter 6 and to investigate the feasibility of exploiting the varactor for PA efficiency improvement.  A novel measurement method to expose the varactor effect on continuous mode PA's, termed the *voltage-pull* is presented.  This method is a modification of the traditional active load-pull approach with the difference that it uses the output voltage waveform as the target criteria rather than specific fundamental and harmonic loads on the Smith chart.

The voltage-pull method was applied both in simulation and in measurement, to a 50V LDMOS device operating in a continuous class-BJ

mode. The resulting impedance trajectories, output power, and efficiency were then analysed and compared to the outcomes from the mathematical analysis.

The possibility of exploiting the varactor for efficiency improvement was then explored using the phase shifting technique on the class-BJ voltage waveform. The chapter concludes with a discussion on the limitations of efficiency enhancement using the varactor due to its resistive loss, and mathematically analyses the lossy-varactor effect in comparison with the theory presented in Chapter 6.

## 7.2     Load-Pull Approach vs. Voltage-Pull Approach

The approach to conventional active load-pull uses the concept of a target load and an algorithm to iteratively change the magnitude and phase of a synthesized phase coherent signal at the load in order to converge onto the target. For waveform engineering and specifically continuous mode PA characterisation, this method relies on de-embedding accuracy to correctly establish the continuous mode output voltage and current waveforms at the intrinsic device plane, from the defined loads. However as shown in Chapter 6, a static de-embedding approach will not be able to fully compensate for the dynamic displacement current generated by the nonlinear $C_{DS}$.

Characterizing a continuous class-BJ mode for example, by applying a target load based on the continuous mode formulation from Fig. 6.1 will result in an output voltage that is different from the expected class-BJ waveforms in Fig. 6.1 because of the varactor displacement current.

To understand and observe the varactor effect on continuous mode operation, a different measurement approach is required where the desired

continuous mode output voltage waveform itself is set as the target at the device's output. This is the approach used in the newly introduced voltage-pull method, where a voltage source is connected at the load to force the output voltage according to the theoretical continuous mode voltage formulation. Fig. 7.1 shows the implementation of the voltage-pull method on a class-BJ mode compared to the conventional load-pull method.
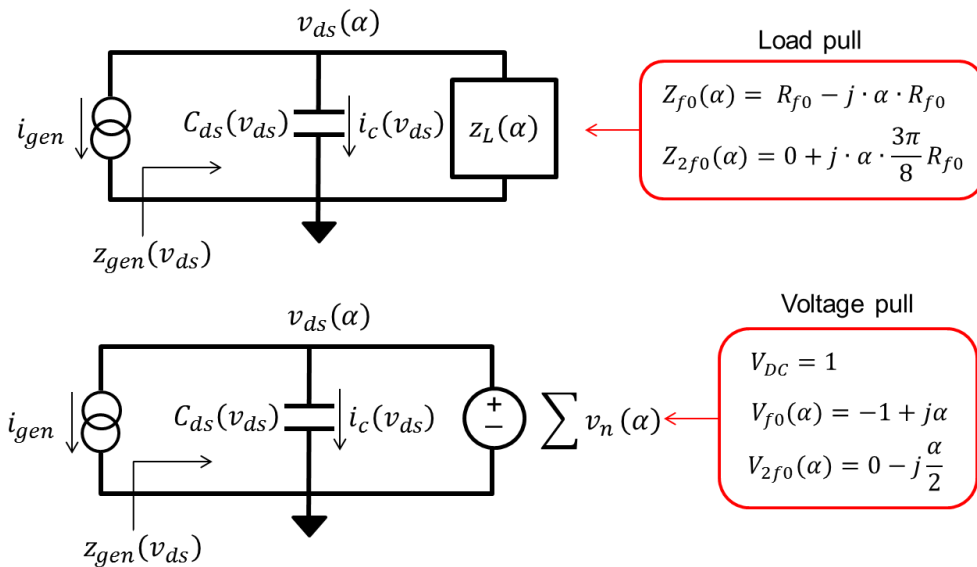


**Figure 7.1 - Comparison of load-pull approach (top) and voltage-pull (bottom).**

The voltage-pull method enables the analysis of the fundamental and harmonic impedances seen by the current generator plane during a continuous mode operation, when the output capacitance is de-embedded with a fixed reference value. With the output power and efficiency known, this method also enables the investigation of the energy transfer between fundamental and 2nd harmonic, for the case of class-BJ mode. The subsequent section discusses the simulation of the voltage-pull method.

## 7.3      Simulation of the Varactor Effect on Continuous Class-BJ Power Amplifier Using Voltage-Pull

The voltage-pull method can be simulated in Keysight ADS software where a voltage source is used to force the continuous mode voltage at the device output.  This section demonstrates in simulation the voltage-pull method performed on a 50V LDMOS device operating in class-BJ mode at 900MHz.

### 7.3.1      Setting up the Voltage-Pull Simulation: Class-BJ Mode, 48V Drain Bias, Optimum Load = 150Ω

The same device model from chapter 3 was used in this simulation, where the die model inherently contains the device nonlinear $C_{DS}$ as shown in Fig. 6.8.  The device was drain-biased at 48V to get maximum output power and so that the energy conversion between fundamental and 2$^{nd}$ harmonic was more visible.  The 150Ω $R_{OPT}$ was used in this section since it is the optimum load for efficiency at 48V bias.  A fixed $C_{DS}$ de-embedding value was used to access the current generator plane when the continuous mode variable α is set to zero.  This provides a reference setting that was used in quantifying the effect of the varactor as α was varied from -1 to 1.  The details of the simulation setup are discussed in Appendix D.

### 7.3.2      Simulation Results & Discussions

Fig. 7.2 shows the resulting fundamental and 2$^{nd}$ harmonic load trajectory on the Smith Chart as α was varied from -1 to 1.  For the reference setting α=0, the expected class-B loads were obtained.  However for negative α values, the 2$^{nd}$ harmonic loads were located inside the Smith Chart and for positive α values they were located outside the Smith Chart.  This result matched the mathematical analysis of the varactor effect explained in Chapter

6.  The main difference now was that for α= -1 and α= 1 the 2$^{nd}$ harmonic load did not return to the edge of the Smith Chart.  The exact reason is unknown but it is suspected that the manufacturer model incorporates some lossy element at the drain.
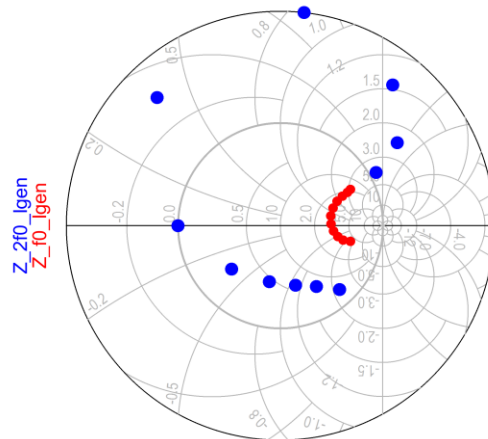


**Figure 7.2 - Simulated fundamental and 2$^{nd}$ harmonic load trajectories for  -1≤α≤1 using voltage-pull.**

The resulting current and voltage waveforms are shown in Fig. 7.3. With voltage-pull, the nonlinear variation in $C_{DS}$ with α manifested itself as a change in the displacement current, and since a static de-embedding was used, the drain current magnitude varied with α.  The resulting waveforms were very similar to the waveforms obtained from the mathematical analysis (Fig. 6.9).

Fig 7.4 shows the change in fundamental and 2$^{nd}$ harmonic absolute power level (a) and in percentage (b) from simulation, as α is varied, which confirms the theory discussed in Chapter 6.  In the negative α region the energy at the fundamental was up-converted to 2$^{nd}$ harmonic while at positive α region the 2$^{nd}$ harmonic energy was down-converted to fundamental.
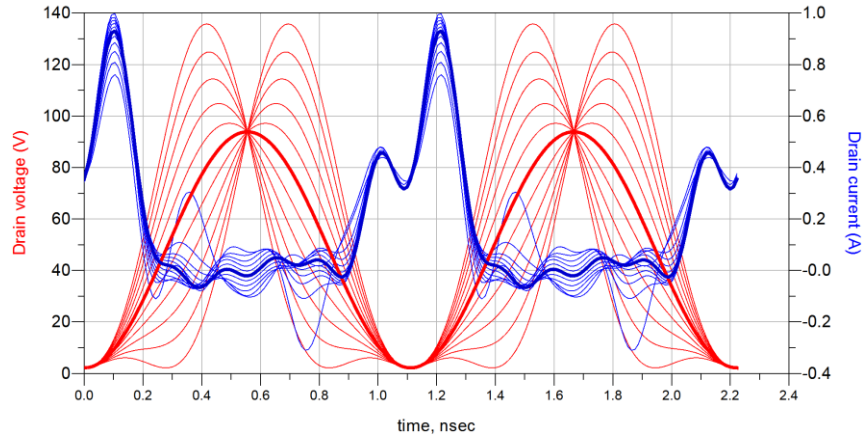
**Figure 7.3 – Simulated voltage and current waveforms for -1≤α≤1 in 0.2 steps using voltage-pull.**
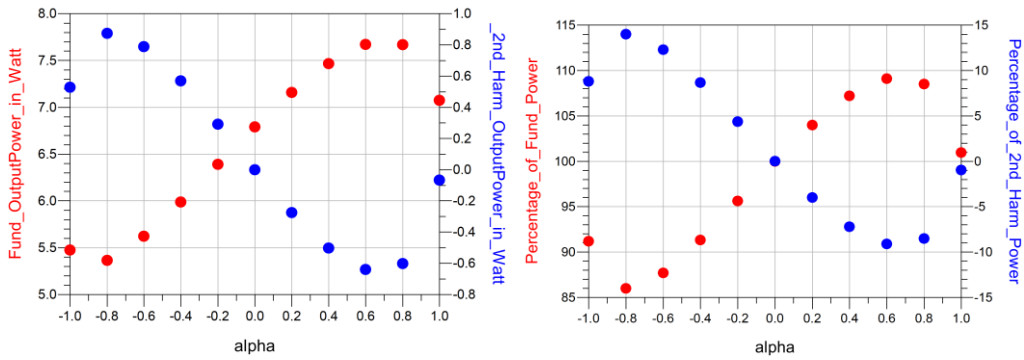


**Figure 7.4 – Simulated output power and distribution for fundamental (red) and 2$^{nd}$ harmonic (blue) as a function of α.**
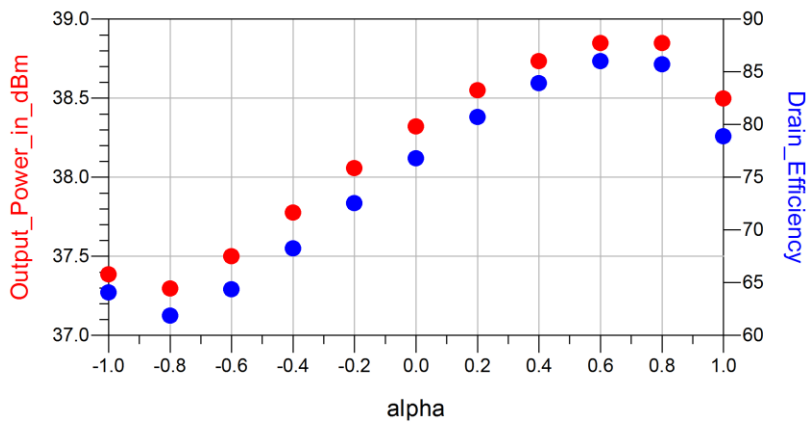


**Figure 7.5 – Output power and drain efficiency as function of α.**

The output power and drain efficiency as a function of α are shown in Fig. 7.5.  As a result of the energy up-conversion in the negative α region, the device output power and efficiency dropped in performance compared to the reference class-B (α=0) case by as much as 15%.  In contrast, the output power and efficiency improved by as much as 10% in the positive α region as the energy from the 2$^{nd}$ harmonic was injected and down-converted to fundamental, as predicted from the mathematical analysis.

### 7.3.3      Simulating an Applied Phase Shift on the Output Voltage

The next step was to simulate the necessary phase shift on the output voltage at each α value to bring the 2$^{nd}$ harmonic loads to the edge of the Smith chart, as performed in the mathematical analysis in Chapter 6.  In this example simulation, the required phase shift for each α was manually obtained using the ADS Tuning function.

Fig. 7.6 shows the phase shift values that were applied and the modified fundamental and 2$^{nd}$ harmonic load trajectories, which agreed with the trajectories predicted from the mathematical analysis in Fig. 6.13.

The resulting output power from simulation after phase shift was applied is shown in Fig. 7.7.  It is observed that the energy conversion from the varactor was not as large as the one from the mathematical analysis.  This is because this simulation took into account the device knee voltage and this also reduced the $C_{DS}$ variation.
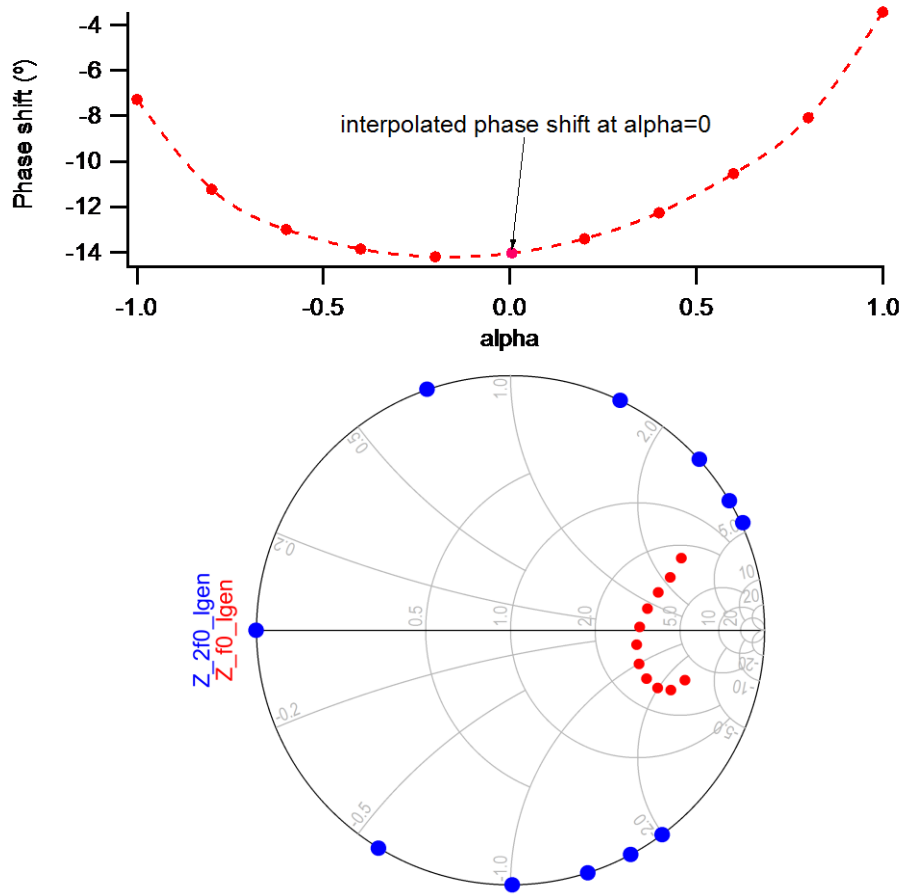
**Figure 7.6 - Required phase shift obtained manually from the ADS Tuning function (top) and the resulting modified load trajectories (bottom).**
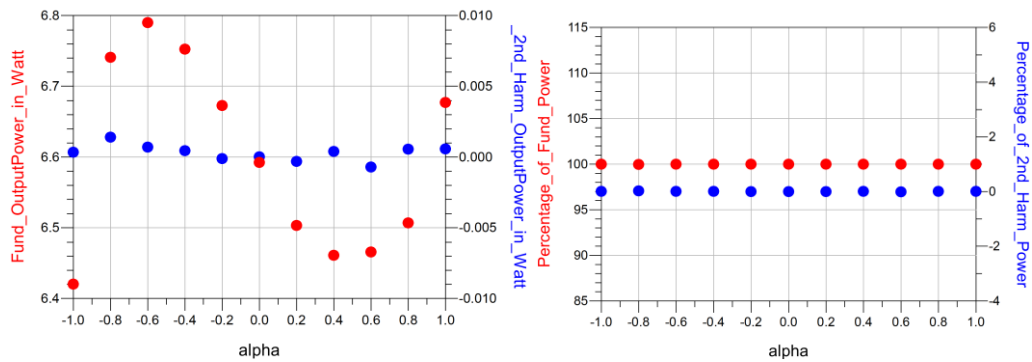


**Figure 7.7 - Simulated output power with phase shift applied.**

The simulated output power and drain efficiency comparison before and after applying phase shift are shown in Fig. 7.8. The efficiency in the positive α region decreased as the 2$^{nd}$ harmonic injection effect was removed when the

2nd harmonic loads were no longer outside the Smith chart. The efficiency at α=0 degraded by 2% as a result of the phase shift that was applied to maintain a smooth fundamental load trajectory on the Smith chart. In the negative α region the efficiency improved after phase shift and was higher than the efficiency at α=0 overall since the 2nd harmonic power was down-converted to the fundamental frequency due to the high reflection it was presented with at the output.
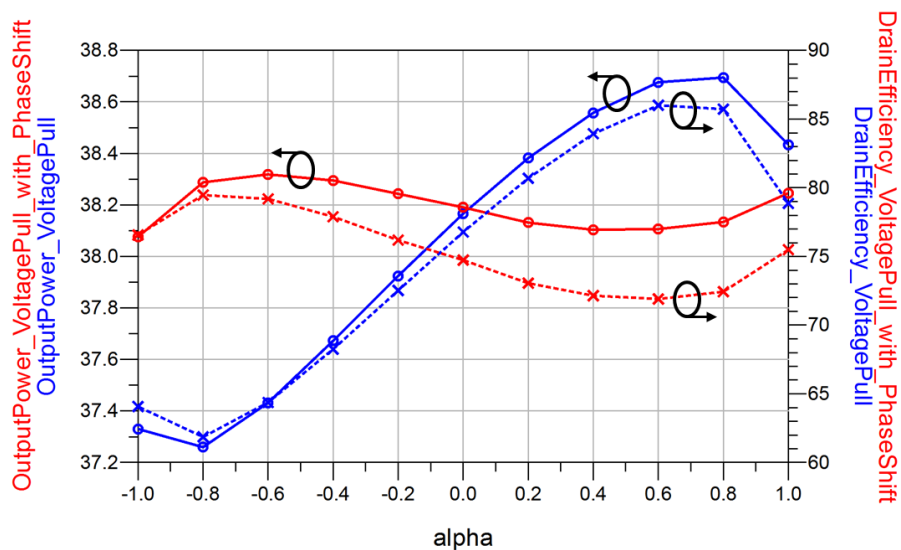


**Figure 7.8 - Simulated output power and drain efficiency before (blue) and after phase shift applied (red).**

## 7.4    Experimental Setup to Analyse the Varactor Effect on Continuous Class-BJ Using Voltage-Pull

The next step was to implement the voltage-pull method on an actual device operating in class-BJ mode. Similar to the previous experiments performed in Chapter 3, the device under test was a packaged 50V LDMOS device. An iterative algorithm was used in the implementation of the voltage-pull approach as described in the next section.

### 7.4.1      **Voltage-Pull Experimental Setup**

The same active load-pull system was used in this experiment but instead of executing the usual load-pull characterisation, the waveform engineering system was now configured to run voltage-pull instead. The device was biased in continuous class-BJ mode at 900MHz near the maximum drain bias point of 48V to enable a more visible energy transfer between fundamental and $2^{nd}$ harmonic. The fundamental load that produced maximum efficiency at 48V bias (150Ω) was selected so that any further increase in efficiency can be attributed to the varactor's $2^{nd}$ harmonic energy down-conversion. A class-B mode ($\alpha=0$ state) was used as a reference state for the rest of the $\alpha$ values. The drive level at each $\alpha$ was adjusted to maintain a constant DC current as the class-B state.

### 7.4.2      **Implementing Voltage-Pull Method Using an Active Load-Pull System**

The Mesuro active load-pull system at Cardiff University uses a load search algorithm, targeting loads instead of voltage waveforms. The fundamental and harmonic loads are synthesized based on the measured incident and reflected waves using external signal generators. Since it is an active load-pull system, it is able to synthesize negative loads, which allows for this varactor analysis. However, the Mesuro system is unable to perform voltage-pull directly on its own. In order to use this system for voltage-pull, additional steps are needed to report the loads that correspond to the desired voltage waveforms, and for this work the ADS software was used to provide this function, as shown in Fig. 7.9.
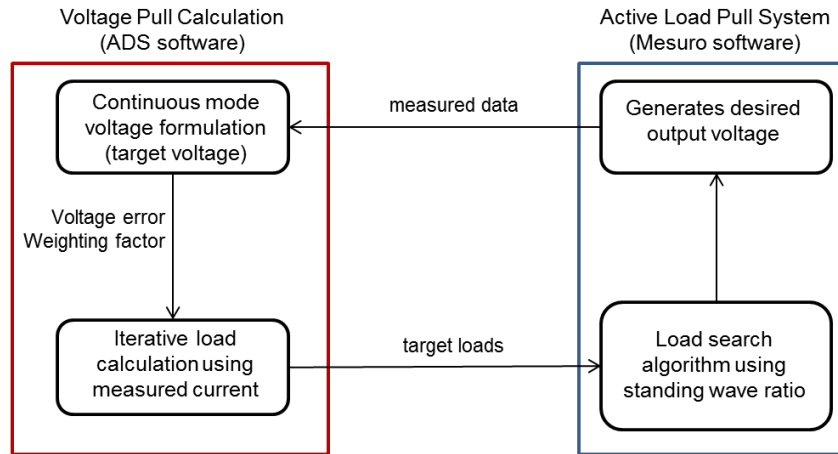
**Figure 7.9 – Implementing voltage-pull using an active load-pull system**

A new program to iteratively calculate the target loads to produce the formulated continuous class-BJ was developed using ADS software utilising its Data Display capability. The reason ADS Data Display was chosen instead of other applications is because it can directly import measured load-pull data for post load-pull processing. The program was then used to iteratively calculate the target loads that correspond to the required voltage states, and feed them into the active load-pull system. Fig. 7.10 shows the flow of the voltage-pull algorithm implemented within the ADS Data Display window.

The first step of the process was the establishment of a class-B mode (α=0) using the active load-pull system. The measured voltage and current information was then extracted and the waveforms were phase-aligned by stripping off the phase of the current so that its phase was zero. The *target voltage* in this case was the ideal continuous class-BJ voltage for each α and can be derived using the magnitude of the measured fundamental voltage as shown in equations (7.1) and (7.2).
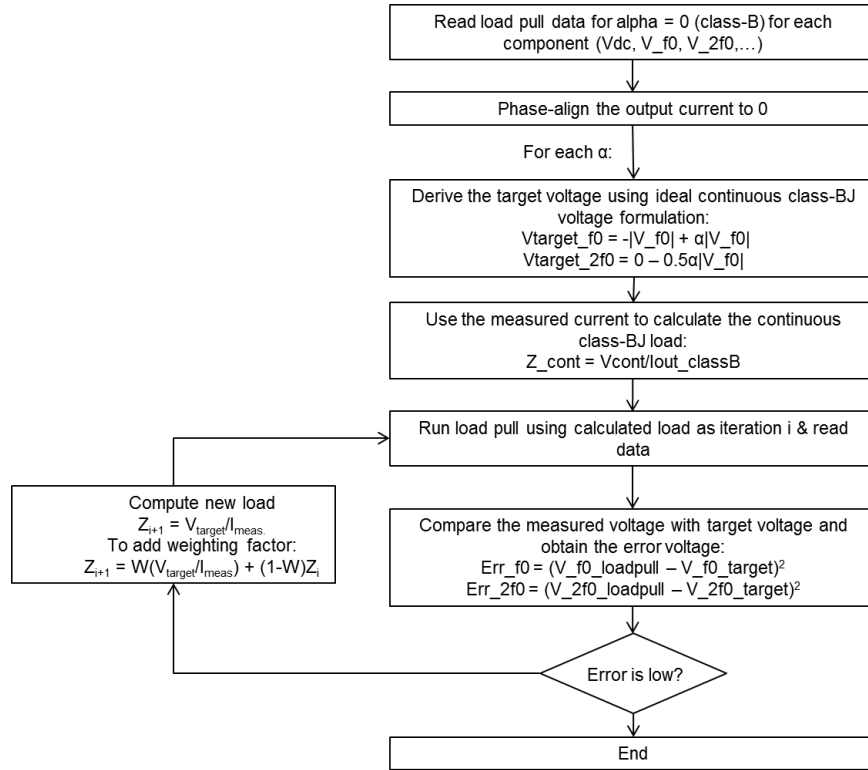
**Figure 7.10 – Voltage pull algorithm flow**

$$V_{target\_f0} = V_{BJ\_f0} = -|V_{f0}| + j\alpha|V_{f0}| \qquad (7.1)$$

$$V_{target\_2f0} = V_{BJ\_2f0} = 0 - j\frac{1}{2}\alpha|V_{f0}| \qquad (7.2)$$

Using the measured current, the target load for each frequency component can be calculated using the equation:

$$Z_{target} = \frac{V_{targt}}{I_{measured}} \qquad (7.3)$$

The calculated fundamental and harmonic loads for each α were then fed into the active load-pull system, which used external signal generators to produce the next iteration of voltage waveform. The difference between the resulting voltage (Fig. 7.11) and the ideal class-BJ voltage, or the error voltage $E_V$, can be calculated as:

140

$$Error_{f0} = \left(V_{f0\_measured} - V_{f0\_target}\right)^2 \tag{7.4}$$

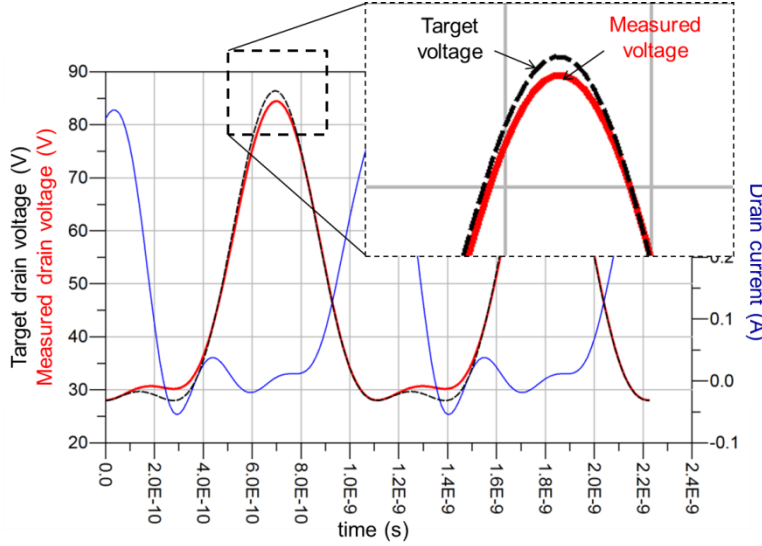$$Error_{2f0} = \left(V_{2f0\_measured} - V_{2f0\_target}\right)^2 \tag{7.5}$$



**Figure 7.11 – Difference between measured (red) and target (black) voltages.**

The next iteration of voltage-pull measurement, *i+1*, was calculated in a similar way, but an option of adding a weighting factor was also introduced (7.7) to enable a gradual convergence for cases where there was an overshoot in getting to a solution.

$$Z_{i+1} = \frac{V_{target}}{I_i} \tag{7.6}$$

$$Z_{i+1} = W\left(\frac{V_{target}}{I_i}\right) + (1-W)Z_i \tag{7.7}$$

where $I_i$ is the measured current from the previous iteration, and *W* is the weighting factor ranging from 0 to 1. Fig. 7.12 shows an example of obtaining the ideal class-BJ voltage waveform for α=0.2.

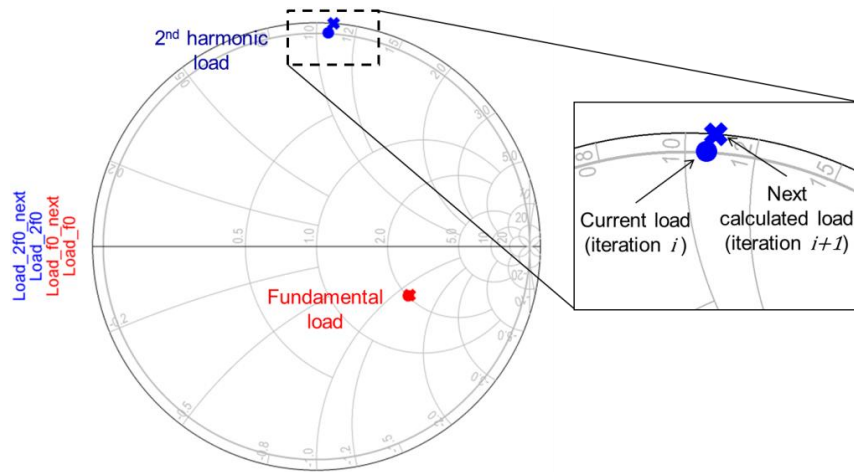**Figure 7.12 - Iteration example for α=0.2.**

The weighting factor was only needed in some of the iterations as they converged closer to the final solution. Throughout the voltage-pull iteration process, the drive level was adjusted such that the DC current component remained constant. This was to ensure that a proper baselining was done. The peak current value $I_{MAX}$ in this case could not be used as a reference in setting the drive level because it changes due to the displacement current from the nonlinear $C_{DS}$.

## 7.5      Voltage-Pull Measurement Results & Discussions

The voltage-pull measurement was first performed at a low input drive level to stay within the linear region and also to reduce the device $C_{DS}$ variation. The purpose of this step was not to analyse the output power and efficiency performance but to verify the algorithm developed in Section 7.4 on a real device. The same step was also performed in simulation for comparison.

In the second part of the experiment the device was driven approximately 1dB into compression exercising the full range of the $C_{DS}$-$V_{DS}$ nonlinear relationship to enable device performance analysis.

### 7.5.1      Verifying the Voltage-Pull Method Using Low Input Drive Level

Fig. 7.13 shows the simulated and measured voltage and current waveforms obtained from the voltage-pull method as well as the load trajectories when performed at a low drive level without hitting the knee region for $-1 \leq \alpha \leq 1$ in 0.2 steps. For this small voltage swing the variation in $C_{DS}$ was relatively small and the peak drain current did not vary significantly with $\alpha$.

There are several observations that can be made from this step. Firstly the voltage waveforms obtained from measurement were close to the ideal continuous class-BJ mode waveform which verified that the voltage-pull approach using an active load-pull system worked well in setting up an ideal continuous class-BJ mode. Secondly there was a good correlation between simulated and measured waveforms, providing a high confidence on the device model and simulation results.

However it was also observed that to obtain these ideal class-BJ voltage waveforms in measurement the 2$^{nd}$ harmonic load trajectory stays outside the Smith chart for $-1 \leq \alpha \leq 0$, unlike in simulation where the 2$^{nd}$ harmonic load enters inside the Smith chart, upholding the varactor effect even at this low drive level. The measurement results indicate possibly a resistive loss at the output after the device current generator plane for the real device which cancelled out the effect of the varactor observed in simulation and from the mathematical analysis in Chapter 6. This was the main discrepancy observed

between the device model and the actual device behaviour and shall be discussed further towards the end of this chapter.
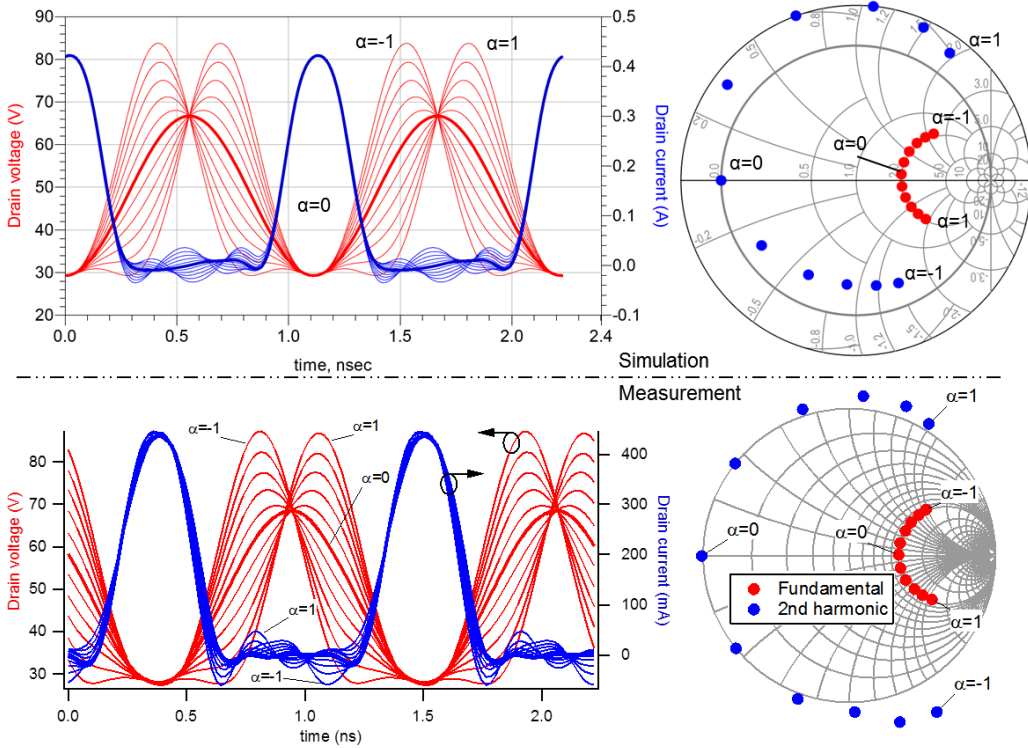


**Figure 7.13 - Voltage pull waveforms and load trajectory comparison between simulation (top) and measurement (bottom).**

### 7.5.2    Voltage-Pull Method at 1dB Compression & Optimum Load

In this step, the voltage-pull approach was applied while exercising the full voltage swing to have a larger $C_{DS}$ variation and boost the varactor effect. The pulling voltage at the device output was set such that the device current generator was presented with an efficiency-optimum load of 150Ω at α=0.

It was observed that with the bias, load, and drive level combination, the device entered an unstable condition at α≤-0.6 and α=1 where the voltage-pull approach was not able to converge properly to build the desired class-BJ voltage waveform at the output.   This stability issue limited the available α

range for this experiment.  An additional measurement point was added at α=-0.5 to improve the confidence in the test results.
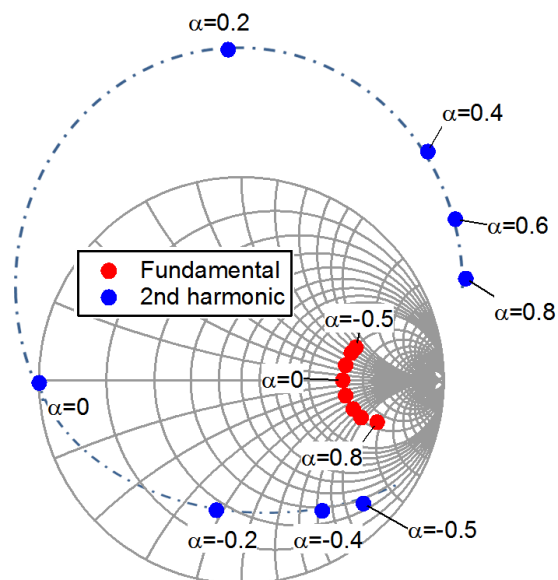


**Figure 7.14 - Measured class-BJ fundamental and 2nd harmonic loads from voltage-pull for -0.5≤α≤0.8.**

Fig. 7.14 shows the measured fundamental and 2nd harmonic load trajectories for -0.5≤α≤0.8.  For this working range of α, the 2nd harmonic load trajectory followed the theoretical behaviour and simulation trend where the varactor caused the 2nd harmonic load to go inside the Smith chart for the negative α values and outside the Smith chart for positive α values.

At each α the drive level was adjusted to keep the output DC current the same as at α=0.  Class-BJ voltage waveforms that were close to ideal could still be produced for -0.5≤α≤0.8 as shown in Fig. 7.15.  With the device driven into compression bifurcations were present in the output current waveforms and the current peak varied with α as a result of displacement current from the varactor.  It was therefore necessary to adjust the input drive

level to keep the DC current the same as the α=0 reference setting instead of using the maximum current ($I_{MAX}$) as a baseline as carried out in [1].
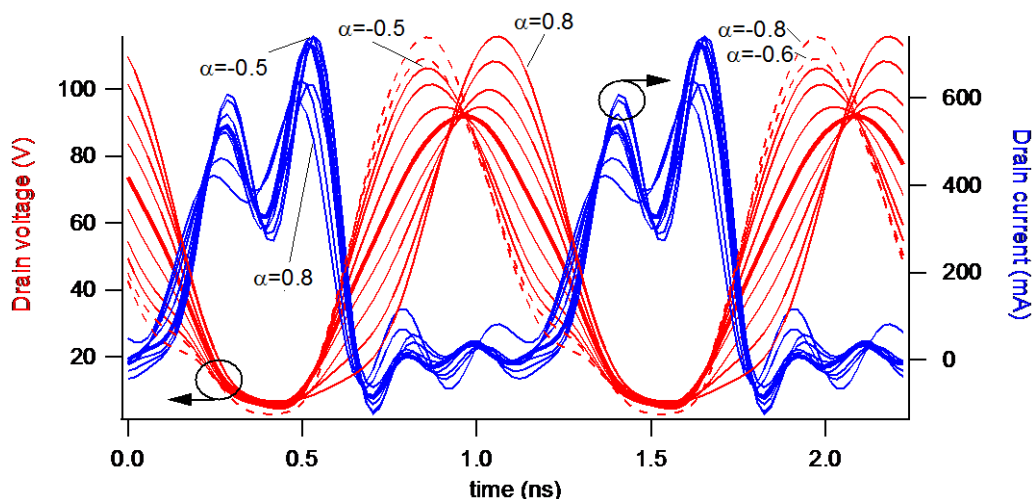


**Figure 7.15 – Measured voltage and current waveforms using voltage-pull for -0.5≤α≤0.8. Expected α=-0.6 and -0.8 voltages are shown with dotted lines.**

Fig. 7.16 shows the measured drain efficiency and output power as a function of α. Unlike simulation results (Fig. 7.5) and the mathematical analysis (Fig. 6.11) where the efficiency varied by at least 6%-point, the measured efficiency performance was relatively flat within this working α region, possibly due to the different criteria of selecting the drive level. Also, the simulation results and mathematical analysis predicted that the efficiency should go up in the positive α region, however from measurement a small decrease of approximately 3%-point was observed for the same region. So even though the experimental voltage-pull approach was successful in producing the almost-ideal class-BJ measured output voltage waveforms, it was not able to produce the predicted efficiency performance. It is suspected that the varactor effect had been counteracted by a lossy element, dissipating the energy that would theoretically be present as a $2^{nd}$ harmonic injection described in Chapter 6.

The next step of the investigation was to apply a phase shift to the output voltage and bring the 2nd harmonic loads that were inside the Smith chart in Fig. 7.14 (in the negative α region) towards the edge and recover the efficiency.
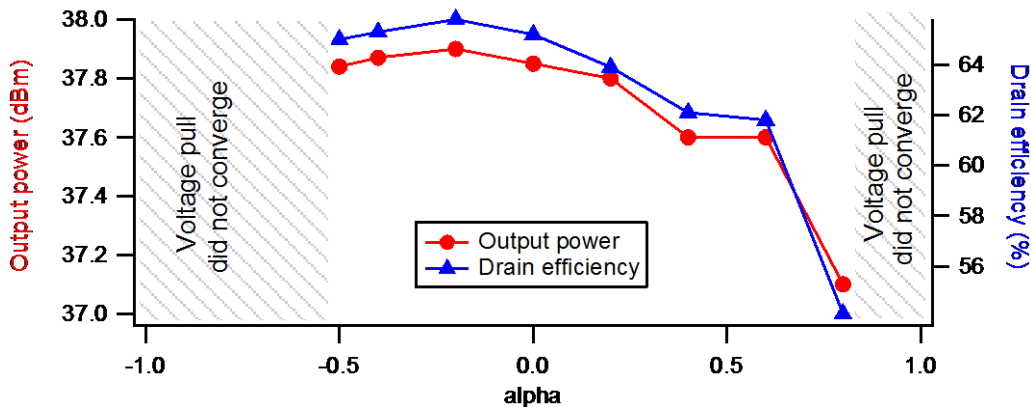


**Figure 7.16 – Measured output power and drain efficiency from voltage-pull.**

### 7.5.3    Applying Phase Shift on the Output Voltage

The objective of this section is to find out if it is possible to practically exploit the varactor and use it to improve efficiency performance in the negative α region.   As demonstrated in simulation and in the mathematical analysis, an improvement in efficiency can be obtained by pushing the 2nd harmonic loads that are inside the Smith chart towards the edge.   From the results obtained in Fig. 7.14 this was only applicable for α values of -0.2, -0.4, and -0.5.

Applying phase shift for each α required a slightly modified algorithm from the flow described in Fig. 7.10.   ADS software was used to estimate the initial required phase shift which was then set as the target voltage waveform. The voltage-pull method was then executed to construct this waveform on the device output.   If the resulting 2nd harmonic load did not sit on the edge of the

147

Smith chart, the phase of the voltage waveform was changed accordingly and the next iteration was executed. This process was repeated until the $2^{nd}$ harmonic sits on the edge of the Smith chart. Fig. 7.17 summarizes this process.
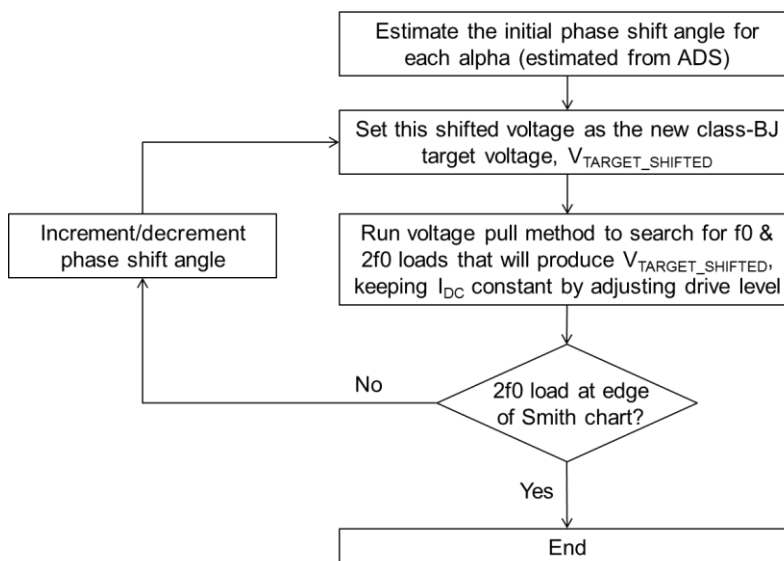


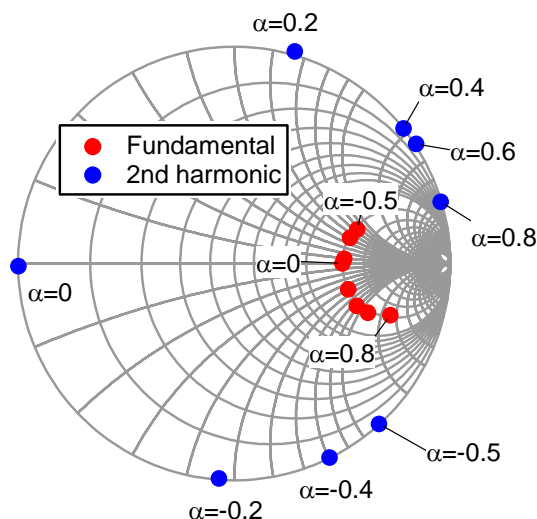**Figure 7.17 – Method to apply phase shift in measurement.**



**Figure 7.18 – Measured fundamental and $2^{nd}$ harmonic loads from voltage-pull with phase shift applied.**

The resulting measured fundamental and 2nd harmonic load trajectories with phase shift applied are shown in Fig. 7.18, for the applicable range of -0.5≤α≤0.8 in 0.2 steps.  In this example, the phase shift was not applied at α=0.

Fig. 7.19 shows the measured output power and drain efficiency comparison before and after applying phase shift.  A small improvement of 3%-point and 2%-point was observed at α=-0.4 and -0.5, respectively.   This amount was small compared to prediction from simulation and mathematical analysis which again was likely to be caused by the lossy element of the varactor.  As expected, the drain efficiency dropped in the positive α region with the removal of the 2nd harmonic injection effect provided by the varactor.

The small improvement seen at the negative α region can be traced to the distribution of fundamental and 2nd harmonic power before the phase shift, as shown in Fig. 7.20.   Before applying phase shift the split between fundamental and 2nd harmonic power was only ± 2% at best, compared to simulation (± 15%) and mathematical analysis (± 8%).
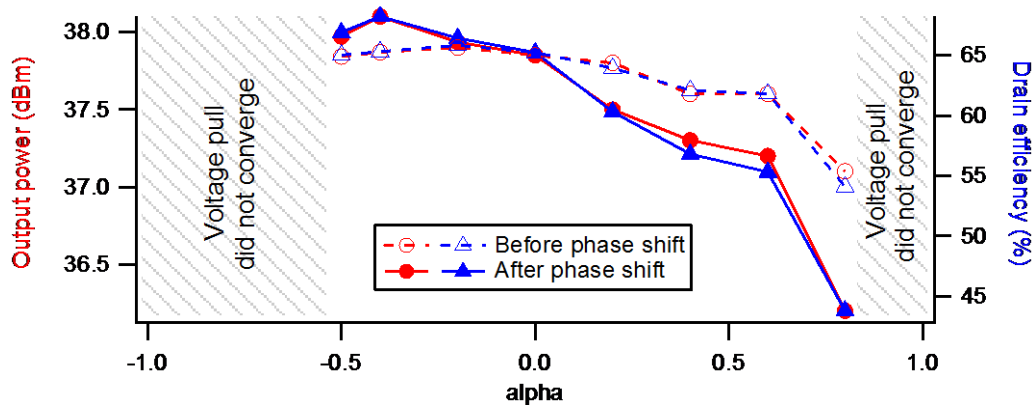


**Figure 7.19 – Measured output power and drain efficiency before and after phase shifting.**
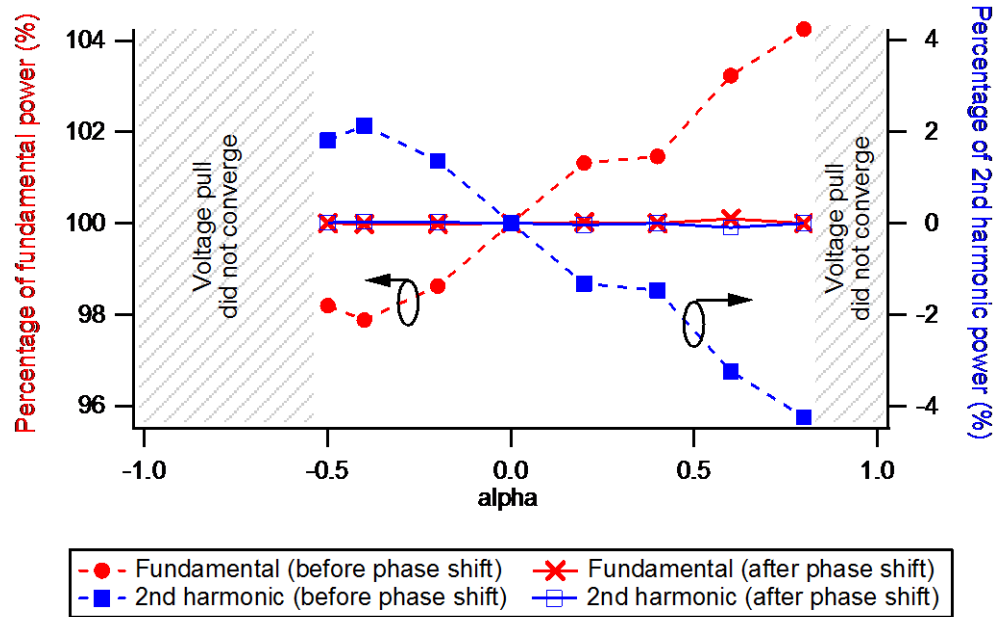
**Figure 7.20 – Measured fundamental and 2nd harmonic power distribution.**

## 7.6        Analysing the Lossy Varactor

The measurement results from voltage-pull indicate a discrepancy between actual varactor behaviour versus simulation and mathematical prediction.  It is suspected that the reason for this discrepancy is the resistive loss associated with the varactor.  This section aims to mathematically analyse this phenomenon by incorporating a series resistance to the varactor analysis from Chapter 6 and explain the experimental results.  It also aims to estimate the resistive element alongside the varactor for the device used in this work.

### 7.6.1        Modelling the Lossy Varactor

Since the manufacturer device model used in ADS simulations was not changeable, only mathematical analysis was performed.  The simplified circuit diagram from the Section 6.5 has been modified to include a resistor $R_S$ in series with the varactor as shown in Fig. 7.21, to model a lossy varactor.  An

iterative approach was used to calculate the current and voltage across the varactor at a given value of $R_S$, and is described in more detail in Appendix E.
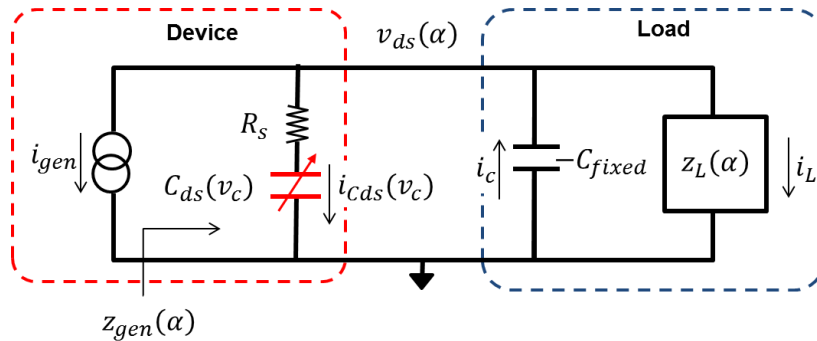


**Figure 7.21 - Modified circuit diagram to represent a lossy varactor.**

## 7.6.2      The Lossy Varactor Effect: Calculated Results
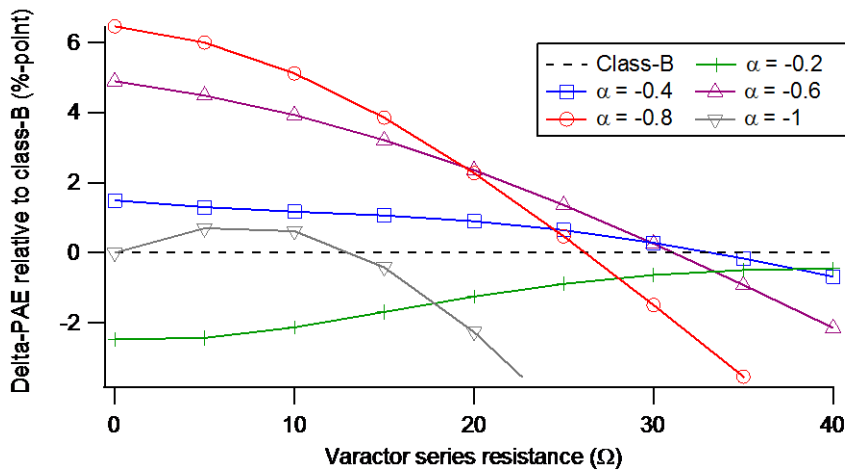


**Figure 7.22 - Calculated effect of varactor series resistance on drain efficiency**

With the addition of a series resistance, the efficiency improvement introduced by the varactor slowly declined as the resistance increased, as shown in Fig. 7.22.  In this calculation the same varactor characteristic from Fig 6.8 was used and the knee voltage effect was not included so that any decline in efficiency relative to class-B's 78.5% theoretical efficiency was contributed by the varactor series resistance alone.  For α=-0.8 where the calculated efficiency was highest for the lossless varactor case (Fig. 6.15), its efficiency

benefit was fully counteracted by a series resistance of approximately 27Ω. Overall, the calculated efficiency benefit for all α was completely diminished by a series resistance higher than 34Ω when the knee voltage effect was not included.

### 7.6.3      Estimating the Varactor Series Resistance of the Actual Device

In order to estimate the series resistance of the device used in Section 7.5, the varactor and device parameters were modified to reflect its actual behaviour instead of using ideal parameters. From Fig. 7.15 the knee voltage can be estimated to be 6V while the DC bias and voltage swing are 48V and 42V, respectively. The measured DC current of 195mA was used to determine the drain current magnitude.

With the knee voltage factor applied, the calculated class-B drain efficiency dropped to from 78.5% to 69% without any varactor series resistance ($R_S$=0Ω). The measured efficiency of 65% corresponds to a calculated efficiency performance with a varactor series resistance of 9Ω. This was the step used to estimate the varactor series resistance for the rest of α, which is summarized in Fig. 7.23.

From Fig. 7.23 there were some differences in the estimated series resistance before and after phase shift was applied. This could be attributed to the measurement uncertainty from the active load-pull setup and the accuracy of the fixed de-embedding value used. Even the $C_{DS}$ model itself was subject to uncertainty as a result of simplification techniques [2].

It was observed from this basic analysis that the varactor series resistance $R_S$ was not constant throughout the different α values in this class-

BJ mode of operation.  At α=0 (class-B) $R_S$ was 9Ω but at α=0.8 $R_S$ was approximately 29Ω.  This could be due to other factors not considered in this basic and simplified analysis, such as feedback and other experimental errors.  Without considering outliers, the estimated series resistance was approximately 8 to 12Ω.   Since this was a simplified analysis further investigations are needed to understand the reason for the series resistance variation with α in a continuous mode PA and it is proposed that this be carried out in future work.
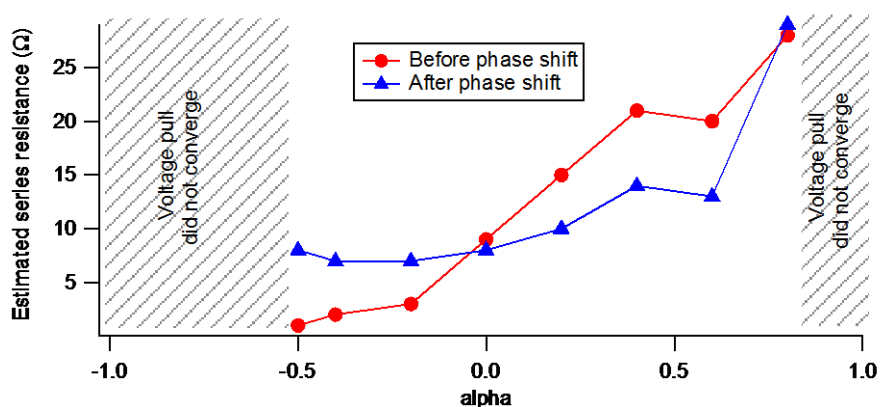


**Figure 7.23 - Estimated varactor series resistance based on measured data.**

## 7.7      Conclusions

The experimental investigation of the varactor effect on class-BJ mode PA has been presented in this chapter.  The novel voltage-pull approach provides an alternative method to characterise continuous mode power amplifiers and exposes the varactor effect.  Voltage pull simulations performed using the device model validated the varactor effect theory discussed in Chapter 6.

An experimental investigation of the voltage-pull approach is presented utilising the active load-pull system.  In this work several challenges were

encountered in its implementation. The first challenge was providing high enough fundamental and 2$^{nd}$ harmonic injected power at the device output in order to formulate the desired output voltage. Secondly a device stability issue was also encountered, most likely due to the fact that the device used for this work was a 'test device' packaged specifically for this PhD work. This test device did not have the proper output-input feedback isolation internally as do the standard ones.

The theory of exploiting the varactor for drain efficiency enhancement, although showing potential in the mathematical analysis and simulation, was limited in the measured results, possibly due to the resistive loss of the varactor. A maximum of 3% improvement was obtained from voltage-pull measurement at α=-0.4. This number could possibly be further improved using different $C_{DS}$-$V_{DS}$ characteristics than the one used in this work, and this extended investigation can be included in future work.

Finally it is also proposed that this this research be extended onto other device technologies such as Gallium Nitride (GaN) which is currently gaining traction in the mobile communication systems [3].

## 7.8     References

[1]     V. Carrubba, "Novel highly efficient broadband continuous power amplifier modes," PhD Thesis, Cardiff University, 2012.

[2]     P. Aaen, Jaime A. Plá, and J. Wood., *Modeling and Characterization of RF and Microwave Power FETs*: Cambridge University Press, 2007.

[3]     S. C. Cripps, *RF Power Amplifiers for Wireless Communications*: Artech House, 2006.

# Chapter 8

# Conclusions & Future Work

## 8.1    Conclusions

Maximizing the system-level efficiency performance of an envelope tracking (ET) power amplifier system requires both the envelope amplifier and the RF power amplifier to be highly efficient.  However, in previous ET system designs, less attention has been given to the RF power amplifier [1] and the class-AB mode RF PA has been the common choice for implementation [2].  This research work fills that gap and provides a systematic analysis on the use of higher-efficiency RF PA modes, and specifically in this work, class-F in ET system applications.  This chapter discusses and concludes the five objectives listed in Chapter 1 for this research.

The novel use of waveform engineering in analysing any PA mode for envelope tracking applications has been described, revealing the challenge of maintaining a particular high-efficiency mode such as class-F throughout the entire ET supply range, due to the nonlinear $C_{DS}$ variation.  This analysis uncovers the maximum available efficiency of class-F and class-AB modes in ET as well as the predicted efficiency when the PA load impedances are optimised at any given bias point.  The effect of $C_{DS}$ on the optimum load at different bias and the resulting load trajectory have been demonstrated for class-F and class-AB using a 50V high voltage LDMOS device.  For class-F, it was shown that optimising the loads at 28V improved the efficiency at 7.5dB

OBO by approximately 8%-point compared to when the class-F loads were optimised at maximum bias of 48V.

A systematic design method for a class-F PA for ET applications has been developed based on the findings from the waveform engineering experiment at variable bias settings. The method provides the ability to optimise based on the efficiency-linearity-gain trade-off analysis from different design requirements and constraints. From CW characterisation, it was observed that for class-F, there was minimal trade-off in efficiency when the envelope shaping function targeted a flat gain (linear) performance in ET if the PA was in compression. This method can also be used to design PA's operating in other modes and other technologies such as GaN, to be implemented in ET systems.
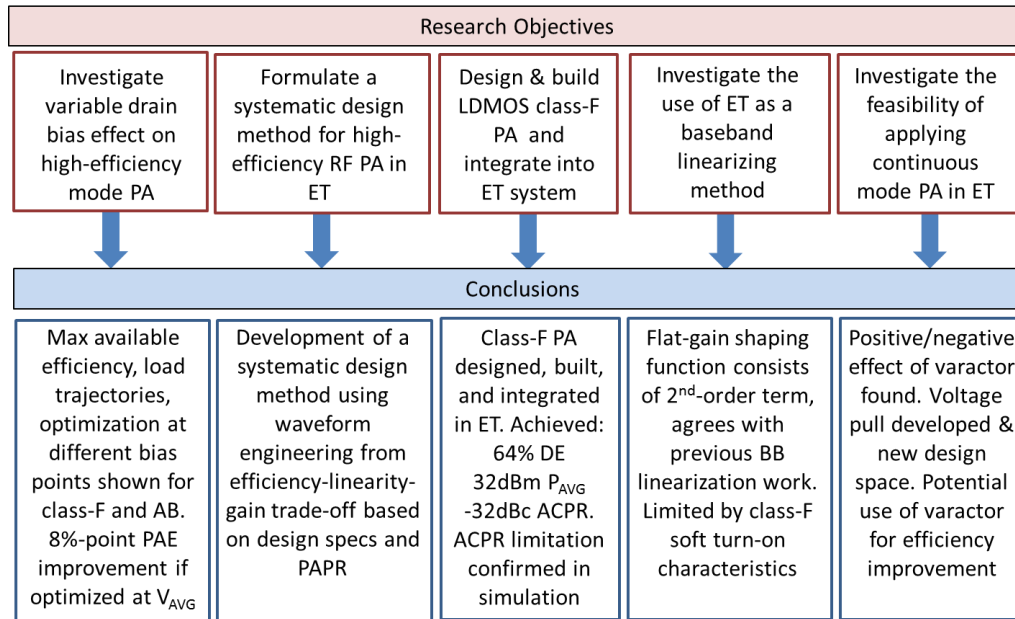
The formulated method was used to design and fabricate a prototype 900MHz class-F PA using a packaged 10W 50V LDMOS device as a proof of concept. From CW measurements, the measured peak drain efficiency of 73% occurred at 3dB OBO while at 7.5dB OBO, the measured DE was 68%. This PA was then integrated into an industry-standard ET system at *Arelis* in France. The measured ET system level efficiency for both the PA and the ET modulator combined was 64% producing 32dBm average output power using a 5MHz LTE signal with a 7.5dB PAPR. The measured efficiency is among the highest compared to the state-of-the-art ET PA's at the time of writing, as shown in Fig. 5.14. However, the measured ACPR was -32dBc due to the soft turn-on nature at very low input level and was not able to be corrected by DPD, and it is suggested for future work that a variable gate bias is used to address this issue, as described in the next section.

The use of ET as a baseband linearisation method has also been explored in addition to improving efficiency. The ET *flat-gain* shaping function for a linear performance consisted of a $2^{nd}$-order term which agreed with the findings from [3]. Therefore it can be concluded that the baseband signal injection at the drain has the potential to be implemented as an envelope shaping function in ET systems, but its effectiveness in reducing AM-AM distortion is limited when used with a class-F mode PA due to the soft turn-on characteristics which resulted from a class-B biasing. A different outcome can be expected if a class-$F^{-1}$ is used, for example with GaN technology.

The use of a continuous class-F PA mode in a variable drain bias has been demonstrated using waveform engineering, and it highlighted the positive and negative effects of the nonlinear output capacitance, or the varactor, on the PA efficiency performance even at a single bias. These findings led to the development of a novel method to characterise continuous mode PA's called voltage-pull, enabling a new design space to be explored. From mathematical analysis and simulation results, it was observed that there is a possibility to exploit the varactor as a $2^{nd}$ harmonic injection source to improve efficiency. However, the measured results did not achieve the level of improvement predicted and it is suspected that it was due to the varactor having an associated resistive loss. Although the experimental efficiency improvement from this approach was minimal compared to simulation, the outcome of this study can be used for future work in this topic, and may well be more relevant to other device technologies.

While the envelope tracking architecture is getting more attention as the demand for bandwidth and efficiency increases, it is currently more widely

used in user equipment (UE) rather than in base stations due to challenge of balancing efficiency, linearity, bandwidth, and power handling of the ET modulator [4]. The implementation of ET in base stations is therefore proposed initially on small cells, with the advancements in medium-power ET modulators such as the one used in the Opera Net 2 project.

| Research Objectives | | | | |
|---|---|---|---|---|
| Investigate variable drain bias effect on high-efficiency mode PA | Formulate a systematic design method for high-efficiency RF PA in ET | Design & build LDMOS class-F PA and integrate into ET system | Investigate the use of ET as a baseband linearizing method | Investigate the feasibility of applying continuous mode PA in ET |
| Conclusions | | | | |
| Max available efficiency, load trajectories, optimization at different bias points shown for class-F and AB. 8%-point PAE improvement if optimized at $V_{AVG}$ | Development of a systematic design method using waveform engineering from efficiency-linearity-gain trade-off based on design specs and PAPR | Class-F PA designed, built, and integrated in ET. Achieved: 64% DE 32dBm $P_{AVG}$ -32dBc ACPR. ACPR limitation confirmed in simulation | Flat-gain shaping function consists of 2nd-order term, agrees with previous BB linearization work. Limited by class-F soft turn-on characteristics | Positive/negative effect of varactor found. Voltage pull developed & new design space. Potential use of varactor for efficiency improvement |

**Figure 8.1 - Research objectives and conclusions.**

## 8.2     Future Work

This research has demonstrated the potential and limitations of using a high-efficiency mode PA in ET architectures. There are areas for further research that can be taken as future work that stems from this study.

### 8.2.1     Variable Gate Bias for Linearity Improvement

While the ET shaping function has been shown to have the potential to be used as a baseband linearisation signal, a class-F mode PA in an ET system would also require a gate bias modulation as a function of the input envelope. This is needed to rapidly adapt the bias from pinch-off to a class-

AB-like bias at very low drive levels, trading-off a small enough efficiency to meet the linearity requirement.  Fig. 8.2 shows some simulated results that illustrate the potential of linearising the device transconductance while maintaining high efficiency by varying both gate and drain bias voltages of a class-F mode PA under a 2-tone excitation.  Further work is required in defining this 'gate bias shaping function' and aligning it with the drain modulation.
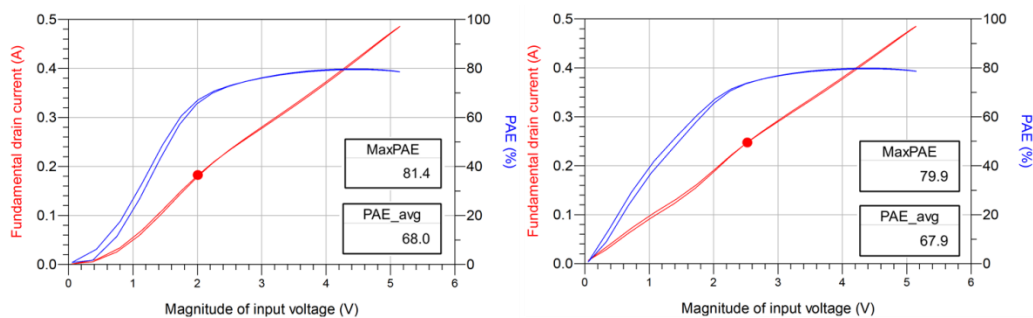


**Fig 8.2 - The effect of varying only the drain bias (left) and varying both drain and gate bias (right) on the linearity of the transconductance curve.**

### 8.2.2      Further Shaping Function Adjustment and Optimisation in an ET Test Environment

In Chapter 5, the ET system level test was performed using shaping functions that would ideally replicate the *'flat-gain'* and *'max-PAE'* shaping functions defined in Chapter 4.  However, the shaping function entry at the ET system level was done in the digital domain using digital-to-analogue converters (DAC), causing a level of uncertainty in the exact replication of the desired shaping functions.

Furthermore, the desired shaping functions were extracted from CW measurements using a fixture that was de-embedded to the current generator plane.  At the PA level and in an ET integrated system, the input and output

characteristics have changed and this potentially will affect the shaping function accuracy. Ideally a different setup is needed which would have the ability to automatically search for a constant gain criteria and generate a new shaping function in situ. Such a system would have a controllable DC supply which would take the place of an ET drain modulator. Having this capability allows for a more accurate shaping function generation and deployment.

### 8.2.3    Using GaN Technology in Inverse Class-F Mode for Potential Incremental Efficiency and Linearity Improvement

GaN technology has a smaller on-resistance ($R_{ON}$) compared to LDMOS and a smaller output capacitance. These characteristics potentially could produce a higher baseline drain efficiency compared to LDMOS as seen in [5]. Using a GaN device also would enable the inverse class-F mode which theoretically would avoid the linearity issue caused by the soft turn-on phenomenon seen in class-F mode PA's. The class-$F^{-1}$ mode was not possible to be implemented in this research due to the large $C_{DS}$ associated with LDMOS technology, making it difficult to present an open circuit at the 2nd harmonic through active load-pull.

### 8.2.4    Automating the Voltage-Pull Method for Continuous Mode PA Characterisation

The voltage-pull method described in Chapter 7 was performed manually, toggling between the active load-pull system and the load calculation template in ADS in several iterations. The iteration process could be made faster through automation by merging the two functions (load calculation and load-pulling) into one user interface.

There was also an issue with regards to stability of the device which prevented a full characterisation of the continuous mode in Chapter 7. A comprehensive stability analysis is therefore needed to address this issue for a fully functional voltage-pull test setup.

### 8.2.5    Further Research into the Varactor for Effect on Continuous Mode PA's and Potential Use for Efficiency Enhancement

The mathematical analysis shown in Chapter 6 indicated a possibility of exploiting the varactor for efficiency enhancement, but this was limited in the actual device. This research predicted that the lossy element of the varactor contributed to this discrepancy. However it is also noted that the mathematical analysis performed in Chapters 6 and 7 is a simplified analysis and there could be other factors involved, which were not included such as the input capacitance effect. The measurement results could also inherently have a larger uncertainty than expected as a result of de-embedding inaccuracies. Further research is needed to understand the discrepancies between the predicted and the actual device performance, as well as investigating optimum $C_{DS}$-$V_{DS}$ characteristics that would enlarge the varactor effect for a potentially larger efficiency improvement.

## 8.3    References

[1]    G. F. Collins, J. Fisher, F. Radulescu, J. Barner, S. Sheppard, R. Worley, et al., "Power Amplifier Design Optimized for Envelope Tracking," in Compound Semiconductor Integrated Circuit Symposium (CSICs), 2014 IEEE, 2014, pp. 1-4.

[2]    K. Bumman, M. Junghwan, and K. Ildu, "Efficiently Amplified," Microwave Magazine, IEEE, vol. 11, pp. 87-100, 2010.

[3]    F. L. Ogboi, P. J. Tasker, M. Akmal, J. Lees, J. Benedikt, S. Bensmida, et al., "A LSNA configured to perform baseband engineering for device

linearity investigations under modulated excitations," in Microwave Conference (EuMC), 2013 European, 2013, pp. 684-687.

[4]     Z. Wang, Envelope Tracking Power Amplifiers for Wireless Communications: Artech House, 2014.

[5]     P. Wright, A. Sheikh, C. Roff, P. J. Tasker, and J. Benedikt, "Highly efficient operation modes in GaN power transistors delivering upwards of 81% efficiency and 12W output power," in Microwave Symposium Digest, 2008 IEEE MTT-S International, 2008, pp. 1147-1150.

# Appendix A

# Measurement Setup

## A.1    Active Load-Pull System and Waveform Engineering Measurement Setup

The waveform engineering approach uses an active load-pull system to construct the desired current and voltage waveforms at the transistor current generator plane. It is achieved by synthesizing the required fundamental and harmonic loads at any bias point hence setting up any PA mode of operation, emulating a harmonic balance simulation in actual measurement.

The voltage and current waveform measurements are performed using a measurement system based around an Agilent N5242A PNA-X Nonlinear Vector Network Analyser (NVNA) as the receiver. It can measure up to 26.5GHz but for this work the fundamental frequency is set at 900MHz. Three signal generators together with their associated power amplifiers are used to synthesize the travelling fundamental and harmonic waves incident on the output of the device, setting up the fundamental and harmonic load conditions up to the third harmonic as shown in Fig. A.1. A triplexer is used to combine the 3 harmonics into 1 path, placed between the device and the load-pull signal generators. The input signal is a 900MHz continuous wave (CW) signal generated by an RF signal generator with a driver amplifier. No input matching is applied on the device input side in this research work, instead the input drive level is increased accordingly to overcome the mismatch losses to arrive at the desired input power level.

External directional couplers are used to sample the incident and reflected waves on both sides of the device to the PNA-X receiver channels. The PNA-X ports 1 and 2 are used for the device under test (DUT) while ports 3 and 4 are used to connect the phase reference modules which enable the nonlinear measurements by correlating the relative phase of the harmonics.

The DC bias signals for the gate and the drain of the device are supplied by an HP 6629A DC Power Supply with 4 outputs of 50W each and a maximum voltage of 50V, which meets the requirements for this work.
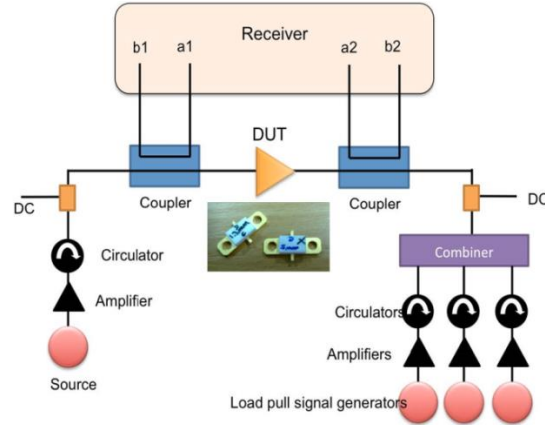


**Figure A.1 - Active load-pull system that enables waveform engineering**

Fig. A.2 shows the fully configured bench setup. The active load-pull system is run using the Mesuro software which enables 3-harmonic load search, multi-parameter sweeps, and 3 layers of de-embedding.
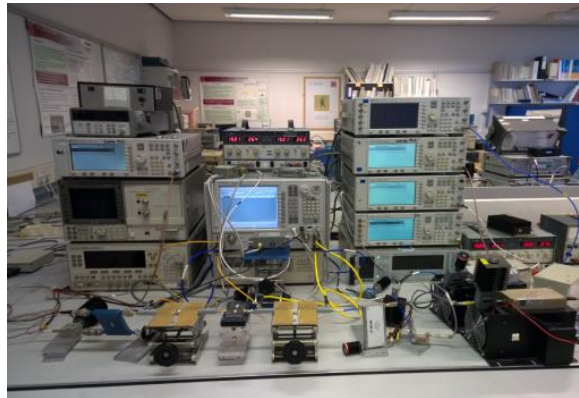


**Figure A.2 - Waveform measurement system**

## A.2      Device Under Test, Fixture, and De-embedding

The transistor device used in this work is a 10W high voltage LDMOS from Freescale (now NXP) with a gate width of 5.2mm in packaged form. As it is a test device made for this research work, it has a single bond wire each at the gate and the drain. The knee voltage is around 10V while its maximum operating drain voltage of 50V provides a higher output impedance compared to a 30V device of the same power capacity.

### A.2.1. Test Fixture De-embedding

For load-pull measurements, the device is tested on a test fixture fabricated for this work. A Thru-Reflect-Line (TRL) calibration kit is also fabricated to enable the extraction of the fixture transmission line s-parameters for de-embedding purposes, as shown in Fig. A.3. The TRL calibration kit has 2 lines of different lengths that are used for 2 frequency ranges of calibration: 700MHz to 6GHz and 2GHz to 15GHz.
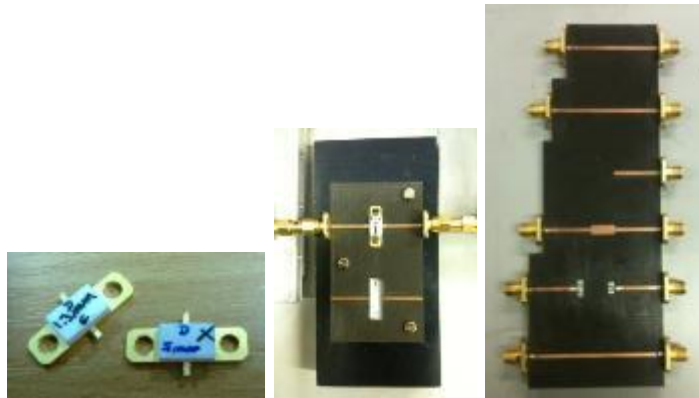


**Figure A.3 – Packaged 50V LDMOS devices (left), test fixture (centre), and TRL calibration kit (right).**

### A.2.2. Device Package De-embedding

The device model to be used in Keysight ADS simulation software is provided by Freescale. The model consists of the die which inherently includes the drain-to-source capacitance ($C_{DS}$), gate and drain manifolds, and the pad capacitance. The dimension of the bond wires are characterised during the fabrication of these devices and therefore their models are then generated in ADS using the *BONDW1* element. The nonlinear relationship between $C_{DS}$ and the drain voltage $V_{DS}$ of the device is also provided which therefore enables a complete de-embedding process from the device package to the device current generator plane.

For load-pull measurements that involve drain bias variation, a two-layer de-embedding is used to obtain the waveform information at the device current generator plane (Fig. A.4). The first layer is a fixed de-embedding that includes the test fixture, pad capacitance, bond wires, and gate/drain manifolds. The second layer is a bias-dependent de-embedding to cater for the

drain-to-source output capacitance ($C_{DS}$) which changes nonlinearly with the drain voltage. For this work the feedback capacitance between the gate and the drain ($C_{GD}$) is not considered as the value is too small and can be neglected.
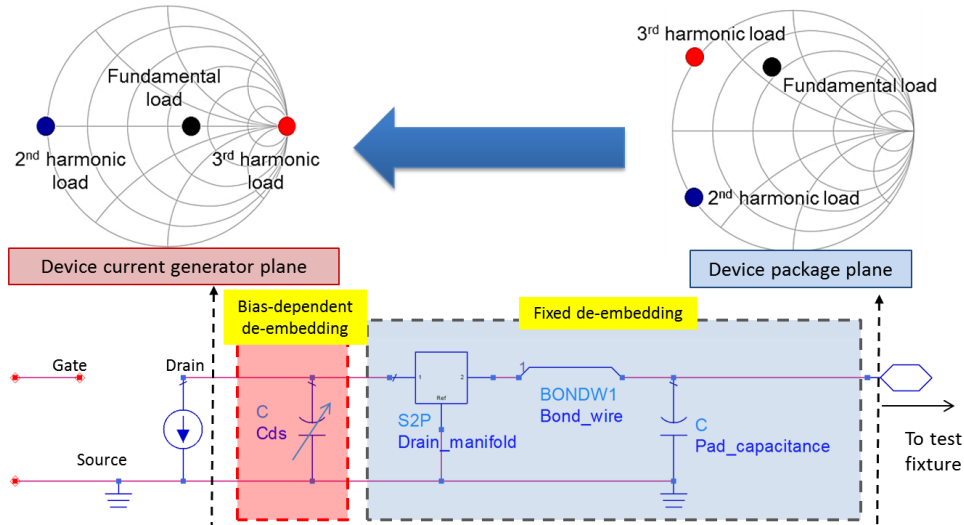


**Figure A.4 – Device de-embedding stages shown here for the output side**

## A.3 **Correlating Device Model Simulation with Actual Measurement**

Verifying that the actual device performance is correlated to the device model is a critical step in this research. Having a good correlation enables most of the research and experimentation work to be performed in simulation first with confidence and using the measurement system as a validation step, saving measurement time. Rigorous steps have been taken to verify that the model simulation correlates with the actual measurements, including through DC current-voltage (DC-IV) characterisation, s-parameter comparison, and harmonic load manipulation. This Appendix presents examples of these verification steps.

### A.3.1. DC-IV Characterisation

The first comparison made between the device and the model is the DC-IV characteristics. Fig. A.5 shows the comparison for drain current versus drain voltage and versus gate voltage. It was observed that the device model predicts a maximum drain current of 1A whereas the actual device only

produced 0.8A maximum. This potentially means that the device model will produce higher gain and output power compared to the actual device under the same condition, and subsequently higher efficiency. However the trend of the pinch-off condition is similar between simulation and measurement, both showed that the device starts to turn on at around 2V gate bias.
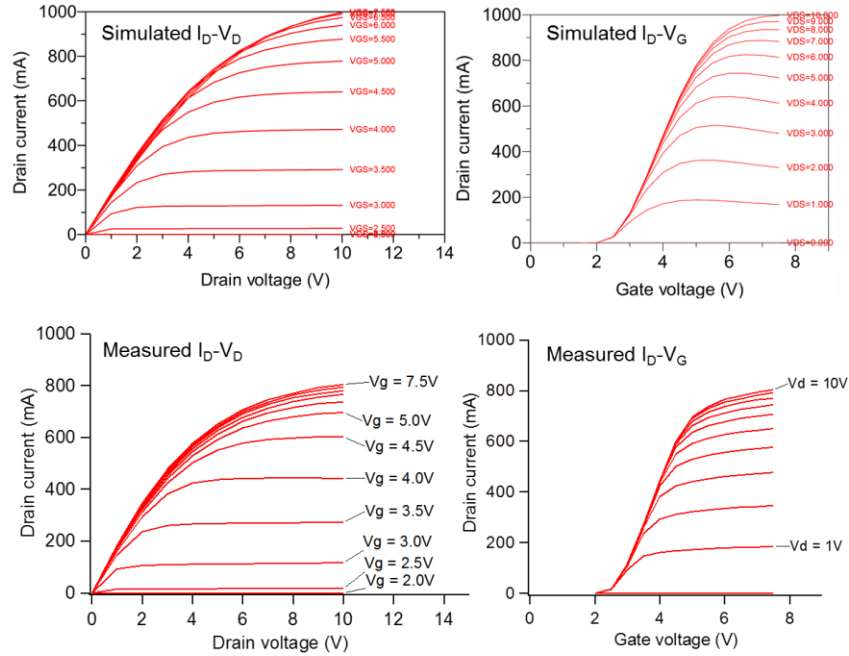


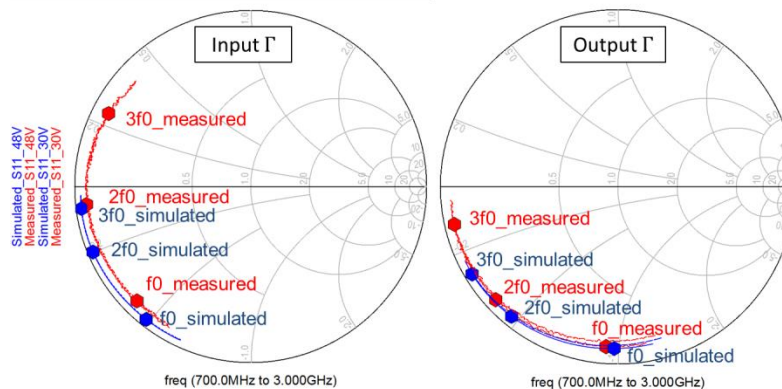**Figure A.5 - DC-IV comparison between simulation (top) and measurement (bottom).**

## A.3.2. S-Parameter Comparison

Bias-dependent s-parameter measurements are made in simulation and measurements, where the drain bias is varied within the device operating range and the gate is biased at a class-AB point. The measured s-parameters are made at the device package plane by de-embedding the test fixture. Fig. A.6 below shows the S21 comparison between simulation and measurements when the gate is biased at 2.5V and the drain at 30V and 48V.
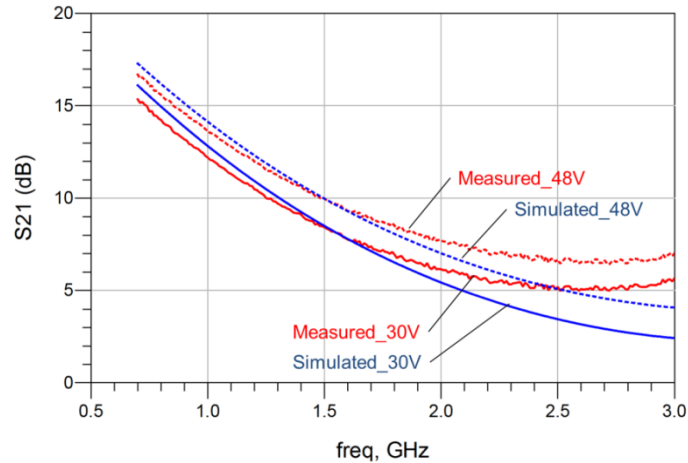
**Figure A.6 - S21 (top) and S11 (bottom) comparisons between simulation (blue) and measurement (red) at 30V and 48V.**

The measured S21 has a similar trend as the simulation at both drain voltages, with the device model having a relatively higher S21 below 1.5GHz. The differences between simulation and measurement at 900MHz are 0.5dB and 0.7dB for 48V and 30V drain biases, respectively.



**Figure A.7 - S11 and S22 comparison between simulation and measurement.**

Both simulation and measurements show a high input reflection based on the S11 results and that there's an overlap between 30V and 48V bias (Fig. A.7). Table A.1 below compares the simulated and measured input and output reflection coefficients for 30V which is similar to 48V. The difference between simulation and measurement gets bigger at higher frequencies. This potentially will result in different available source power requirements between simulation and measurement to get to the same input power at the gate.

| Frequency | Simulated $\Gamma_{IN}$ | Measured $\Gamma_{IN}$ | Simulated $\Gamma_{OUT}$ | Measured $\Gamma_{OUT}$ |
|---|---|---|---|---|
| 900MHz | 0.96 ∠-128 | 0.92 ∠-135 | 0.91 ∠-91 | 0.91 ∠-94 |
| 1.8GHz | 0.97 ∠-157 | 0.94 ∠-174 | 0.95 ∠-129 | 0.94 ∠-137 |
| 2.7GHz | 0.97 ∠-173 | 0.91 ∠153 | 0.96 ∠-149 | 0.95 ∠ -167 |

**Table A.1 – Input reflection comparison between simulation and measurement.**

### A.3.3.  Harmonic Load Manipulation Comparison

Ultimately the correlation of interest between simulation and measurement is in the performance at the current generator plane under a certain harmonic load combination, an exercise that takes into account the effect of de-embedding accuracy. This section presents the steps taken in determining the right $C_{DS}$ de-embedding for load-pull, followed by the simulation and measurement comparison of a class-F mode PA.

The first step is to find the right de-embedding for the actual device. Using load-pull measurements, a search for maximum efficiency point is performed and different $C_{DS}$ values are iteratively used until the maximum output power and efficiency of the load-pull contours are located on the real axis of the Smith chart. Fig. A.8 shows the iteration performed for the 48V drain bias setting, where the optimum $C_{DS}$ value for de-embedding was found to be 1.3pF. This step is repeated at other drain bias settings as well.



Cds = 1.0pF                Cds = 1.2pF                Cds = 1.3pF
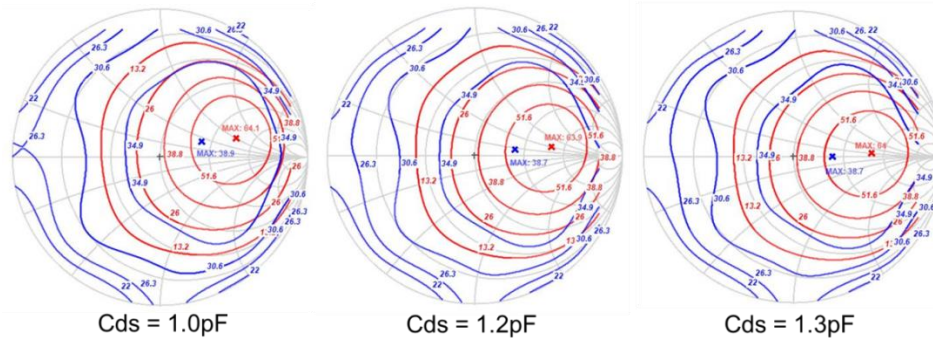
**Figure A.8 - Iterations to find the right de-embedding in measurements.**

The next step is to compare simulated load-pull against measured load-pull, with the same harmonic load combination on the current generator plane. The comparison shown in this section is achieved by performing a power sweep at 28V drain bias with the PA set to operate in a class-F mode. The fundamental load presented to the current generator plane in this example is

117Ω which is targeting a maximum efficiency performance, while the 2$^{nd}$ and 3$^{rd}$ harmonics are presented with a short and an open circuit, respectively. Fig. A.9 compares the gain and PAE between the model and actual device as a function of output back-off from peak power. The model has approximately 0.8dB higher gain before the compression region, as predicted from the DC-IV differences. This produces a PAE of close to 80% at its peak, while the measured device exhibits a maximum PAE of 74%. The maximum output power from simulation in this case is 36.4dBm, 0.6dB higher than the measured output. Although the absolute performance result values are different, the actual device does exhibit the same trend as the model.
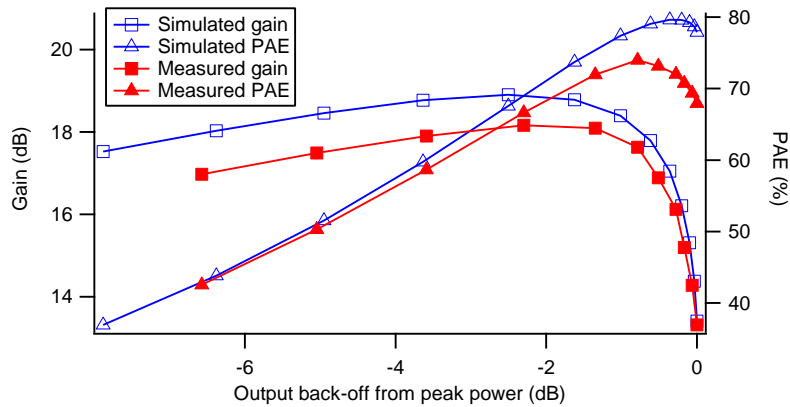


**Figure A.9 – Gain and PAE comparison between simulation and measurement.**

Fig. A.10 shows the DC, fundamental, and 2$^{nd}$ harmonic current at the drain as a function of the input voltage magnitude, normalized to the location of maximum gain. Both simulation and measurement show a similar trend, although the model generates higher fundamental drain current output.

Finally the simulated and measured time-domain waveforms with power sweep of up to 5dB compression are compared, as shown in Fig. A.11. The squared voltage waveform characteristic of class-F can be seen on both cases, with the simulation having a slightly bigger swing. The measured current peaks at 650mA compared to 600mA from simulation. This small difference could be attributed to the difference in the fundamental impedance presented to the current generator plane or residual de-embedding error between simulation and load-pull. However in general the device model does show a good

correlation with the actual device especially in predicting performance trends with different fundamental and harmonic load combinations.
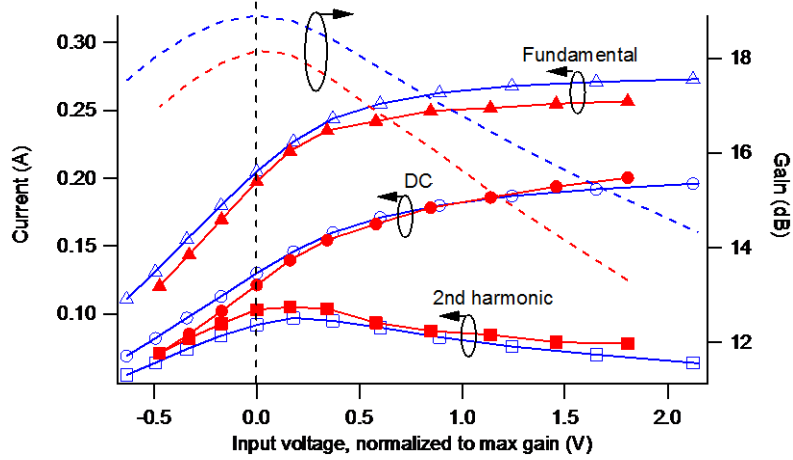


**Figure A.10 - DC, fundamental, and 2<sup>nd</sup> harmonic current comparison between simulation (blue) and measurement (red) normalized to maximum gain location.**
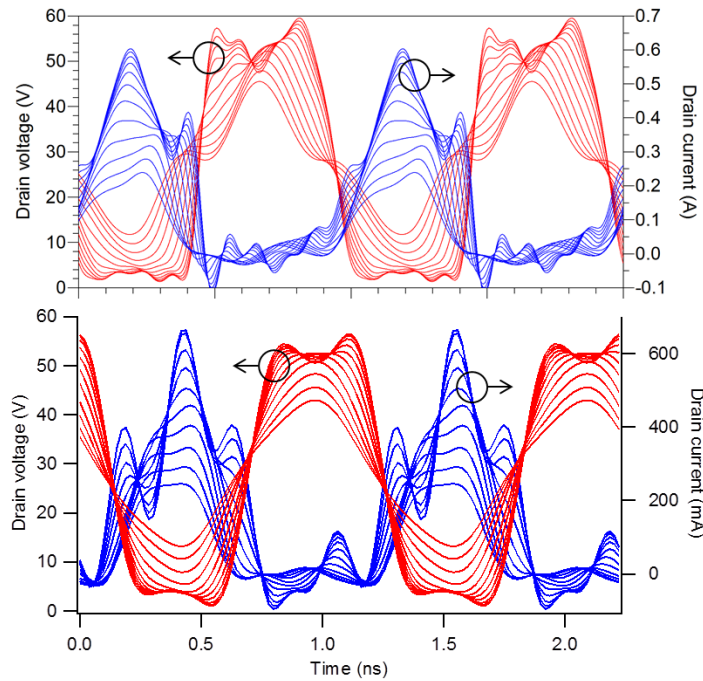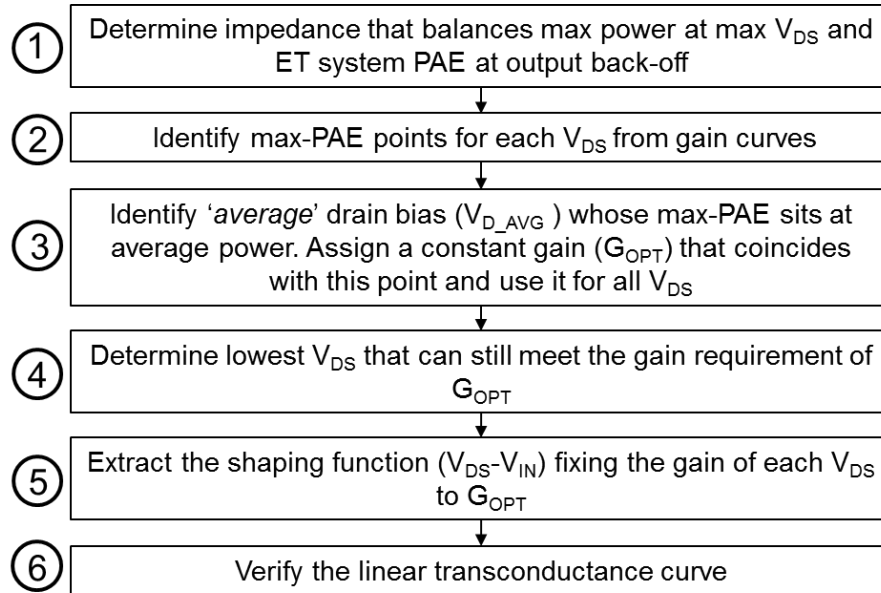


**Figure A.11 - Voltage (red) and current (blue) waveforms during power sweep from simulation (top) and measurement (bottom).**

171

# Appendix B

# Simulation Data for the Design Method Formulation

## B.1. Formulating the Design Flow of a Class-F PA for an ET Application

A design flow has been formulated in designing a class-F PA to be used in an ET architecture that considers the factors that will influence efficiency and linearity with the constraint on output power and signal PAPR. Fig. B.1 shows the proposed design flow, achieved through waveform engineering.



**① Determine impedance that balances max power at max $V_{DS}$ and ET system PAE at output back-off**

**② Identify max-PAE points for each $V_{DS}$ from gain curves**

**③ Identify '*average*' drain bias ($V_{D\_AVG}$) whose max-PAE sits at average power. Assign a constant gain ($G_{OPT}$) that coincides with this point and use it for all $V_{DS}$**

**④ Determine lowest $V_{DS}$ that can still meet the gain requirement of $G_{OPT}$**

**⑤ Extract the shaping function ($V_{DS}$-$V_{IN}$) fixing the gain of each $V_{DS}$ to $G_{OPT}$**

**⑥ Verify the linear transconductance curve**

**Figure B.1 - Formulated design flow**

This section describes with simulation results the design flow of a class-F to be used in an ET system with a peak output power specification of 40dBm

and signal PAPR of 7.5dB. The useable drain bias range for ET is from 16V to 48V.

## B.2.      Finding the Optimum Fundamental Load

The ET efficiency is defined as the trajectory of maximum PAE curves of different drain bias within the ET drain supply range of 16V to 48V. Fig. B.2 shows the simulation outcome of this exercise in ADS. For this PA design, the chosen output reflection coefficient is 0.34 which corresponds to an optimum load of 101.5Ω as it provides a good compromise between peak power and average efficiency.
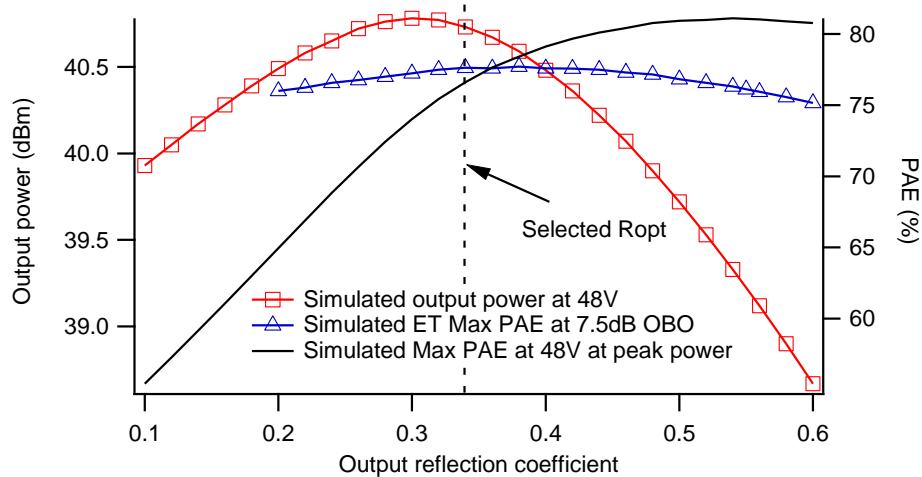


**Figure B.2 – Simulated output power at 48V bias and the corresponding ET system PAE at 7.5dB OBO**

## B.3.      Identifying Maximum-PAE locations, Assigning Constant Gain (G$_{OPT}$), and Minimum Drain Bias (V$_{D\_MIN}$) from Gain Curves

A family of gain curves obtained from power sweep at different drain bias with the device operating in a class-F mode is shown in Fig. B.3. The bias that has its maximum PAE sitting on the average power in this case is 20V and the intersecting gain is chosen as the target constant gain value for each V$_{DS}$, which is 14.5dB. The lowest drain bias that can still meet that gain value is 16V which is set as the minimum ET drain supply range. The simulated PAE also shown in Fig. B.3 indicates less than 2%-point worst-case trade-off in efficiency when the ET shaping function targets a constant 14.5dB gain performance,

while the output power range where this constant gain holds is approximately 10.5dB.
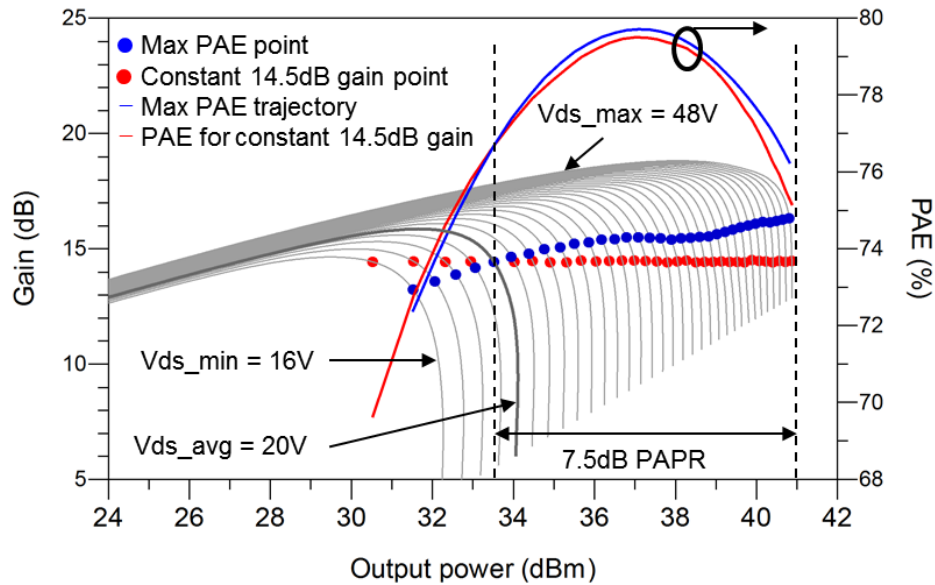


**Figure B.3 - Simulated gain curves with locations of maximum PAE (blue dots) and flat 14.5dB gain (red dots), and the corresponding PAE.**
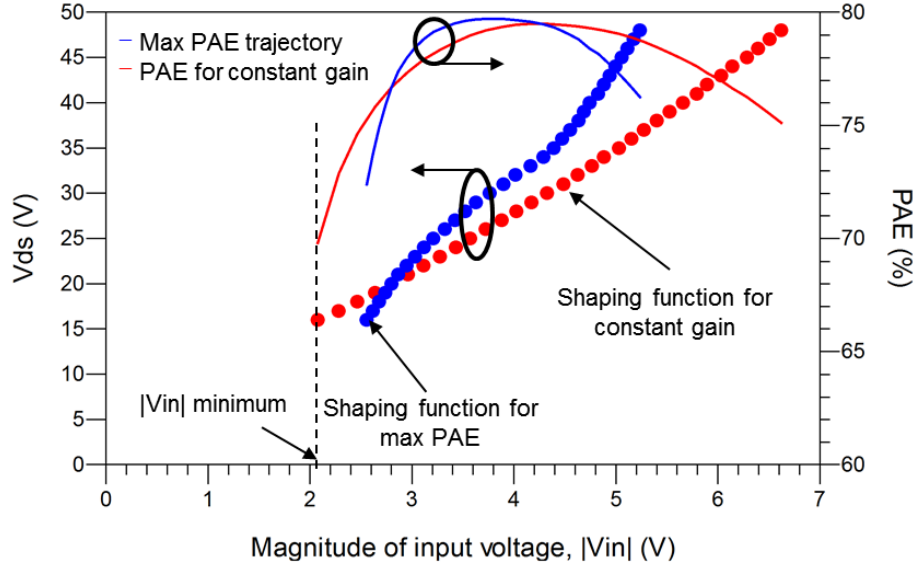
## B.4.    Extracting the Shaping Function

Fig. B.4 shows the extracted ET shaping function from the previous simulation step, which describes the relationship between the input voltage and the drain supply voltage. The first shaping function (blue) targets maximum efficiency throughout the ET operating range while the second one (red) targets a flat gain performance and therefore linearity. From simulation the quadratic feature of the *flat-gain* shaping function is not really apparent but as shown in Chapter 4 it does consist of even order coefficients. The lowest input voltage that will enable this flat gain performance is shown in the plot as $|V_{IN}|$ minimum.
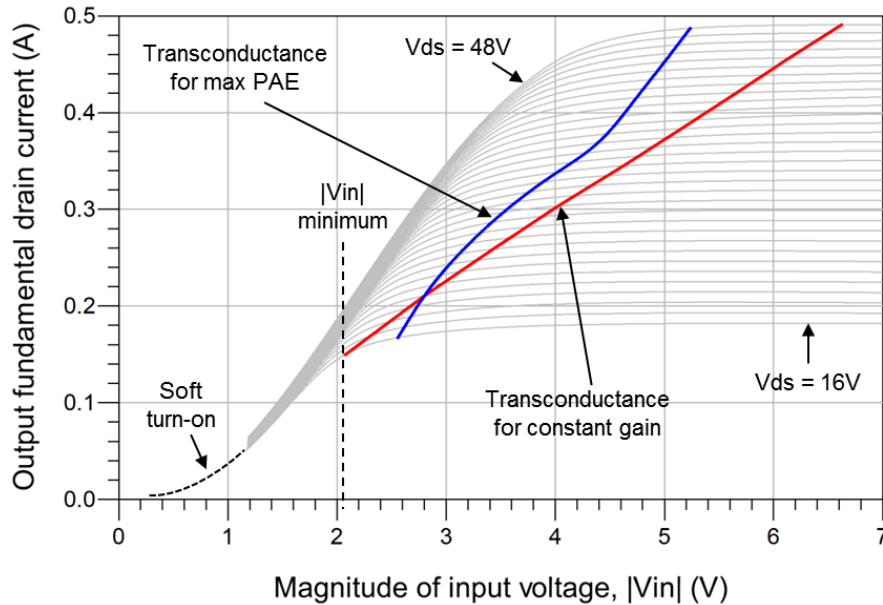
## B.5.    Verifying the Transconductance Curve

Fig. B.5 shows the resulting transconductance plot for both shaping functions. As expected the shaping function that holds a flat gain yields a linear relationship between the input voltage and the output fundamental current of the device. However this linear relationship has a limited range, where it only

applies when the input voltage is above the minimum $|V_{IN}|$. For lower input voltage, it will follow the transconductance curve of the lowest $V_{DS}$ bias within the ET range.



**Figure B.4 - Extracted shaping function for maximum PAE (blue) and constant 14.5dB gain (red) from simulation.**



**Figure B.5 - Verifying the simulated linear performance from the transconductance plot.**

# Appendix C

# Continuous Mode Power Amplifier Theory

## C.1.    Introduction

The basis of the continuous mode power amplifier starts with the formulation of the class-J power amplifier that was introduced by Cripps in [1]. The class-J applies a phase shift on the fundamental and 2nd harmonic loads of a class-B mode PA at -45° and 90°, respectively and retains the class-B output power and efficiency performance. The work in [2] further presented a design space continuum between the class-B and class-J states which would maintain the same output power and efficiency performance, enabling a high bandwidth design of matching network. This continuous mode of operation is referred to as the continuous class-BJ mode.

## C.2.    Formulation of the Continuous Class-BJ Mode

The continuous class-BJ mode of operation has a half-rectified current waveform as class-B but applies a raised sine function of the continuous mode operator $(1 - \alpha \sin \vartheta)$ to the normalized class-B output voltage:

$$I_{Cont_{BJ}}(\vartheta) = I_{max} \cos \vartheta \qquad 0 < \vartheta < \frac{\pi}{2} \text{ and } \frac{3\pi}{2} < \vartheta < 2\pi$$

$$= 0 \qquad \frac{\pi}{2} < \vartheta < \frac{3\pi}{2} \tag{C.1}$$

$$V_{Cont\_BJ} = V_{max}(1 - \cos \vartheta) \cdot (1 - \alpha \sin \vartheta) \tag{C.2}$$

where the range of α is defined from -1 to 1 in order to keep the voltage above zero. Multiplying out the terms in (C.2) yields:

$$V_{Cont\_BJ} = V_{max}(1 - \cos\vartheta - \alpha\sin\vartheta + \frac{\alpha}{2}\sin 2\vartheta) \qquad\text{(C.3)}$$

Fig. C.1 shows the ideal normalized output voltage and current waveforms of a class-BJ mode power amplifier as the variable α is varied from -1 to 1 in 0.2 steps. At α=0 (shown in black) the voltage waveform returns to a class-B output state. It is noted that the voltage swing of the class-BJ mode increases by almost a factor of 1.5 from the class-B state at α=-1 and α=1.
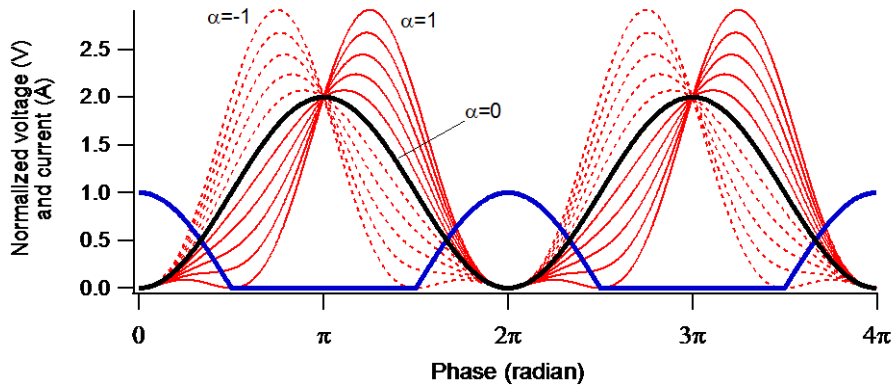


**Figure C.1 – Output voltage (red, black) and current (blue) waveforms of class-BJ power amplifier when α is varied from -1 to 1 in 0.2 steps.**

The normalized DC, fundamental and 2$^{nd}$ harmonic frequency voltage components can be extracted from C.3:

$$V_{DC} = 1 \qquad\text{(C.4)}$$

$$V_{f0}(\alpha) = -1 + j\alpha \qquad\text{(C.5)}$$

$$V_{2f0}(\alpha) = 0 - j\frac{\alpha}{2} \qquad\text{(C.6)}$$

From the voltage and current equations the fundamental and second harmonic loads can be derived as a function of α:

$$Z_{f0} = R_{opt} - j \cdot \alpha \cdot R_{opt} \qquad\text{(C.7)}$$

$$Z_{2f0} = -j \cdot \alpha \cdot \frac{3\pi}{8} \cdot R_{opt} \qquad\text{(C.8)}$$

where R$_{OPT}$ is the normalized optimum load. Again, at α=0 the pair of load impedances return to the class-B load state. It is noted from (C.8) that the

2nd harmonic load is always located on the edge of the Smith chart. Fig. C.2 shows the trajectories of the fundamental and 2nd harmonic loads on the Smith chart as α is varied from -1 to 1 with $R_{OPT}$=101.5Ω from Chapter 5.
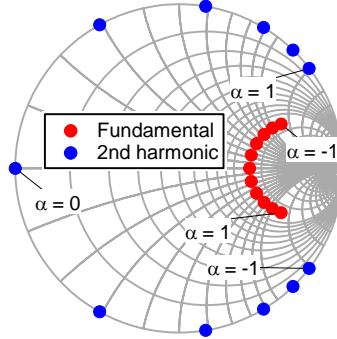


**Figure C.2 – Trajectories of fundamental (blue) and 2nd harmonic loads (red) of a class-BJ power amplifier with $R_{OPT}$=101.5Ω for -1<α<1 in 0.2 steps.**

The resulting normalized output power and theoretical efficiency is maintained at 1 and 78.5%, respectively throughout α values from -1 to 1 as shown in Fig. C.3.

## C.3.    Formulation of the Continuous Class-F Mode

The continuous mode operator of $(1 - \alpha \sin \vartheta)$ can also be applied to the output voltage of class-F to produce the continuous class-F mode. Class-F mode has the same half-rectified current waveform as class-B while the output voltage is ideally a squared waveform if infinite harmonics are used. For this analysis only the first 3 harmonics are considered as described in [3] and applying the raised sine function of the continuous mode operator produces the voltage equations below:

$$V_{Cont\_F} = V_{max} \left( 1 - \frac{2}{\sqrt{3}} \cos \vartheta + \frac{1}{3\sqrt{3}} \cos 3\vartheta \right) \cdot (1 - \alpha \sin \vartheta) \tag{C.9}$$

which can be expanded into the equation below, showing up to the 3rd harmonic component:

$$V_{Cont\_F} = V_{max}(1 - \frac{2}{\sqrt{3}} \cos \vartheta - \alpha \sin \vartheta + \frac{7}{6\sqrt{3}} \alpha \sin 2\vartheta + \frac{1}{3\sqrt{3}} \cos 3\vartheta) \tag{C.10}$$

The normalized individual frequency components can therefore be extracted:

$$V_{DC} = 1 \tag{C.11}$$

$$V_{f0}(\alpha) = -\frac{2}{\sqrt{3}} + j \cdot \alpha \tag{C.12}$$

$$V_{2f0}(\alpha) = -j\frac{7}{6\sqrt{3}} \cdot \alpha \tag{C.13}$$

$$V_{3f0}(\alpha) = \frac{1}{3\sqrt{3}} \tag{C.14}$$

It is noted that only the fundamental and 2$^{nd}$ harmonic voltages have a dependency on α. Fig. C.3 shows the ideal normalized output voltage and current waveforms of a continuous class-F with α varied from -1 to 1 in 0.2 steps, as well as the theoretical efficiency performance and normalized output power. As with the previous section, at α=0 the output waveforms become the conventional class-F waveforms.



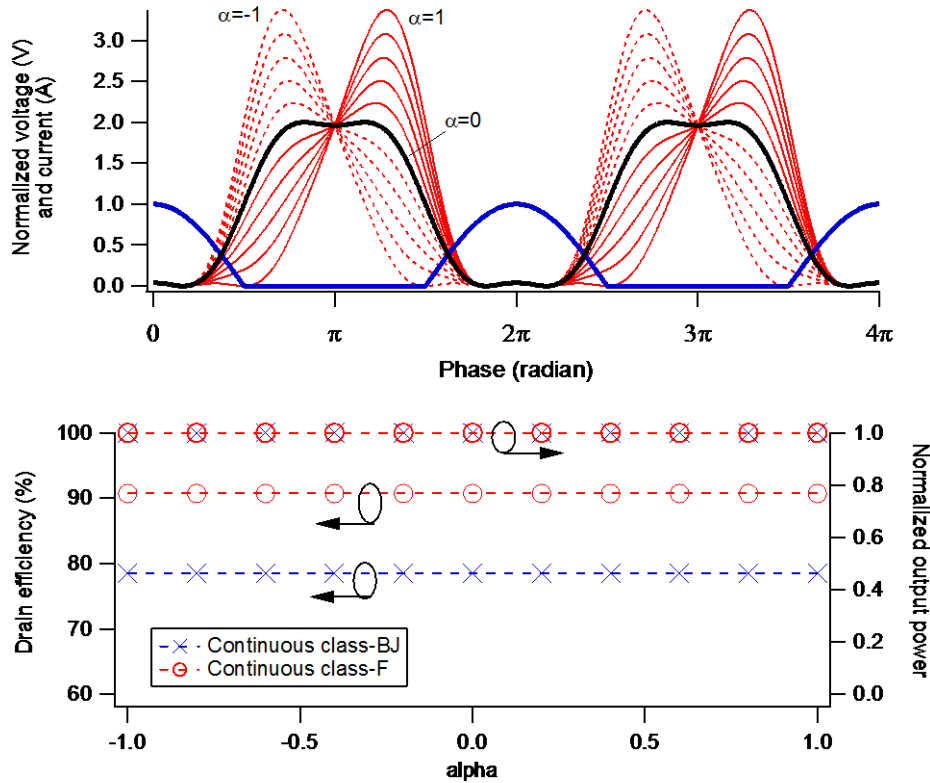**Figure C.3 – Top: Output voltage (red, black) and current (blue) waveforms of a continuous class-F power amplifier when α is varied from -1 to 1 in 0.2 steps. Bottom: Efficiency and normalized output power for continuous class-BJ and F.**

Dividing each component with the corresponding current component results in the following load impedances for the fundamental, 2nd, and 3rd harmonic components:

$$Z_{f0} = R_{opt} - j\frac{\sqrt{3}}{2}\alpha \cdot R_{opt} \tag{C.15}$$

$$Z_{2f0}(\alpha) = j \cdot 1.375 \cdot \alpha \tag{C.16}$$

$$Z_{3f0}(\alpha) = \infty \ (open\ circuit) \tag{C.17}$$

Fig. C.4 shows the trajectory of the continuous class-F mode with α varied from -1 to 1 using the same $R_{OPT}$ of 101.5Ω from the previous chapter. The 3rd harmonic load remains in an open circuit condition while the trajectories of fundamental and 2nd harmonic loads move in opposite directions.
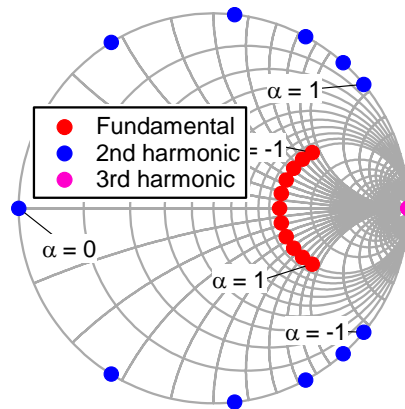


**Figure C.4 – Trajectories of fundamental, 2nd, and 3rd harmonic loads of a continuous class-F power amplifiers with $R_{OPT}$=101.5Ω for -1<α<1 in 0.2 steps.**

## C.4. References

[1]     S. C. Cripps, RF Power Amplifiers for Wireless Communications: Artech House, 2006.

[2]     S. C. Cripps, P. J. Tasker, A. L. Clarke, J. Lees, and J. Benedikt, "On the Continuity of High Efficiency Modes in Linear RF Power Amplifiers," Microwave and Wireless Components Letters, IEEE, vol. 19, pp. 665-667, 2009.

[3]     P. Colantonio, F. Giannini, G. Leuzzi, and E. Limiti, "On the class-F power amplifier design," International Journal of Rf and Microwave Computer-Aided Engineering, vol. 9, pp. 129-149, Mar 1999.

# Appendix D

# Voltage-Pull Simulation Method

## D.1.    Setting up the Voltage-Pull Simulation

The voltage-pull simulation is performed in ADS using the Harmonic Balance simulator. Fig D.1 shows the ADS schematic where a *V_nHarm* voltage source is connected to the load side of the device. The device model is a die model with intrinsic drain-source capacitance ($C_{DS}$). To probe the voltage and current waveforms at the current generator plane ($I_{GEN}$), a negative capacitor is used for de-embedding. This negative $C_{DS}$ value is fixed based on the value given by the manufacturer based on the drain bias voltage.

In this simulation the waveforms after the $C_{DS}$ which contains the sum of the displacement current and $I_{GEN}$ is obtained by placing back a positive $C_{DS}$. Another negative $C_{DS}$ is required to enable probing at the $I_{GEN}$ plane.

The continuous class-BJ voltage equations as a function of α as described in Appendix C are used to define the DC, fundamental, and $2^{nd}$ harmonic voltage magnitudes respectively, while higher harmonic voltages are set to zero. The phases of these components are initially set to zero but in the later part of the simulation their values will change to simulate the effect of phase-shifting.

The desired impedance at α=0 is achieved by adjusting the magnitude of the voltage source at fundamental frequency. The parameter α is swept from -1 to 1 in 0.2 steps, modifying the output voltage and the output power and PAE are recorded.

**Figure D.1 – Voltage pull simulation setup with a fixed C$_{DS}$ de-embedding (top), and the equations used in the analysis (bottom).**

To simulate a phase shift effect on the output voltage and bring the 2$^{nd}$ harmonic loads to the edge of the Smith chart, the phase of the *V_nHarm* source is changed manually using the ADS Tuning function.

# Appendix E

# Calculating the Lossy Varactor

## E.1. Calculating the Current and Voltage: an Iterative Approach

To model a lossy varactor, a series resistor is added in series with $C_{DS}$ as shown in Fig. E.1. The Igor program developed in Section 6.5 is modified to iteratively calculate the varactor voltage and current for a given series resistor value as shown in Fig. E.2. At the start of the iteration the 'lossless' varactor voltage is used to determine the corresponding $C_{DS}$ and varactor current. With a known series resistor value assigned, the calculated current is then used to calculate the next iteration of varactor voltage $V_{NEXT}$ using Kirchhoff's Voltage Law. This voltage is then compared with the previous iteration and an error voltage is calculated. The magnitude of the error voltage is used to determine if the next iteration is required. The process is repeated until the error is reduced to near zero or until the iteration reaches a certain limit. A weighting factor is applied in the voltage iteration to improve convergence success rate.
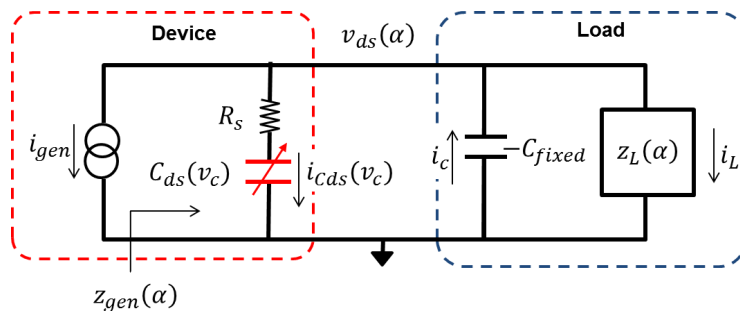


**Figure E.1 – Modified circuit diagram to represent a lossy varactor.**

## E.2. Estimating the Varactor Series Resistance of the Actual Device

In order to estimate the series resistance of the device used in Section 7.5, the varactor and device parameters are modified to reflect its actual

behaviour instead of using ideal parameters. These modified parameters are then used to calculate the corresponding drain efficiency where the series resistance value is swept in 2Ω steps. Fig. E.3 shows the comparison between the calculated drain efficiency at different series resistance values and the measured efficiency from voltage-pull. To have a higher confidence on the estimation, the comparison process is performed both before and after phase shifting is applied.
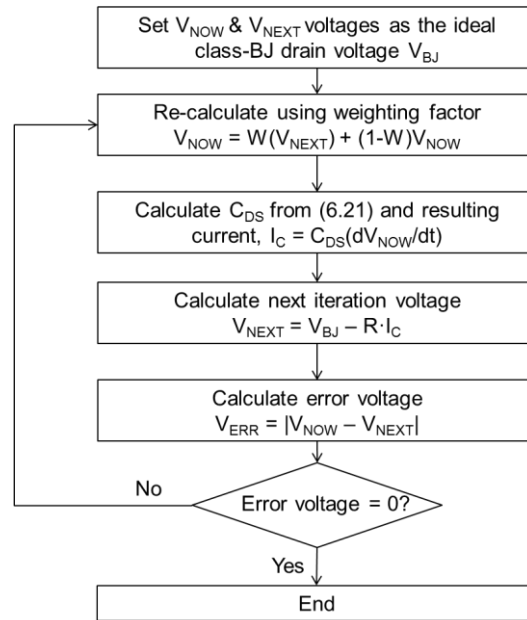


**Figure E.2 – Iterative approach to determine the lossy varactor effect.**

With the knee voltage factor applied the calculated class-B drain efficiency drops to from 78.5% to 69% without any varactor series resistance ($R_S$=0Ω). The measured efficiency of 65% corresponds to a calculated efficiency performance with a varactor series resistance of 9Ω. This is the step used to estimate the varactor series resistance for the rest of α, which is summarized in Fig. E.4. However only α values between -0.5 and 0.8 are available since the voltage-pull approach was not able to converge beyond this α range.
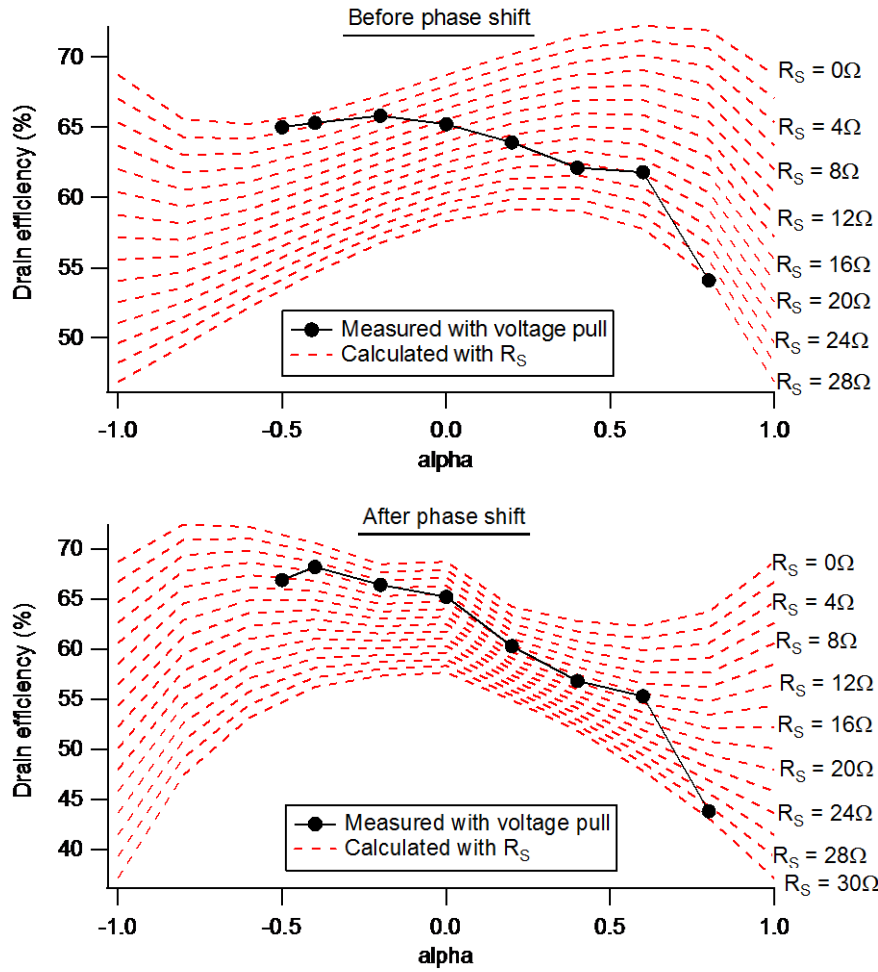
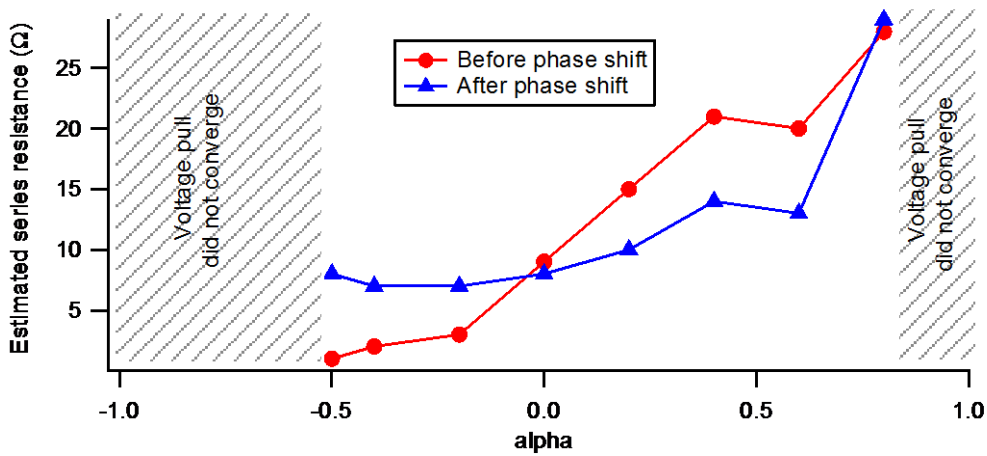**Figure E.3 – Comparing measured data with calculation (red) to estimate varactor series resistance.**



**Figure E.4 – Estimated varactor series resistance based on measured data.**